

**Development of a Pneumatic PDMS MEMS Actuator**  
**Using a Closed Loop Controller for Endoscopic Applications**

by

Ali Moallemi

B.A.Sc., The University of Tehran, 2016

A THESIS SUBMITTED IN PARTIAL FULFILLMENT OF

THE REQUIREMENTS FOR THE DEGREE OF

MASTER OF APPLIED SCIENCE

in

THE FACULTY OF GRADUATE AND POSTDOCTORAL STUDIES

(Mechanical Engineering)

THE UNIVERSITY OF BRITISH COLUMBIA

(Vancouver)

August 2019

© Ali Moallemi, 2019

The following individuals certify that they have read, and recommend to the Faculty of Graduate and Postdoctoral Studies for acceptance, a thesis/dissertation entitled:

Development of a Pneumatic PDMS MEMS Actuator Using a Closed Loop Controller for Endoscopic Applications

---

submitted by Ali Moallemi in partial fulfillment of the requirements for

the degree of Master of Applied Science

in Mechanical Engineering

**Examining Committee:**

Mu Chiao, Department of Mechanical Engineering

Supervisor

Ryozo Nagamune, Department of Mechanical Engineering

Supervisory Committee Member

Xiaoliang Jin, Department of Mechanical Engineering

Supervisory Committee Member

---

Additional Examiner

**Additional Supervisory Committee Members:**

---

Supervisory Committee Member

---

Supervisory Committee Member

## Abstract

Gastrointestinal (GI) cancer is one of the most significant public health issues globally. Early diagnosis results in increasing the probability of surviving GI cancers. However, it is difficult to develop diagnostic tools for early GI cancer detection. One of the challenges is to design an endoscope with adequate optical quality. This thesis demonstrated a pneumatic miniaturized PDMS (Polydimethylsiloxane) MEMS (Microelectromechanical Systems) actuator with high stability to improve optics. Theoretical, experimental, and simulation methods were used to characterize the actuator. An electronic platform with a PID (Proportional–Integral–Derivative) controller was designed to control the actuator. A feedback control mechanism was designed to eliminate disturbances, and provide a stable position for the actuator. A trial-and-error method, the Matlab<sup>®</sup> PID Tuner, and Genetic Algorithm were used to find and verify the PID parameters.

To demonstrate the functionality of the actuator, a confocal system was used to obtain images of paper fiber and onion epidermis. The actuator shows an axial resolution of  $1.12\ \mu\text{m}$  and the optical resolution of  $21.5\ \mu\text{m}$ . The actuator designed in this study has several advantages, such as ease of miniaturization and stability that make it attractive for further development.

## **Lay Summary**

Cancer is among the leading causes of death worldwide. Gastrointestinal (GI) cancers are one of the greatest public health issues globally. Diagnosing the GI cancer at the early stages leads to significantly improving the probability of surviving GI cancers. A non-invasive optical imaging technology could be used to assist early GI cancer detection. In clinical practice, an endoscope is typically a tubular instrument used to look deep into the body as a diagnostic tool. Endoscopes used in procedures is called an endoscopy. For cancer diagnosis examination, tissue samples should be analyzed. Oversampling is often required to minimize false negative results. However, it has significant adverse effects on patients given the invasiveness and time-consuming nature of the procedure. The focus of the presented thesis is developing a miniaturized soft actuator with appropriate imaging technology that could improve early GI cancer detection. The actuator designed in this study has several advantages that makes it attractive for further clinical applications. We are hoping to reduce the number of biopsies, but the exact number will need to be studied further.

## Preface

The research presented in this thesis was carried out in the University of British Columbia (UBC) MEMS Laboratory by the author, Ali Moallemi, in the Department of Mechanical Engineering under the supervision of Dr. Mu Chiao. A portion of the research was also conducted in the Imaging Unit of Integrative Oncology Department in the British Columbia Cancer Agency Research Center (BCCRC), under the supervision of Dr. Haishan Zeng.

The designed Z-scanner actuator in this research combined with the X-Y scanner provided 3D images. The X-Y scanner actuator was developed by Ran Fan, my colleague in UBC MEMS Laboratory, based on her thesis: “*A Piezoelectric Fiber Scanner for Reflectance Confocal Imaging of Biological Tissues.*”

This work was presented in the following conference:

- ❖ Ran Fan\*, **Ali Moallemi\***, Yunshan Zhang, Lei Chen, Yuan Zhao, Zhenguo Wu, Ryoza Nagamune, Keng Chou, Haishan Zeng, and Mu Chiao, “A hybrid Pneumatic and piezoelectric 3D micro scanner for cancer imaging,” *The 20<sup>th</sup> International Conference on Solid-State Sensors, Actuators and Microsystems*, Berlin, Germany, 2019.

A version of the presented thesis with the focus on the control system, and the MEMS pneumatic actuator has been submitted for a peer reviewed journal article:

- ❖ **Ali Moallemi**, Amir Farzad Forughi, Yunshan Zhang, and Mu Chiao, “Design of a High-Resolution Pneumatic PDMS MEMS Actuator Using Genetic Algorithm Closed Loop Controller,” 2019.

---

\* Authors contributed equally and sorted alphabetically.

A version of the presented thesis with the focus on the optical system, and the combination of both pneumatic and piezoelectric actuator has been submitted for a peer reviewed journal article:

- ❖ **Ali Moallemi\***, Ran Fan\*, Amir Farzad Forughi, Yunshan Zhang, and Mu Chiao, “Design of a Novel Pneumatic PDMS MEMS Actuator Using Machine Learning Closed Loop Controller for Early Gastrointestinal Cancer Detection,” 2019.

---

\* Authors contributed equally.

# Table of Contents

Abstract .....	iii
Lay Summary .....	iv
Preface .....	v
Table of Contents .....	vii
List of Tables .....	xii
List of Figures.....	xiv
List of Symbols .....	xviii
Acknowledgments.....	xxiii
Dedication.....	xxiv
<b>Chapter 1: Introduction .....</b>	<b>1</b>
1.1 Cancer Statistics and Early Cancer Diagnosis.....	1
1.2 Imaging Techniques for Early Cancer Detection .....	2
1.3 MEMS and MOEMS.....	9
1.4 MEMS Technology for Confocal Applications.....	10
1.4.1 Electrostatic Actuators .....	11
1.4.2 Electromagnetic Actuators.....	12
1.4.3 Piezoelectric Actuators.....	14
1.4.4 Thermal Actuators.....	15

1.4.4.1	Shape Memory Alloy (SMA) Actuators.....	16
1.4.5	Fluid power actuators.....	17
1.4.5.1	Hydraulic Actuators.....	17
1.4.5.2	Pneumatic Actuators.....	18
I.	Pneumatic Balloon Actuators (PBAs).....	18
II.	Pneumatic Bellow Actuators.....	20
III.	Pneumatic Artificial Muscle (PAM) Actuators.....	22
IV.	Pneumatic Membrane Actuators.....	23
1.4.6	Concluding Remarks and Objectives.....	25
<b>Chapter 2: Design and Analysis of a PDMS MEMS Actuator .....</b>		<b>26</b>
2.1	Selection of Materials.....	26
2.1.1	Microstructure of PDMS.....	26
2.1.2	PDMS Samples for Experimental Research.....	27
2.1.3	PDMS Preparation Procedure.....	27
2.1.4	Properties of PDMS.....	28
2.1.5	PDMS as a Nonlinear Hyperelastic Material.....	29
2.2	PDMS Membrane Actuator .....	30
2.2.1	Working Principle of a Pneumatic Membrane Actuator.....	30
2.2.2	Theoretical Analysis of Membrane Actuator .....	31
2.2.3	Design of the Membrane Actuator .....	32

<b>Chapter 3: Experimental Setup and Methodology</b> .....	<b>34</b>
3.1 Experimental Setup and Electronic System .....	34
3.1.1 Manual Basic Control .....	35
3.1.1.1 Selection of Components for Manual Basic Control Circuit .....	35
3.1.1.2 Assembling the Manual Basic Board .....	36
3.1.1.3 Guideline for Manual Basic Testing/Control .....	37
3.1.2 Advanced Control .....	37
3.1.2.1 Selection of Components for Advanced Control Board .....	37
3.1.2.2 Assembling the Advanced Control Circuit.....	38
3.1.2.3 Guideline for Advanced Testing/Control.....	40
3.2 System Calibration .....	41
3.2.1 Optical Setup.....	41
3.2.2 Methodology for System Calibration .....	42
3.2.3 Laser Doppler Vibrometer (LDV) .....	45
3.2.4 Optical Instrumentation and Resolution .....	45
3.3 Control System .....	48
3.3.1 System Identification .....	48
3.3.1.1 Linear Parameter Varying (LPV) systems.....	50
3.3.1.2 LPV Model Structures .....	51
3.3.1.3 Linearization Through LPV Modeling.....	52

3.3.2	Feedback Control.....	53
3.3.2.1	PID Controller .....	56
3.3.2.2	Genetic Algorithm.....	56
3.3.2.3	Design of PID Controller Using Genetic Algorithm Technique.....	58
3.4	Image Quality .....	59
3.4.1	Image Quality Assessment (IQA) Techniques .....	59
<b>Chapter 4: Results and Discussion.....</b>		<b>63</b>
4.1	System Identification Experimental Results.....	63
4.1.1	Closed Loop Controller Experimental and GA Results .....	65
4.1.2	Effect of the Proposed PID Controller on the System .....	68
4.2	Experimental, Analytical and Simulation Results .....	72
4.3	Imaging Results .....	77
4.3.1	2D Images.....	77
4.3.2	3D Images.....	80
<b>Chapter 5: Conclusion and Future Work.....</b>		<b>81</b>
<b>Bibliography .....</b>		<b>84</b>
<b>Appendices.....</b>		<b>99</b>
Appendix A (Balloon (Cantilever) Actuator) .....		99
A.1	Working Principle of Pneumatic Balloon Actuators.....	99
A.2	Design Concept of the Pneumatic Balloon Actuator .....	100

A.3	Theoretical Analysis of Pneumatic Balloon Actuator .....	102
A.4	FEM Modeling.....	104
A.5	Experimental, Analytical and Simulation Results .....	105
Appendix B (PDMS Preparation Procedure).....		107
Appendix C (Electronic System and Components) .....		110
C.1	Electronic System .....	110
C.2	Selection of Components for Manual Basic Control Circuit.....	111
C.3	Valve characterization .....	115
Appendix D (Principles of Operation of LDV) .....		118
Appendix E (Genetic Algorithm Code) .....		120
Appendix F (Dynamic Response Considerations) .....		125

## List of Tables

Table 1.1 Stages of stomach cancer and its 5-year observed survival rate [10, 11].	2
Table 1.2 Summary of imaging techniques.	4
Table 1.3 Summary of state-of-the-art laser scanning confocal technologies (RCM/FCM).	6
Table 1.4 Summary of different types of typical MEMS actuators.	25
Table 2.1 Basic material properties of PDMS.	28
Table 2.2 The dependency of PDMS elastic modulus and mass density on the base/agent ratio [114, 118, 119].	28
Table 2.3 Second-order Ogden material parameters for hyperelastic model (15:1 PDMS) [124].	30
Table 3.1 Key features of Arduino ATmega 2560.	35
Table 3.2 Coefficients of the displacement-pressure equation.	44
Table 4.1 Transfer function parameters of the first-order system for different air pressure.	63
Table 4.2 Updated transfer function parameters for different air pressure.	64
Table 4.3 PID parameters of the general form of a PID controller for different air pressure.	65
Table 4.4 Parameters used in the genetic algorithm.	66
Table 4.5 PID parameters obtained by genetic algorithm and other methods.	67
Table 4.6 Scale of onion images epidermis with- and without PID controller evaluated by NR algorithms.	79
Table A.1 Geometrical dimensions of the pneumatic balloon actuator.	100
Table C.2 Key features of the pressure sensor.	111

Table C.3 Key features of the solenoid valve.....	112
Table C.4 Key features of the proportional valve.....	113
Table C.5 Key features of the manifold.....	114
Table C.6 Coefficients of the proportional valve characterization.....	117

## List of Figures

Figure 1.1 Comparison of resolution and penetration depth of various optical microscopy techniques [31].....	4
Figure 1.2 Basic principle of confocal microscopy.....	6
Figure 1.3 Optical configuration of the MEMS confocal engine. Optical fiber serves as a pinhole and scans in X and Y directions (Y-axis is pointing out of the page). The collimating lens (L1) is at a fixed position, while the objective lens (L2) is scanning in Z-direction [40]. .....	8
Figure 2.1 2D schematic view of a horizontal circular plate firmly clamped in a horizontal direction.....	30
Figure 2.2 Modeling of the (a-c) two-channel and, (d) one-channel membrane actuator.....	32
Figure 2.3 (a) 3D printed mold for one-channel small-scale membrane actuator, (b) The assembly of small-scale membrane actuator with PDMS and tubing, (c) The assembly of large-scale membrane actuator with PDMS, (d) The assembly of two-channel membrane actuator with all frames, connectors, and air tubing.....	33
Figure 3.1 Wiring diagram of the manual basic board.....	36
Figure 3.2 Active low pass filter.....	38
Figure 3.3 Precision voltage to current converter.....	39
Figure 3.4 Wiring diagram and the assembled voltage to current converter board.....	40
Figure 3.5 Optical setup for system calibration.....	41
Figure 3.6 Displacement as a function of the laser power.....	42

Figure 3.7 Pressure as a function of the voltage for different PDMS membrane thicknesses: (a) 0.25 mm, (b) 0.45 mm, and (c) 0.75 mm. ....	43
Figure 3.8 Schematic diagram of the proposed imaging system. ....	46
Figure 3.9 Full assembly of the actuators, control and optical system. ....	46
Figure 3.10 Assembly of the probe, actuators and lenses: (a) Pneumatic actuator, (b) Piezoelectric actuator, (c) Objective and collimating lens, (d) Assembly of the objective lens .....	47
Figure 3.11 The system identification loop [130, 132]. ....	49
Figure 3.12 LPV vs. LTI vs. LTV systems. ....	51
Figure 3.13 Typical components of a feedback control loop. ....	53
Figure 3.14 Block diagram of a basic feedback loop. ....	53
Figure 3.15 Simplified block diagram of a basic feedback loop. ....	55
Figure 3.16 Flow diagram of a genetic algorithm. ....	57
Figure 3.17 Chromosome definition .....	59
Figure 4.1 Effect of the proposed PID controller at high-pressure setpoint of $P = 125$ kPa. ....	68
Figure 4.2 Effect of the proposed PID controller at low-pressure setpoint of $P = 4$ kPa. ....	68
Figure 4.3 Effect of using other random PID controller parameters ( $P = 90$ kPa) for a specific setpoint ( $P = 4$ kPa). ....	69
Figure 4.4 Effect of using other random PID controller parameters ( $P = 90$ kPa) for a specific setpoint ( $P = 30$ kPa). ....	70

Figure 4.5 Tracking the displacement of the PDMS actuator and effect of the proposed PID controller at setpoint of $P = 125$ kPa.....	71
Figure 4.6 Tracking the displacement of the PDMS actuator and effect of the proposed PID controller at setpoint of $P = 4$ kPa.....	71
Figure 4.7 2D model of the membrane actuator. ....	73
Figure 4.8 The large-scale membrane actuator (a) before, and (b) after actuation. ....	73
Figure 4.9 Effect of the PDMS ratio (PR) on the deflection of the membrane actuator. ....	74
Figure 4.10 Experimental, theoretical, and simulation results for 0.45 mm thickness membrane actuator.....	75
Figure 4.11 Comparison of membrane actuators with various membrane thickness.....	77
Figure 4.12 Confocal images of (a) paper fiber, and (b) onion epidermis at a specific fixed Z-depth and different air pressures. ....	78
Figure 4.13 Confocal images of onion epidermis with (a), and (b) without PID controller. ....	78
Figure 4.14 3D images of paper fiber with the PID controller. ....	80
Figure 5.1 3D printed design of a future four-channel MEMS actuator. ....	83
Figure A.1 Concept design of pneumatic balloon actuator: (a) Modeling diagram of the balloon actuator, (b) Photograph of fabricated balloon actuator with geometries listed in Table A.1, (c) 3D printed mold for fabrication of PDMS balloon actuator.....	101
Figure A.2 Modeling of the inflated arc after injecting the air pressure inside the channel.....	103
Figure A.3 3D modeling of the balloon actuator.....	104

Figure A.4 The balloon actuator (a) before, and (b) after actuation. ....	105
Figure A.5 Experimental, analytical and simulation results for the balloon actuator.....	106
Figure C.1 Schematic wiring diagram of the advanced control board and the voltage to current converter board. ....	115
Figure C.2 Proportional valve characterization. ....	116
Figure C.3 Relationship between the input PWM voltage and the valve current. ....	117
Figure D.1 Basic components of a Laser Doppler Vibrometer [156]. ....	118
Figure F.1 Schematic of the pressure-transmitting system.....	125
Figure F.2 The effect of length of the tube on the pressure drop.....	127
Figure F.3 The effect of the length of the tube by applying an impulse response. ....	128
Figure F.4 Response of the PDMS actuator due to the step function. ....	128

## List of Symbols

$\alpha$	Radian of the inflated arc	[ <i>rad</i> ]
$\alpha_i$	Ogden stain energy density function parameter	[–]
$\alpha_{bv}$	The angle between the laser beam and the velocity vector	[ <i>rad</i> ]
$\Delta P$	Pressure drop	[ <i>kPa</i> ]
$\varepsilon$	The strain of the stretched PDMS	[–]
$\zeta$	Dummy parameter for $\dot{x}$ , i.e. $\dot{x} = \zeta$	[–]
$\lambda_i$	Principal stretching ratio	[–]
$\lambda_{wt}$	The wavelength of the light	[ <i>nm</i> ]
$\mu$	Possibly state dependent parameter vector	[–]
$\mu_d$	Dynamic viscosity of the fluid	[ <i>kg.m<sup>-1</sup>.s<sup>-1</sup></i> ]
$\mu_i$	Ogden stain energy density function parameter	[ <i>MPa</i> ]
$\nu$	Poisson's ratio	[–]
$\rho$	Fluid density	[ <i>kg.m<sup>-3</sup></i> ]
$\sigma$	The stress of the stretched PDMS	[ <i>Pa</i> ]
$\phi$	Phase angle	[ <i>rad</i> ]
$\omega$	Frequency of the fluctuating pressure in the pressure-transmitting system	[ <i>Hz</i> ]
$\omega_n$	Natural frequency	[ <i>Hz</i> ]
$a$	The diameter of air channel in the balloon actuator	[ <i>mm</i> ]
$a_p$	The radius of the circular plate	[ <i>m</i> ]
$a_s$	Coefficient of the transfer function for the control system	[–]

$A(\mu)$	An LPV Parameter	[–]
$b$	Distance between the edge of the balloon actuator and the center of the embedded lens	[ <i>mm</i> ]
$b_s$	Coefficient of the transfer function for the control system	[–]
$B(\mu)$	An LPV Parameter	[–]
$c$	Length of the air channel inside the balloon actuator	[ <i>mm</i> ]
$c_s$	Coefficient of the transfer function for the control system	[–]
$C(\mu)$	An LPV Parameter	[–]
$C(s)$	The transfer function for the controller	[–]
$d$	The diameter of the mounted lens embedded in the balloon actuator	[ <i>mm</i> ]
$d_s$	Load disturbance signal	[ <i>V</i> ]
$d_u$	Coefficient of the updated transfer function for the control system	[–]
$D$	Deflection of the actuator	[ <i>um</i> ]
$D(\mu)$	An LPV Parameter	[–]
$D_s$	Laplace transforms of $d_s$	[–]
$e$	Distance between the tip of the balloon actuator and the center of the embedded lens	[ <i>mm</i> ]
$e_1$	Distance from the center of the air channel to the neutral axis of the beam	[ <i>m</i> ]
$e_2$	Distance from the middle height of inflated arc to half of the height of the actuator	[ <i>m</i> ]
$e(t)$	Difference between a desired setpoint and a measured process control variable	[ <i>V</i> ]
$E$	Elastic modulus	[ <i>MPa</i> ]
$f_b$	Carrier frequency	[ <i>Hz</i> ]

$f_d$	Modulation frequency	[Hz]
$f_o$	Frequency of laser source or reference beam	[Hz]
$f_t$	Frequency of measured beam	[Hz]
$f(t)$	Step input	[V]
$G(s)$	The transfer function for the control system	[-]
$G^*(s)$	The updated transfer function for the control system	[-]
$h$	Height of the balloon actuator	[mm]
$h_d$	Damping ratio	[-]
$h_p$	The thickness of circular plate	[m]
$I$	Moment of inertia of a beam	[m <sup>4</sup> ]
$k$	Height of the inflated arc	[m]
$k_s$	A constant in the step input function	[V]
$K_d$	Derivative term of the PID controller	[-]
$K_i$	Integral term of the PID controller	[-]
$K_p$	Proportional term of the PID controller	[-]
$l$	Length of the balloon actuator	[mm]
$L_t$	Length of the tube	[m]
$m$	The upper layer thickness of PDMS in the balloon actuator	[mm]
$M$	The local bending moment resulted from air pressure	[N.m]
$M_{ac}$	The moment generated by the air channel of the original area	[N.m]
$M_{ia}$	The moment generated by the extra area (inflated arc)	[N.m]

$n$	The lower layer thickness of PDMS in the balloon actuator	[ $mm$ ]
$n_p$	PDMS base/curing agent weight ratio	[ $-$ ]
$n_{ri}$	the refractive index of the medium	[ $-$ ]
$n_s$	Nose signal	[ $V$ ]
$N$	Ogden stain energy density function parameter	[ $-$ ]
$N_s$	Laplace transforms of $n_s$	[ $-$ ]
$NA$	The numerical aperture of the objective lens	[ $-$ ]
$P_0$	The amplitude of the pressure signal in the source	[ $kPa$ ]
$P$	Air pressure	[ $kPa$ ]
$PH$	Pinhole or core diameter of the optical fiber	[ $m$ ]
$PR$	PDMS ratio	[ $-$ ]
$r_s(t)$	Reference signal	[ $V$ ]
$r_e$	An external signal	[ $V$ ]
$r_t$	The radius of the tube	[ $m$ ]
$R$	The local curvature radius of the beam	[ $m$ ]
$R_{ia}$	The radius of the inflated arc	[ $m$ ]
$R_s$	Laplace transforms of $r_s$	[ $-$ ]
$s$	Laplace variable	[ $-$ ]
$S$	The extra area of inflated arc after injecting air into the cavity	[ $m^2$ ]
$t$	The thickness of the upper-layer of the actuator before injecting air into the cavity	[ $m$ ]

$t'$	The thickness of the upper-layer of the actuator after injecting air into the cavity	[ $m$ ]
$T$	Temperature	[ $K$ ]
$u(t)$	Input signal	[ $V$ ]
$U_s$	Laplace transforms of $u$	[ $-$ ]
$v(t)$	The velocity of the object	[ $m.s^{-1}$ ]
$V$	Voltage signal	[ $V$ ]
$V_c$	The volume of the chamber at the end of the tube	[ $m^3$ ]
$V_s$	Velocity of sound	[ $m.s^{-1}$ ]
$w$	Width of the balloon actuator	[ $mm$ ]
$w(t)$	Outer disturbances signal	[ $V$ ]
$W$	Energy density function	[ $N.m$ ]
$W_1$	Overshoot weight for the cost function of the genetic algorithm	[ $-$ ]
$W_2$	Rise time weight for the cost function of the genetic algorithm	[ $-$ ]
$W_3$	Stability weight for the cost function of the genetic algorithm	[ $-$ ]
$x(t)$	State signals	[ $V$ ]
$\dot{x}$	First order differentiation of the state signals ( $x$ )	[ $-$ ]
$X_s$	Laplace transforms of $x$	[ $-$ ]
$y(t)$	Output signal	[ $V$ ]
$Y_s$	Laplace transforms of $y$	[ $-$ ]

## Acknowledgments

This thesis would not have been possible without inspiration, support and guidance of my research advisor, Dr. Mu Chiao. I would like to express my sincere appreciation to him for giving me the honor of working in the MEMS research group, and for his continuous optimism, patience, enthusiasm, and encouragement.

I also would like to thank my thesis committee members, Dr. Ryozo Nagamune, and Dr. Xiaoliang Jin for their time and valuable comments.

I cannot find words to express my gratitude to my friend Amir Farzad Forughi, and to my brother, Mohammad, for their endless help and perfect suggestions regarding the electronic system in this thesis, and for their patience with my endless questions. Also, I would like to thank my friends Ran Fan and Yunshan Zhang for their kind help for providing the optical system. I am forever thankful to my friends Roozbeh Yousefnejad and Amin Arefi for their great help with fluid mechanics analysis in my research. It is a pleasure to thank my friends Shayan Kayvan Majd, Mohammadreza Rostam, Ali Shademani, Hamed Helisaz, and Nima Negarandeh for their fantastic support during crucial time of writing my thesis.

Finally, my deepest gratitude and special thanks are owned to my family for their continuous and unparalleled love, help and support. I am forever indebted to my parents and my brothers who have supported me throughout my years of education and for giving me the opportunities and experiences that have made me who I am. They stood by me and supported me in every way, which made this thesis possible.

## Dedication

To my beloved parents,

for their continued love;

To my brothers, Mohammad and Reza,

for their endless supports & sacrifices;

&

To my best friend, Shayan,

for his unconditional support;

who selflessly encouraged me to explore new directions in my life and seek my own destiny. This journey would not have been possible if not for them, and I dedicate this milestone to them.

# Chapter 1: Introduction

## 1.1 Cancer Statistics and Early Cancer Diagnosis

Cancer is a leading cause of death worldwide with about 1 in 6 deaths due to cancer. It led to approximately 9.6 million deaths in 2018 [1, 2]. The economic impact of cancer is remarkable and in 2010, the total annual economic cost of cancer was around \$1.16 trillion. The most common causes of cancer that lead to death are cancers of lung (1.76 million deaths), colorectal (862,000 deaths), stomach (783,000 deaths), liver (782,000 deaths), and breast (627,000 deaths). Gastrointestinal (GI) cancers including cancers of the colon and rectum, esophagus and stomach, liver, gallbladder, pancreas, small intestine, appendix, and anus, collectively represent one of the greatest public health issues worldwide. The latest data from 2013 shows that GI cancer resulted in almost 4.5 million global deaths. American Cancer Society reported that GI cancers have the highest incidence and are the second leading cause of cancer death (after lung cancer) in the US [3]. According to the Canadian Cancer Society, the 2<sup>nd</sup> and 3<sup>rd</sup> cause of death of Canadian men and women, respectively, is cancer [4, 5].

According to researchers, only 1 in 5 low- and middle-income countries have enough and necessary data to detect cancer. Late-stage cancer diagnosis and treatment are common worldwide. Low-income countries reported that in 2017, only 26% of them have public available pathology services for cancer. Cancer treatment services are available in more than 90% of high-income countries compared to less than 30% of low-income countries. Unfortunately, fewer than half of cancer cases amongst people in Canada are identified at the earliest most curable stages [6].

If GI cancer is diagnosed in the early stages, the probability of surviving will improve significantly. Currently, white light endoscopy is used to detect the GI cancer, and clinical decisions are made according to the biopsies obtained from areas with abnormal morphological or color appearance [7]. The drawback of this strategy is that early cancerous lesions have subtle changes in color and

morphology. Therefore, white light endoscopy cannot detect GI cancer definitively in the early stages. Oversampling is often required to improve the probability of surviving GI cancer and minimize false negative results; however, it has significant adverse effects on patients [8].

According to Table 1.1, the stage 1 (1A) of the stomach cancer should be considered to reach to the highest rate of 5-year observed survival (early cancer diagnosis). In stage 1, the tumor penetrates through the thickness of the mucosa layer. The surface of the mucosa is smooth, soft, and velvety. Based on the literature review, the thickness of the mucosa layer is reported less than 850  $\mu\text{m}$  [9].

**Table 1.1 Stages of stomach cancer and its 5-year observed survival rate [10, 11].**

Stage	5-year observed survival rate
1 (A)	71%
1 (B)	57%
2 (A)	46%
2 (B)	33%
3 (A)	20%
3 (B)	14%
3 (C)	9%
4	4%

In the following section, some techniques for imaging of biological tissues are presented:

## 1.2 Imaging Techniques for Early Cancer Detection

In-vivo non-invasive methods could be a potential solution for improving early cancer detection. Optical microscopy could provide morphological and microstructural information for visualization and quantitative measurement of biological samples. This information could be utilized for improving early cancer detection.

Spectroscopy has various applications in biomedical spectroscopy in the areas of medical imaging and tissue analysis. Spectroscopy is the study of the interaction between matter and electromagnetic radiation [12, 13]. Spectroscopic technologies such as Raman [14] examine the composition, and physical structure of matter to be investigated at the atomic scale, molecular scale, and macro scale but to a lesser extent tissue morphology. Biochemical information is complementary to micro-morphology information acquired from endomicroscopy. Both contribute to improving GI cancer detection. Spectral analyses including reflectance, fluorescence, and Raman [14] have all been implemented for in-vivo endoscopy measurements.

Endomicroscopy is a technique for obtaining histology-like images from inside the human body, and this process is known as *optical biopsy* [15–18]. Major pre-clinical applications are in the gastrointestinal tract, tumors margin detection, live imaging of cartilage and tendon, etc. It provides real-time in-vivo tissue micro-morphology images that are directly related to the gold-standard histopathology images, without the need to excise the tissue. Histopathology diagnosis of excised tissue during endoscopy is the observation of the size and spatial arrangement of the nuclei, and vascularization patterns within the tissue. Therefore, the histopathologist could determine the phenotype of the tissue. Microendoscopy technology is capable of looking below the mucosal surface and seeing in-vivo histology of lesions during ongoing endoscopy [19]. Some of the most important optical microscopy techniques for non-destructive imaging of biological tissues are Optical Coherence Tomography (OCT) [20, 21], Multi-Photon Microscopy (MPM) [22, 23], Reflectance-mode Confocal Microscopy (RCM) [24, 25], and Fluorescence-mode Confocal Microscopy (FCM) [26, 27]. Table 1.2 presents some technologies under development for improving GI cancer detection.

**Table 1.2 Summary of imaging techniques.**

Techniques	Resolution	Fluorescence Dye	Spectral Information	Morphology Information
FCM [19]	1 $\mu m$	Yes	No	Yes
MPM [28]	1 $\mu m$	No	No	Yes
OCT [29]	10 $\mu m$	No	No	Yes
Raman [14]	1 mm	No	Yes	No
RCM [30]	1 $\mu m$	No	No	Yes

Images obtained by these techniques provide high-resolution morphological information. Figure 1.1 compares imaging resolution and penetration depth of some optical imaging techniques [31]. Considering the thickness of the mucosa layer, the MPM, Confocal Microscopy (CM), and to some extent OCT techniques would be the best fit for early cancer detection.

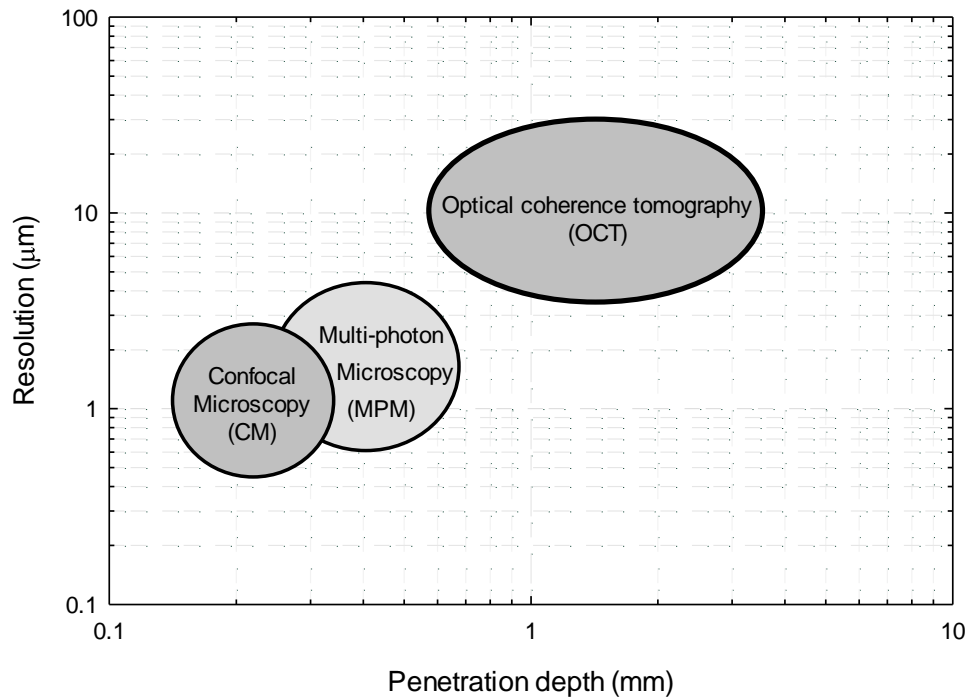


**Figure 1.1 Comparison of resolution and penetration depth of various optical microscopy techniques [31].**

OCT is a well-developed method, providing cross-sectional imaging of microstructures in various materials including biological tissue [29]. Although the penetration depth of OCT makes it more capable of determining the stages of invasive cancers (relatively large imaging depth ( $\sim 2\text{ mm}$ ) and field of view (FOV)), the low spatial resolution ( $10\text{-}15\ \mu\text{m}$ ) of this technique is not enough for early GI cancer detection. Multi-Photon Microscopy uses 2D micromirrors or optical fiber scanners to provide cross-sectional images by scanning the light beam in a horizontal plane (parallel to the surface of tissue). MPM has a higher resolution ( $\sim 1\ \mu\text{m}$ ) compared to OCT but the penetration depth (up to  $1\text{ mm}$ ) is smaller than OCT and larger than FCM and RCM. The drawbacks are that it is expensive, and a femtosecond (fs) laser is required as the light source. Moreover, it is almost difficult to be miniaturized for endoscopy applications. Therefore, the focus of this study is confocal endomicroscopy technology for improving early GI cancer detection. Confocal imaging (both RCM and FCM) is capable of providing cell-level microscopic images. This is also more feasible for miniaturization compared to MPM for endomicroscopy clinical applications.

The confocal microscopy technique provides a very high resolution close to MPM and cellular morphology images. Although CM has limited imaging depth ( $\sim 0.2\text{ mm}$ ), this penetration depth is sufficient for the detection of many diseases such as early epithelial cancers. CM works based on the rejection of out-of-focus light using a pinhole that enables optical sectioning of samples, and enhances imaging resolution and contrast. Confocal microscopy can be categorized as RCM or FCM. It should be noted that RCM does not require exogenous contrast fluorescence agents, but FCM does. These contrast agents bring additional drug administration procedures and complications. Moreover, RCM could provide images with deeper layers within the tissue, because higher light penetration depth is achievable by RCM imaging (near infrared (NIR) laser illumination) compared to FCM (visible wavelength laser excitation). Therefore, clinicians prefer RCM for GI diagnostic applications, and predominately use it for skin cancer investigations and diagnosis [32–34]. Table 1.3 summarizes some of the confocal microscopic technologies:

**Table 1.3 Summary of state-of-the-art laser scanning confocal technologies (RCM/FCM).**

Research Groups	Ref. [34]	Ref. [35]	Ref. [36]	Ref. [37]
Mechanism	Fiber bundle	Mirror, lens	Mirror, fiber	Fiber
Resolution	1 $\mu m$	1 $\mu m$	3 $\mu m$	2 $\mu m$
Fluorescence Dye	Yes	No	No	Yes
Probe Diameter	2.6 mm	Unknown	Hand-held	5 mm
Field of View	(240 $\mu m$ ) <sup>2</sup>	(200 $\mu m$ ) <sup>2</sup>	(300 $\mu m$ ) <sup>2</sup>	(475 $\mu m$ ) <sup>2</sup>
Frame Rate (fps)	12	1	2	1
Image Plane	X-Y	X-Y	X-Y	X-Y
Feedback Control	No	No	No	No

Marvin Minsky proposed the original concept of confocal microscopy in 1957 [32–34]. CM is active in both life science research and industrial metrology. The typical configuration of a CM is represented in Figure 1.2. This optical setup has the following components: a beam splitter, two pinholes, an objective lens, a light source, and a detector. The entrance pinhole limits the field of the laser, while the exit pinhole rejects the out-of-focus light. The smaller pinhole improves the resolution of the system. However, it lowers the amount of light received by the detector. This system greatly reduces image blur due to light scattering and increases resolution [32–34].

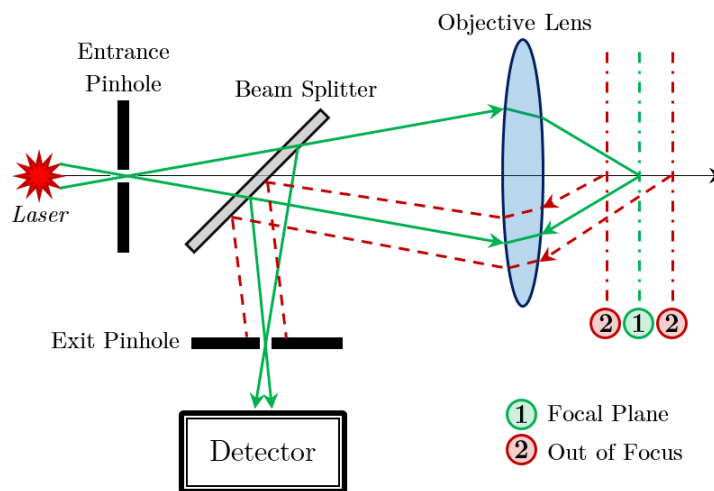


**Figure 1.2 Basic principle of confocal microscopy.**

The challenge for RCM is to miniaturize the device into a small catheter of a few millimeters size, and it is still at the investigational stage. RCM obtains imaging contrast from native tissue optical properties (different refractive index fluctuations in cells and other tissue microstructures). With RCM images, visualization of cell nuclei is feasible, and it could be possible to quantify their sizes and distributions. RCM can be used to estimate the staging of organs with cancer to reduce the number of biopsies [30].

According to Table 1.3, two main scanning mechanisms were employed in literature including 1) proximal, and 2) distal scanning. The former is associated with imaging fiber bundle, and the latter with mechanical structures and single fiber for light transmission.

In proximal approach, the scanning is performed outside of the endoscope at the proximal end of the fiber bundle. Small size imaging fiber bundles are readily available, making proximal scanning feasible for miniaturization. However, the main drawbacks of proximal scanning are that the reflections of the fiber bundle end faces and the occurrence of Rayleigh scattering phenomenon lead to the loss of lateral resolution and the loss of imaging contrast. Proximal scanning/fiber bundle based endomicroscopy imaging of in-vivo GI tissues by a catheter probe of 2.6 *mm* diameter, and a lateral resolution of 1  $\mu m$  has been reported in [17, 38]. However, the low contrast of the images is not suitable enough for cellular structure based diagnosis.

In the distal scanning approach, an exact and high-quality design is needed. Typically, the confocal imaging is performed at only one fixed depth within the tissue, and it would be almost difficult to design a continuous Z-depth scanning system. In the investigation of [34], an in-vivo skin imaging was demonstrated by using distal scanning approach, and the single fiber acted as both illumination pinhole and detection pinhole.

According to [39], for a good contrast and signal to noise ratio (S/N), the minimum imaging requirements to be capable of resolving individual cells are a lateral resolution of  $\sim 3 \mu m$  or less (preferably 1  $\mu m$ ) and an optical sectioning of approximately 10  $\mu m$  or better.

A unique optical configuration is proposed in Figure 1.3. In this configuration, an optical fiber serves as a pinhole in a confocal system, and simultaneously scans in X and Y directions (Y-axis is pointing out of the page). The input signal (illumination beam) and the output signal (collected optical tissue signal) will pass through this fiber. These two signals are in opposite directions. The collimating lens ( $L_1$ ) collimates the incident light coming from the pinhole. In the next step, the objective lens ( $L_2$ ) focuses the beam to a micron-sized spot inside the tissue. The collimating lens is fixed, and has a larger diameter compared to the objective lens ( $L_2$ ). Therefore, when the objective lens ( $L_2$ ) moves to different positions, it receives constant total illumination power. For confocal imaging, the elastically scattered laser light is collected by the objective lens ( $L_2$ ), and relayed back to the pinhole by the collimating lens ( $L_1$ ). It should be noted that the objective lens is scanning in the axial Z-direction. 3D images can be achieved by X-Y scanning of the fiber at incremental Z-depth.

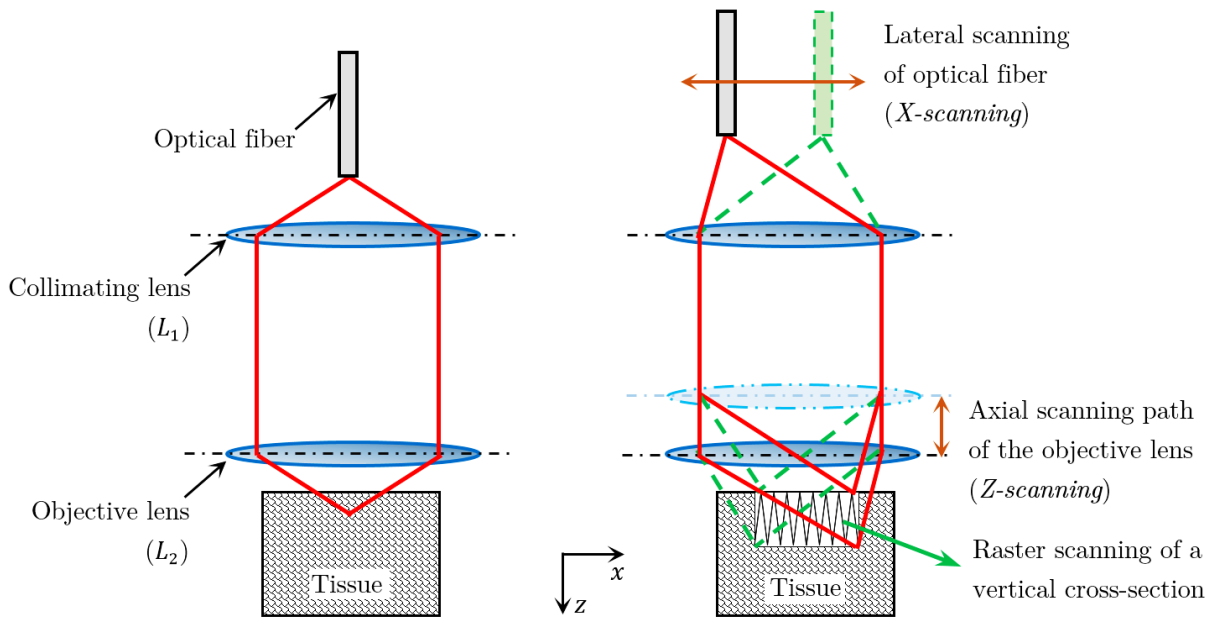


**Figure 1.3** Optical configuration of the MEMS confocal engine. Optical fiber serves as a pinhole and scans in X and Y directions (Y-axis is pointing out of the page). The collimating lens ( $L_1$ ) is at a fixed position, while the objective lens ( $L_2$ ) is scanning in Z-direction [40].

It would be challenging to bridge optical microscopy and clinical applications, because miniaturized laser beam scanning devices have to be designed and integrated into hand-held endoscopic catheters. Microelectromechanical Systems (MEMS) plays a crucial role in the fabrication of various micro-scanning systems for optical imaging modalities.

### **1.3 MEMS and MOEMS**

Microelectromechanical Systems (MEMS) is a process technology used to manufacture tiny integrated devices (e.g., sensors, actuators, and microsystems) that combine mechanical and electrical components [41]. While the electronics of the device are fabricated using computer chip IC technology, the micromechanical components are fabricated by sophisticated manipulation of silicon and other substrates using micromachining processes. Processes such as bulk and surface micromachining, as well as high-aspect-ratio micromachining (HARM), selectively remove parts of the silicon or add additional structural layers to form the mechanical and electromechanical components. While integrated circuits are designed to exploit the electrical properties of silicon, MEMS takes advantage of either silicon's mechanical properties, or both its electrical and mechanical properties. In the most general form, MEMS consists of mechanical microstructures, micro-sensors, micro-actuators and microelectronics, all integrated onto the same silicon chip [42]. With the advancement of MEMS technology, MEMS actuators and sensors are now commercially available, and it is now possible to integrate them into cost-sensitive commercial devices such as smartphones, shock monitoring equipment, robotics, etc [43]. These devices have the ability to sense, control and actuate on the micro scale, and generate effects on the macro scale. The interdisciplinary nature of MEMS utilizes design, engineering and manufacturing expertise from a wide and diverse range of technical areas including integrated circuit fabrication technology, automotive industry [44], biotechnology [45], wireless communications and electrical engineering [46], as well as fluid engineering, optics, instrumentation and packaging [47].

Micro-Opto-Electro-Mechanical Systems (MOEMS) is a combination of MEMS and micro-optics. MOEMS involves sensing or manipulating optical signals on a small size scale using integrated mechanical, optical, and electrical systems. MOEMS devices are MEMS devices combined with optical components such as mirrors [48] and lenses [49]. MOEMS has a wide variety of applications including optical switch, optical cross-connect, telecommunication [50], medical imaging [51], and consumer products [52]. These devices are usually fabricated using micro-optics and standard micromachining technologies using materials like silicon, silicon dioxide, silicon nitride, and gallium arsenide. Similar to MEMS, the smallest feature size of a MOEMS device usually ranges from a few microns up to a few millimeters.

#### **1.4 MEMS Technology for Confocal Applications**

Some research groups have worked on developing MEMS-based optical scanners for confocal and other imaging applications [53–56]. As explained in Chapter 1Chapter 1., most of these miniaturized scanners are based on reflective scanning through the angular rotation of micromirrors.

The UBC group proposed a transmissive scanning [57, 58] which deflects incident light by translating the refractive elements (i.e., lenses) directly off the optical axis. Transmissive scanners using moving lenses have alignment advantages, and result in smaller MEMS packages. In most existing MEMS-based confocal imaging approaches, Z-scanning ( $Z$  is the dimension into the tissue, while  $X$ - $Y$  plane is parallel to the tissue surface) is implemented by changing the focal length of the optical system. This leads to the disadvantage of spatial resolutions varying with depth. Transmissive scanners using moving lenses will move the laser beam's focal point inside the tissue without changing the focal length of the optical system. This not only results in constant spatial resolution regardless of different tissue depth, but also facilitates convenient Z-scanning in the MEMS confocal engine.

Typically, for optical microscopy, there are three fundamental types of laser beam scanners including optical fiber, lens, and mirror scanners. These types of scanners can be actuated through various actuation mechanisms, as it could be categorized by six primary types of actuators including Electrostatic, Electromagnetic, Piezoelectric, Thermal, Shape Memory Alloy (SMA), and Fluid Power (Pneumatic/Hydraulic) actuators.

#### **1.4.1 Electrostatic Actuators**

Electrostatic actuators rely on the force between two conducting electrodes. There are different types of actuators based on the arrangement of the conducting electrodes. When a voltage is applied between the electrodes, in case of the existence of the mutual capacitance, a nearly always-attractive force will be generated. Voltages of several hundred volts for electrostatic actuators are not uncommon which can be thought of as the main disadvantage of this type of actuator. Electrostatic actuators could be categorized as linear or rotary. The theory behind many of the rotary actuators is similar to their corresponding linear forms [12, 59].

One typical type of electrostatic actuator is based on two parallel electrodes (parallel-plate actuators). One electrode is fixed and the second one is capable of actuation in the electric field. Parallel-plate actuators can also be thought of as parallel-plate capacitors whose dielectric is a fluid. The most straightforward configuration consists of two plates, which are pulled together when a voltage is applied. This configuration is generally used to sense in the  $Z$ -axis sensing schemes. Due to the possibility of large capacitance areas, this configuration may result in very high sensitivity. However, the main disadvantage of this configuration is the non-linear force and sensitivity values (or highly nonlinear behavior of the angle of micro-mirror versus voltage curve), which occurs with the movement of one of the plates towards the other [60].

This actuator is a common approach for moving micro-mirrors, and mostly provides large mirror deflection. Weinberger et al. [61] designed a four-electrode arrangement that drives a micro-mirror for an optical micro-tracker system. In the proposed design, a laser beam is deflected by a micro-mirror and is detected by a Position-Sensitive Device (PSD) as a feedback position sensor. The PSD is mounted on a moving stage, and the mirror is actuated using a linear PID controller. According to the experiments, stage movements with a speed of up to  $80 \text{ mm.s}^{-1}$  are tracked over an angular range between  $0.8^\circ$  and  $12.3^\circ$ . For tilting the mirror, the angular velocity of about  $14.7^\circ/\text{s}$  is recorded. The presented scanner has a low first resonance frequency (rotational oscillation). The eigenfrequency of the rotational oscillation is about  $57 \text{ Hz}$ . The second eigenfrequency, which is a vertical oscillation of the mirror plate, is about  $1420 \text{ Hz}$ .

Another common type of electrostatic actuator is comb-shaped electrodes [62, 63]. For example, Fan et al. [63] presented a novel assembly method for an electrostatic vertical comb drive scanning. In the proposed design, the rotor and stator fingers are fabricated by using one mask lithography step, and the mirror wafer and mesa wafer are stacked up and assembled into a vertical comb drive mirror. In the resonant mode of the actuator, the mirror has a scanning angle of  $\pm 10.8^\circ$ . The resonance frequency of the mirror reported as  $393 \text{ Hz}$ .

#### **1.4.2 Electromagnetic Actuators**

Electromagnetic actuators convert electricity into magnetic force using the electromagnetic-mechanical principle. This magnetic force is used to move an object. For example, in the case of a solenoid valve, the magnetic force moves the spool or poppet, which in turn controls the direction of flow. Electromagnetic actuators produce force and torque using magnetic energy. Electromagnetic actuators have been commercialized in different engineering areas including robotics, energy, and biomedical engineering. These types of actuators have some advantages such as: 1) suitable force and work densities, 2) easily controllable, 3) the power source can be far away, and 4) power flow in both directions (possibility to use the actuators as generators for

braking function). Regarding the disadvantages of this type of actuator, it is not applicable to use electromagnetic actuators when their environment is not free of electromagnetic fields or interferences [64, 65].

Ju et al. [66] reported the design, fabrication, and analysis of an electromagnetic 2D scanning micro-mirror. The application of the presented study is for a high definition laser pico-projection display system with a packaged device volume of  $0.34 \text{ cm}^3$ . The device has a set of permanent magnets to generate a high magnetic field. This device is capable of providing a large deflection angle in the horizontal direction at resonance due to the design of a double gimbaled structure and angular deflection amplification mechanism [67]. The diameter size of the fabricated micro-mirror is  $1.2 \text{ mm}$ . This micro-mirror is capable of scanning at the maximum angle of  $52^\circ$  at  $28.9 \text{ kHz}$  and  $33^\circ$  at  $60 \text{ Hz}$  for horizontal and vertical scanning, respectively.

Kim et al. [68] presented an electromagnetic actuator for the 2D scanning micro-mirror with large aperture and tilting angle. The micro-mirror has a plate size of  $3 \text{ mm}$  diameter, and is fabricated on a SiOG (Silicon on Glass) wafer using four photolithography masks. Permanent magnets are used to provide a radial magnetic field. Horizontal and vertical resonance frequencies of the micro-mirror are  $1421 \text{ Hz}$  and  $396 \text{ Hz}$ , respectively. For the horizontal scan, the resonance scan angle of  $24.45^\circ$  at the input signal of  $48 \text{ mA}_{pp}$  is measured. The maximum vertical scanning angle is recorded as  $26.32^\circ$  with the cylindrical magnet diameter of  $4.0 \text{ mm}$ , at  $60 \text{ Hz}$  sinusoidal input of  $640 \text{ mA}_{pp}$  signal.

### 1.4.3 Piezoelectric Actuators

For the first time, Jacques and Pierre Curie described piezoelectricity in 1880 [69]. When mechanical stress is applied to some solid materials such as crystals, electric charges (piezoelectricity) accumulate in the solid material [12]. The linear electromechanical interaction between the electrical and mechanical states in certain materials with crystalline non-symmetrical structure leads to the piezoelectric effect [70].

Piezoelectric actuators convert electrical to mechanical energy. Piezoelectric effect results in crystalline materials to expand when charges are applied. This effect is reversible, i.e., a deformation in a piezoelectric material generates electric charges. Piezoelectric actuators have a wide range of applications such as piezoelectric inkjet printing, amplification pickups for guitars, time reference source in quartz watches, etc. The piezoelectric behavior is highly nonlinear. However, linear equations are introduced in [71, 72] for describing the direct and inverse piezoelectric effect [65]. Piezoelectric actuators have some advantages compared to electromagnetic types as follows: 1) more applicable to miniaturization, 2) free of electromagnetic noise, 3) compact design (no need for a magnetic shield), and 4) higher efficiency (for the power range more than 30 W, the efficiency is insensitive to the size) [73].

For optical microsystem applications, Lei et al. [74] implemented an Aluminum Nitride (AlN) piezoelectric film for the fabrication of a large aperture MEMS scanning micro-mirror. A  $6\text{ mm} \times 4\text{ mm}$  large mirror plate is used in the proposed design. The experimental results showed a linear actuation relationship, and the good signal quality of the integrated angle sensors. In order to overcome the shortcoming of relatively low piezoelectric coefficients of AlN film and enlarge the optical scan angle, a leverage amplification mechanism and resonant amplification effect are employed. Two sinusoidal voltages with  $180^\circ$  phase difference were applied to the actuators and results revealed the micro-mirror scanning frequency of 898 to 906 Hz. According

to the experiments, applying 10  $V$  leads to the maximum optical scan angle and the resonance frequency of 902.05  $Hz$ .

Koh et al. [75] demonstrated a 2D scanning silicon micro-mirror controlled by piezoelectric actuators. A large ( $5\text{ mm} \times 5\text{ mm}$ ) and small ( $3\text{ mm} \times 3\text{ mm}$ ) micromirrors are used in the reported study. For both micro-mirrors, 2D raster scanning patterns are proposed. For the large micro-mirror, the first resonance frequency (bending mode) and the second resonance frequency (torsional mode) are measured at 34  $Hz$  and 198  $Hz$ , respectively. The optical angle of the micro-mirror at its slow scanning resonance peak reaches up to  $2.8^\circ$  at 10  $V_{pp}$ . For the small micro-mirror, the first (bending) and second (torsion) resonance frequencies are observed at 122  $Hz$  and 2460  $Hz$ , respectively.

#### 1.4.4 Thermal Actuators

Thermal actuators typically generate motion by thermal expansion. When the electric current flows through a thin beam, the temperature increases and the beam expands. The thermal expansion is small; therefore, it is often necessary to mechanically amplify the output to translate to a large amount of deflection that requires high temperatures. The internal temperature increase was caused by electrical resistive heating or a local heat source generator [75]. Thermal actuators are capable of deflecting in one direction. Typical inputs of the thermal actuators are 13  $V$  and 36  $mA$  [77], and the operating temperature is usually about  $600^\circ\text{C}$  [78, 79]. Considering the transient thermal gradients and its effect on the other parts of the system, they present some drawbacks in precision positioners. In addition, the stress in the beams is mostly compressive, and buckling results in failure of the beams [80].

Luo et al. [81] developed a large-piston scanning electrothermal micro-mirror using combined surface- and bulk- micromachining process. The position of the central mirror plate, which is supported by 16 three-level ladder bimorph actuators, could be controlled by the variation of the ambient temperature. A thermally-isolated frame with heaters and temperature sensors are

embedded in the presented design. Four annular Titanium (Ti) rings are placed side by side: two of Ti rings are heaters to generate a local temperature by applying a voltage, and the other two Ti rings are as temperature sensors to detect the variation of temperature by measuring resistance change. The mirror plate and chip size are  $1.4 \times 1.4 \text{ mm}^2$  and  $5.9 \times 5.9 \text{ mm}^2$ , respectively. The first and second resonance frequencies are  $523 \text{ Hz}$  and  $898 \text{ Hz}$ , respectively. The piston displacement reaches  $354 \text{ }\mu\text{m}$ . A PID controller is used to stabilize the local temperature.

#### 1.4.4.1 Shape Memory Alloy (SMA) Actuators

Ölander observed the shape memory effect in a gold-cadmium alloy in 1932 [82]. A shape-memory alloy (SMA) is a type of alloy that can recover its original shape. When the SMA is heated, it deforms and then returns to its pre-deformed form. According to the solid-solid phase transition of SMA (the reversible transformation from the martensite into the austenite), this behavior is produced in a given temperature interval[82]. SMA is a lightweight and solid-state material; therefore, it is exploited in several useful applications including medical equipment, aerospace, robotics, and biomedical engineering. SMA actuators have advantages such as easy miniaturization and flexible configuration but they present some disadvantages regarding their low speed, low efficiency, and their temperature dependency [65, 83].

AbuZaiter et al. [84] developed a new SMA micro-positioning stage monolithically micro-machined with a single fabrication step. It can be used to move a small object for microscopic scanning applications. In the presented square design of their device with dimensions of  $12 \text{ mm} \times 12 \text{ mm} \times 0.25 \text{ mm}$ , the three degrees of freedom movement of the moving stage is controlled by six SMA planar springs actuators. SMA actuators are driven independently by an electrical current that is controlled by an external Pulse Width Modulation (PWM) signal. The maximum stage movements of  $1.2 \text{ mm}$  and  $1.6 \text{ mm}$  along the X- and Y-directions, respectively and rotational movements of  $20^\circ$  are recorded.

### 1.4.5 Fluid power actuators

Generally, fluid power actuators are driven by an electric motor and the power of fluid flow is adjusted using pumps or compressors. The actuator converts the energy of the pressurized fluid into a mechanical variable such as stroke (angle of rotation), speed (rotatory speed), or force (torque) of linear or rotary motion. Fluid power actuators are predominately categorized according to the state of the fluid employed: 1) hydraulic actuators employ an incompressible liquid (usually oil), 2) pneumatic actuators employ a compressible gas (air) [65, 83]. In the real environment, regarding the existence of disturbances, a suitable feedback controller plays a crucial role in controlling the target variable and comparing it to the set point to avoid possible errors. Therefore, a considerable increase in the speed and accuracy of the actuator could be observed [83].

#### 1.4.5.1 Hydraulic Actuators

Hydraulic actuators have a relatively high pressure up to 40 *MPa* and relatively low flow velocities within the pipelines. It should be noted that in the presence of great pressure differentials at flow resistors or leakage gaps, high flow velocities could be observed which could affect control elements [83].

Hydraulic actuators have some advantages including: 1) high force and work densities in comparison with other actuators, 2) easy to control, and 3) the power source of energy can be far away relative to the actuator. The principal drawbacks of this actuator are: 1) considering the high pressure of the fluid, safety conditions are an important problem, and 2) the leakage of flow and impulse forces and their effects on the performance of the actuator [65].

### 1.4.5.2 Pneumatic Actuators

Lower pressure ranges up to 1 *MPa* are often used for pneumatic actuators and higher flow velocities within the pipelines are observed [83]. Pneumatic actuators present some advantages almost as same as the hydraulic actuators, but the force and work densities are not as high as the hydraulic actuators. Also, they are capable of working at higher temperatures compared to hydraulic actuators. However, pneumatic actuators have some drawbacks including: 1) high compressibility of the operating gas which prevents to work with high pressures, 2) not as fast as hydraulic actuators against disturbances, and 3) higher leakage of air pressure. The most important type of pneumatic actuators could be categorized as Balloon, Bellow, Artificial Muscle, and Membrane actuators.

#### I. Pneumatic Balloon Actuators (PBAs)

Hwang et al. [85] presented a PDMS pneumatic balloon actuator by fabricating 3D printed molds for trapezoidal vertical micro-balloon fins. They claimed that conventional balloon actuators have nonlinear behavior by applying air pressure. However, the presented balloon fins produced a linear response of bending angle under air pressure. Experimentally and analytically, the force and bending angle of the actuator are measured and compared to each other. In the proposed design, the bending angle is proportional to the injection air pressure. Using hyperelastic polymers such as PDMS, large deformation and bending angle would be achievable [86–88]. The introduced balloon actuator has a thin air channel embedded in a PDMS beam structure. It works according to the difference between the expansion of the thin top layer and a thick bottom layer. This results in an out-of-plane motion, which can be expressed by the ratio of the top-layer to bottom-layer thickness [87, 89, 90]. When the air channel is pressurized, the actuator bends towards the thicker layer side because of the pressurized air.

Konishi et al. [88] proposed a thin, flexible pneumatic balloon actuator. The cavity of the balloon actuator is formed by two thin, flexible films combined by a silicone rubber glue. Typically, researchers use different thickness for thin films, but in their study, different materials are utilized to produce different behavior. The upper film is made of silicon rubber as the membrane, and the lower one is a polyimide film as a substrate. By injecting the air pressure into the balloon, the end-effector bends. Therefore, the actuator would be capable of generating a large out-of-plane vertical deflection and horizontal displacement. Static and dynamic analysis are performed to show the capability of the actuator for providing large displacements and high forces. Utilizing PBAs, the motion of end-effectors is analyzed by a ciliary motion conveyance setup.

From theoretical and experimental points of view, Benjamin et al. [91] presented a biologically inspired pneumatic balloon micro-actuator based on an asymmetric deflection of two PDMS films. These layers have different thicknesses (or material properties) which are bonded together. An optimal beam-to-membrane thickness ratio in the range of 2 to 3 is used. Also, to fabricate the PBAs, an innovative method which is the combination of molding, micro-milling, and plasma bonding is introduced. 3D FEM models and measurements are studied to explain the behavior of the presented actuator. The experimental and FEM results are presented to verify the results of the modeling and a good agreement is observed to provide an appropriate description of the actuator behavior.

Zheng et al. [92] presented a double-layered pneumatic balloon actuator with tunable bending points. The proposed actuator has two different channels made of elastic silicon rubber. The upper channel composed of bismuth-based low-melting-point-alloy. This channel is for controlling the local stiffness of the actuator, but the lower channel is used for actuation by air pressure. Injecting the air into the channel results in inflation of the channel and bending of the actuator. A low-melting-point-alloy, which is solidified by temperature decrease, is embedded to control the local stiffness of the balloon actuator. Locally melting the alloy results in changing the position of the alloy, and then the bending points can be moved since the pneumatic actuator bends at soft

points. Therefore, there is no need to change the whole design of the actuator to change the bending point. The presented actuator and its mechanism could be used in designing highly flexible actuators for soft robotics.

Konishi et al. [93] designed a PDMS pneumatic micro-hand actuator as an end-effector of a robot. The actuator made of two PDMS membranes with a different mixing ratio of the base polymer and curing agent. The top PDMS layer is more rigid than the bottom one. The out-of-plane displacement of the actuator is observed by applying the air pressure into the actuator. In their design, different mixing ratios of PDMS layers are used to control the bending direction of micro-finger.

Gorissen et al. [94] introduced a new PDMS actuator which generates twisting deformations by applying air pressure into the actuator. The production, optimization, and performance testing of these actuators are studied to increase the twisting angle per actuator length. In their design of twisting actuators, two same arrays of PBAs are fabricated through soft lithography and are bonded back-to-back. Due to the asymmetric design, only one pressure supply is sufficient to actuate the twisting deformation. Moreover, four flexible pneumatic twisting actuators are combined into a tilting mirror-platform with two degrees of freedom (2-DOF).

## **II. Pneumatic Bellow Actuators**

Bütefish et al. [95] presented a pneumatic actuator utilizing a new actuation principle for micro-mechanical systems. This actuator can be used as a micro-gripper driven by two bellow-type micro-pneumatic actuators. The proposed actuator has some advantages including: 1) large deflection, 2) excellent dynamic behavior, 3) high generated mechanical forces, and 4) high design flexibility (usage of various working fluids). The overview of the micro-pneumatic actuator is a piston connected to the housing by two spring elements as sealing against the environment. The spring elements are used to move the piston by applying air pressure. The piston is attached to the gripper linkage to transmit the generated mechanical force. Based on the presented design,

one pneumatic actuator is utilized for opening, and one for closing the gripper. The optimization study for the shape of the spring elements is performed by FEM simulation. The mechanical failure of the spring elements is included in the optimization.

Shapiro et al. [96] presented a 1-DOF pneumatic actuator with large bending capabilities and compared it with several actuator designs. The introduced actuator has two materials with slightly different shear modules. Therefore, each of the materials tends to deform based on its stiffness by injecting air pressure into the bellows. Some dynamic properties and the effect of external loads (gravity) on the behavior of the actuator are studied. From the theoretical and experimental point of view, the behavior of the actuator is examined as well. A rapid-prototype polymer tube is utilized in this study, but according to their design, the same concept and methodologies would be applicable for other materials.

Yukisawa et al. [97] were interested in an extensible pneumatic actuator with bellows (EPAB) including two requirements: 1) large elongation strain, and 2) large operational pressure. The presented actuator has a rubber tube and a highly packed bellows sleeve. Regarding the verification of the presented model, the basic properties of four actuators with different parameters are observed. Two categories of experiments are performed: 1) constant pressure with variable length, and 2) constant length with variable pressure. Based on the experimental measurement, the proposed model is verified.

Drotman et al. [98] investigated a class of commercial 3D printed bending actuator with bellows. Considering the set of design parameters, the analytical models of the actuator to predict actuation behavior of bellows are investigated. For the three-chambered actuator, the forward and inverse kinematics are analyzed and experimentally validated using a motion capture system. To determine which of the geometric parameters have the greatest effect on bending and blocked force, a sensitivity analysis of the geometric parameters of the bellows is performed in this thesis.

Sudani et al. [99] proposed a new model of a miniature bellow pneumatic bending rubber actuator derived from statics and neo-Hookean elasticity. As a result, this actuator shows nonlinear behavior in input-output relation results from elastomer. The presented actuator could bend circularly in two directions. This model represents a relation between the bending angle of the actuator and the applied pressure. Using the operator theory and a control system, a nonlinear control feedback system for the actuator is designed. By tracking the control experiment, the performance of the actuator is verified for the feedback system.

### **III. Pneumatic Artificial Muscle (PAM) Actuators**

Li et al. [100] introduced an architecture for fluid-driven artificial muscles including a flexible skin, compressible skeleton, and a fluid medium. This type of actuator could present multiaxial motions including contraction, bending, and torsion. Developing a mechanical model, the interaction of these three components is elaborated. A rapid manufacturing method for low-cost artificial muscles is proposed using various materials at multiple scales. Fabrication of the actuator has these steps: 1) fabrication of the deformable skeletal structure, 2) preparation of the outer skin, and 3) assembly and sealing. This can be used in many working environments at multiple scales, such as miniature surgical devices, and wearable robotic exoskeletons.

Greer et al. [101] investigated the design and fabrication of a novel series pneumatic artificial muscle (sPAM) for a soft continuum robot. The basic working principle of the presented actuator is almost as same as tendons: a tension force is applied on the robot's pneumatic backbone by sPAMs, resulted in bending. sPAM and robot kinematics are modeled, and the results are experimentally confirmed. The closed-loop control is designed using an eye-in-hand visual servo control law and a step-response rise time and settling time of less than two seconds are observed.

Sarosi et al. [102] developed a new dynamic model for a pneumatic artificial muscle. Applying the air pressure, a nonlinear force is generated results in 2D motion of the PAM. An analytical analysis by applying the optimal parameter identification method to determine the parameters of the

acting force is performed. The model is experimentally tested and verified. According to their results, the stiffness and the damping are nonlinearly proportional to the displacement. In PAM due to loading, the self-excited vibrations occur.

#### **IV. Pneumatic Membrane Actuators**

Rodríguez et al. [103] introduced a micro-pressure source consisting of three parts: 1) a heating resistance built on a dielectric membrane, 2) air encapsulated at atmospheric pressure, and 3) an elastomer membrane with high elastic properties. The membrane is composed of PDMS. In the proposed design, in order to increase the air pressure, air should be heated. Due to the increase of air temperature, the elastic membrane deforms. The actuator performance with respect to the input electrical signal is predicted by formulating a simple, comprehensive system model. COMSOL® Multiphysics is used for the simulation of micro-balloon actuator. The result of the simulation on the micro-balloon actuator shows an appropriate fit with their experiments.

Rothmund et al. [104] presented an elastomeric valve that contains a bi-stable membrane as a mechanical latching or non-latching switch to control the air flow. A hemispherical membrane is utilized as the control element of the valve. The snap-through instability results in rapid transition between two stable states of the membrane. They claimed that the snap-upward pressure of the membrane differs from the snap-downward pressure and could be controlled by changing the material and geometry of the membrane.

Gabriel et al. [105] described an electrostatically driven, pneumatic actuator capable of generating surface-normal deflections. Two sealed concentric chambers shared a membrane. The chambers are connected by channels and made up the pneumatic actuator. The conducting substrate is considered as the fixed opposing electrode plate of an electrostatic actuator. On the other hand, the movable electrode plate is designed as the portion of the membrane suspended over the outer chamber. Applying voltage between the two plates results in the deflection of the outer-chamber membrane towards the substrate. Therefore, a decrease in the volume of the outer chamber could

be observed and increases pressure in both the outer and inner chamber. As a consequence of this process, the membrane over the inner chamber shows a deflection with respect to the position of the substrate.

Zhang et al. [106] investigated the working principles of pneumatic actuators and their applications in parachute systems for soft-landing and steering control. The 3D nonlinear structural dynamic behavior of the actuator is observed. Membranes composed of geometrically nonlinear anisotropic elements are used in their modeling. In order to validate the dynamic applications of the actuator, the inflation of a quasi-static pneumatic actuator is studied and compared with a 1D analytical solution. Also, a new finite element model for this type of actuator is presented. These simulations show the capability of the presented actuator as a useful control device in parachute systems.

Wu et al. [107] presented a robust design for manufacturing a PDMS-based micro-pump. Both theoretical and experimental analyses are performed. A good agreement is observed between the results of the theoretical model and experimental data for the deformation of the membrane. Furthermore, some experiments are conducted to evaluate the effect of flow rates, air pressures, and operation modes for the proposed micro-pump. The designed membrane is optimized by numerical simulations. According to their study, a micro-pump with a single- and double-sided flexible actuation could transport the sample stream.

### 1.4.6 Concluding Remarks and Objectives

The key contribution of this thesis is developing a pneumatic miniaturized high-resolution PDMS MEMS actuator. A feedback control mechanism should be designed to provide a stable position. According to the literature review, typical MEMS actuators are summarized in Table 1.4:

**Table 1.4 Summary of different types of typical MEMS actuators.**

MEMS Actuator	Displacement	Supply Voltage/Ampere	Frequency	References
Electrostatic	1 – 200 $\mu m$	100 V	$10^2 - 10^6$ Hz	[59–63], [108–111]
Electromagnetic	10 – 1000 $\mu m$	1 A	1 – $10^3$ Hz	[64–68], [108–111]
Piezoelectric	0.1 – 1000 $\mu m$	300 V	$10^2 - 10^5$ Hz	[69–74], [108–111]
Thermal	1 – 300 $\mu m$	50 V	1 – 100 Hz	[75–81], [108–111]
Shape Memory Alloy (SMA)	1 – 1000 $\mu m$	1 A	1 – 100 Hz	[82–84], [108–111]
Pneumatic	> 1 $\mu m$	10 V	1 – 100 Hz	[82–111]

Several driving mechanisms have been considered. According to Table 1.4, electrostatic and piezoelectric actuators have high frequency (fast response), but they need high voltage for actuation. Thermal actuators provide moderate displacement and have a slow response up to 100 Hz but a high level of voltage should be applied for actuation. Magnetic actuation has a fast speed, but the material has to include MEMS-process compatible ferromagnetic materials (e.g., electroplated nickel) and also, as same as SMA actuators, a high ampere should be provided for actuation. Our objective is to provide an actuator which has a displacement less than 100  $\mu m$ , low frequency (< 100 Hz), high resolution (< 5  $\mu m$ ), and be stable (PID controller). Therefore, we propose to use a pneumatic actuation for scanning. The available scanning lens which is used in this project has a size of ~6.0 mm diameter, but (as a future work) we envision that the final scanning lens can has a size of 1.0 mm diameter, while the collimating lens can be 1.25 mm. Therefore, designing an actuator with the diameter size of less than 2.5 mm would be appropriate.

## Chapter 2: Design and Analysis of a PDMS MEMS Actuator

In our proposed system, there were some geometrical and physical limitations regarding the usage of artificial muscle and bellow actuators. Moreover, these actuators have more complicated fabrication processes compared to balloon and membrane actuators. Therefore, in this research, two designs are developed for the PDMS MEMS actuator: balloon and membrane actuators. After conducting many experiments, we found that there were some disadvantages regarding the usage of balloon actuator, resulting in concentrating efforts on designing a membrane actuator. The balloon actuator showed a non-linear behavior compared to the membrane actuator, which makes controlling the actuator more complicated. Also, a higher range of air pressure should be injected to the balloon actuator to reach to a specific displacement. The fabrication process of this actuator is more difficult in comparison with the membrane actuator. It should be noted that the miniaturization of the balloon actuator would be more challenging to embed in a cylindrical tube. The design and analysis of our proposed balloon actuator are presented on Appendix A.

### 2.1 Selection of Materials

The material used in this research is Polydimethylsiloxane (PDMS). It is the most widely used silicon-based organic polymer. PDMS is inert, non-toxic, non-flammable, and optically clear. It has lots of applications, ranging from contact lenses and medical devices to elastomers. PDMS at high temperatures (long flow time) acts like a viscous liquid (viscoelastic). However, at low temperatures (short flow time) it acts like an elastic solid, similar to rubber [112–114].

#### 2.1.1 Microstructure of PDMS

The chemical formula of PDMS is  $CH_3[Si(CH_3)_2O]_nSi(CH_3)_3$  and  $n$  is the number of repeating monomer  $[Si(CH_3)_2O]$  units. The network of PDMS polymer is assembled by crosslinking these polymer chains. The long PDMS polymer chains usually have vinyl groups at each end. Polymethylhydro-siloxane is the short crosslinker which is used to link the PDMS chains [114].

### 2.1.2 PDMS Samples for Experimental Research

Sylgard™ 184 silicone elastomer base, and Sylgard™ 184 silicone elastomer curing agent are used in this research. A series of different base/agent ratios (i.e., different degrees of crosslinkers) are used for the experiments which are PDMS Ratio (PR) of 10:1, 15:1, and 20:1. The higher the degree of crosslinker, the stiffer the sample would be.

### 2.1.3 PDMS Preparation Procedure

In order to prepare PDMS, three main steps should be followed:

- I. The preparation of the mold,
- II. The scaling and mixing of the PDMS and the curing agent and degassing,
- III. The PDMS baking, peeling off the mold and bonding (if applicable)

The detailed procedure is available on Appendix B. The brief explanation of these steps are as follows [115]:

A mold was 3D printed with Miicraft® 50. After 3D printing the sample, the mold soaked in 2-Propanol (anhydrous 99.5%) for 20 *min*. Then, the mold was exposed to UV-light for 30 *min*. The most used PDMS is the Sylgard™ 184 Silicone elastomer and was used in this study. The weight ratio between the base and the curing agent can be changed to prepare a softer or harder PDMS for specific applications. In this study, different ratios of PDMS were used and compared with each other. To prepare the PDMS, the base and the curing agent should be mixed strongly. An automatic PDMS mixer was used (2 *min* mixing with 2000 *rpm*). For degassing procedure, first a centrifuge (2:30 *min* and 2200 *rpm*) and then, a vacuum pump (30 *min*) were used. For baking the PDMS, the set temperature of the oven should be selected based on the glass temperature of the mold container. We baked the PDMS at 80°C in an oven for 2–4 hours. When the mold and the PDMS reached room temperature, then to the PDMS was peeled off.

#### 2.1.4 Properties of PDMS

PDMS is nonirritating to the skin with no adverse effect on rabbits and mice, and has an only mild inflammatory reaction when implanted [116, 117]. The basic material properties of PDMS are presented in Table 2.1:

**Table 2.1 Basic material properties of PDMS.**

Properties	Value
Mass density	$\sim 0.97 \text{ kg.m}^{-3}$ [117]
Elastic Modulus	$0.35 - 3.7 \text{ MPa}$ [118]
Poisson Ratio	0.499 [117]

The elastic modulus of PDMS could be affected by the mixing ratio, curing temperature, and heating duration.

To describe the relationship between the elastic modulus of PDMS network and its base/agent ratio, an instrument setup for tension or compression test and cylindrical PDMS network samples should be provided. The density of the PDMS material is obtained by measuring the mass and volume of structures made of PDMS. According to the literature reviews [114, 118, 119], Table 2.2 shows the dependency of PDMS elastic modulus and mass density on the base/agent ratio.

**Table 2.2 The dependency of PDMS elastic modulus and mass density on the base/agent ratio [114, 118, 119].**

Base/Agent Ratio	$E \text{ (MPa)}$	$\rho \text{ (kg.m}^{-3}\text{)}$
PDMS 5:1	3.59	$9.52 \times 10^2$
PDMS 7.5:1	2.96	$9.18 \times 10^2$
PDMS 10:1	2.66	$9.20 \times 10^2$
PDMS 12.5:1	2.06	$9.52 \times 10^2$
PDMS 15:1	1.69	$9.87 \times 10^2$

The elastic modulus,  $E$ , in  $MPa$  can be expressed as a function of the PDMS base/curing agent weight ratio,  $n_p$ . A polynomial curve fitting with the goodness of fit ( $R$ -value) of 0.985 could be derived [114]:

$$E = 0.0044n_p^2 - 0.26896n_p + 4.7345 \quad (2.1)$$

According to the literature review [114, 116, 118–120], the following conclusions could be made:

- I. The larger the amount of the curing agent is, the larger the value of the elastic modulus.
- II. The higher the curing temperature, the larger the value of the elastic modulus.
- III. The longer the heating duration is, the larger the value of the elastic modulus.
- IV. The influence of heating duration on the elastic modulus of PDMS is mild.
- V. The elastic modulus of PDMS decreases more if the heating duration is longer.
- VI. The density of PDMS under various base/agent ratios does not have remarkable differences, as shown in Table 2.2 [121].

### 2.1.5 PDMS as a Nonlinear Hyperelastic Material

The PDMS is incompressible and has a linear stress-strain relation at low stress ( $< 150 \text{ kPa}$ ) but under high pressure, the nonlinear behavior should be considered [122]. According to the literature review, a hyperelastic constitutive second-order Ogden model is preferable for analyzing the large deformation of PDMS structures. The general form of the Ogden strain energy density function ( $W$ ) is given by [123]:

$$W = \sum_{i=1}^N \frac{\mu_i}{\alpha_i} [\lambda_1^{\alpha_i} + \lambda_2^{\alpha_i} + \lambda_3^{\alpha_i} - 3] \quad (2.2)$$

where  $\lambda_i$  is the principal stretching ratio, and  $N$ ,  $\mu_i$ , and  $\alpha_i$  are the Ogden parameters. The shear modulus results from  $2\mu = \sum_{i=1}^N \mu_i \alpha_i$ . The essential coefficients of the second-order Ogden model ( $N = 2$ ) and the bulk modulus of 15:1 mass ratio PDMS of Sylgard<sup>TM</sup> 184 are summarized in Table

2.3 from the literature [85, 124]. It should be noted that the bulk modulus increases with the amount of curing agent. The bulk modulus for 15:1 PDMS is 739 MPa [125].

**Table 2.3** Second-order Ogden material parameters for hyperelastic model (15:1 PDMS) [124].

$i$	$\mu_i$ (MPa)	$\alpha_i$
1	0.0001440	14.24
2	0.2674	2.743

## 2.2 PDMS Membrane Actuator

### 2.2.1 Working Principle of a Pneumatic Membrane Actuator

For an air-filled membrane actuator, the volume increase (resulting from the injection of the air into the inner channel surrounded by the PDMS) leads to the deflection profile of the circular clamped membrane. For thin plates where the thickness is small compared to the diameter, shearing stresses acting on normal sections of the plate are neglected and have a slight effect on the deflection of the plate. A circular plate rigidly fixed and there is no rotation or displacement at the edge [126, 127]. A horizontal circular plate firmly clamped in a horizontal direction as shown in Figure 2.1.

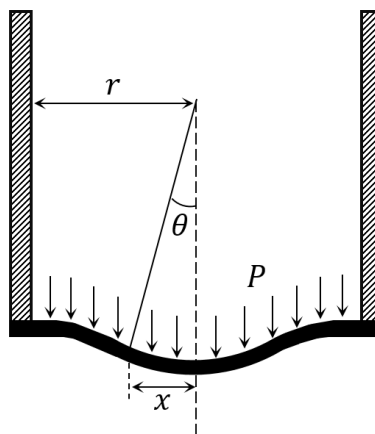


**Figure 2.1** 2D schematic view of a horizontal circular plate firmly clamped in a horizontal direction.

### 2.2.2 Theoretical Analysis of Membrane Actuator

The deflection in the proposed clamped circular plate could be obtained by the *Theory of Flexure of Plates*. For a circular plate clamped at its circumference and under uniform pressure on its face (Figure 2.1), the maximum deflection occurs at its center and could be obtained according to the following equation [126, 127]:

$$D_{max} = \frac{3(1 - \nu^2)Pa_p^4}{16Eh_p^3} \quad (2.3)$$

where  $\nu$  is the Poisson's ratio,  $P$  is the pressure,  $a_p$  is the radius of the plate,  $E$  is the elastic modulus,  $D$  is the deflection of the actuator, and  $h_p$  is the thickness of the plate.

The presented formula is given for the maximum deflection of clamped circular plates of an ideal, elastic material. In fixed-edged plates under uniformly distributed loads, the presented formula is correct for the thin and medium-thick plates ( $h_p/a_p < 0.1$ ). For thicker plates, because of the lack of ideal fixity at the edge and also the additional deflection in the thicker plates resulting from the shear stresses, the measured values of deflection are larger than those obtained by the presented formula for thin and also medium-thick plates. According to some experiments, researchers suggested that, for thicker circular plates, ( $h_p/a_p > 0.1$ ), with fixed edges under uniform loads, the values of deflection computed by the presented formula should be multiplied by a correction factor that depends on the ratio of the thickness  $h_p$  to the radius  $a_p$  of the plate.

This correction factor is:

$$C = 1 + 5.72 \left( \frac{h_p}{a_p} \right)^2 \quad (2.4)$$

Therefore, the modified version of the maximum deflection formula of the membrane actuator would be [127]:

$$D_{max}^{modified} = \left[ 1 + 5.72 \left( \frac{h_p}{a_p} \right)^2 \right] \frac{3(1 - \nu^2) P a_p^4}{16 E h_p^3} \quad (2.5)$$

where  $a_p$  is the radius of the plate,  $h_p$  the thickness of plate,  $P$  uniform load per unit area,  $E$  elastic modulus,  $D$  is the deflection of the actuator, and  $\nu$  Poisson's ratio.

### 2.2.3 Design of the Membrane Actuator

For the membrane actuator, a thin air channel with different lengths and diameters is embedded in a cylindrical PDMS structure. When the air channel is pressurized, according to the plate theory, the PDMS membrane on top of the actuator moves towards Z-axis. Figure 2.2 (a-c) shows a two-channel actuator which is made of two one-channel membrane actuator (Figure 2.2 (d)).

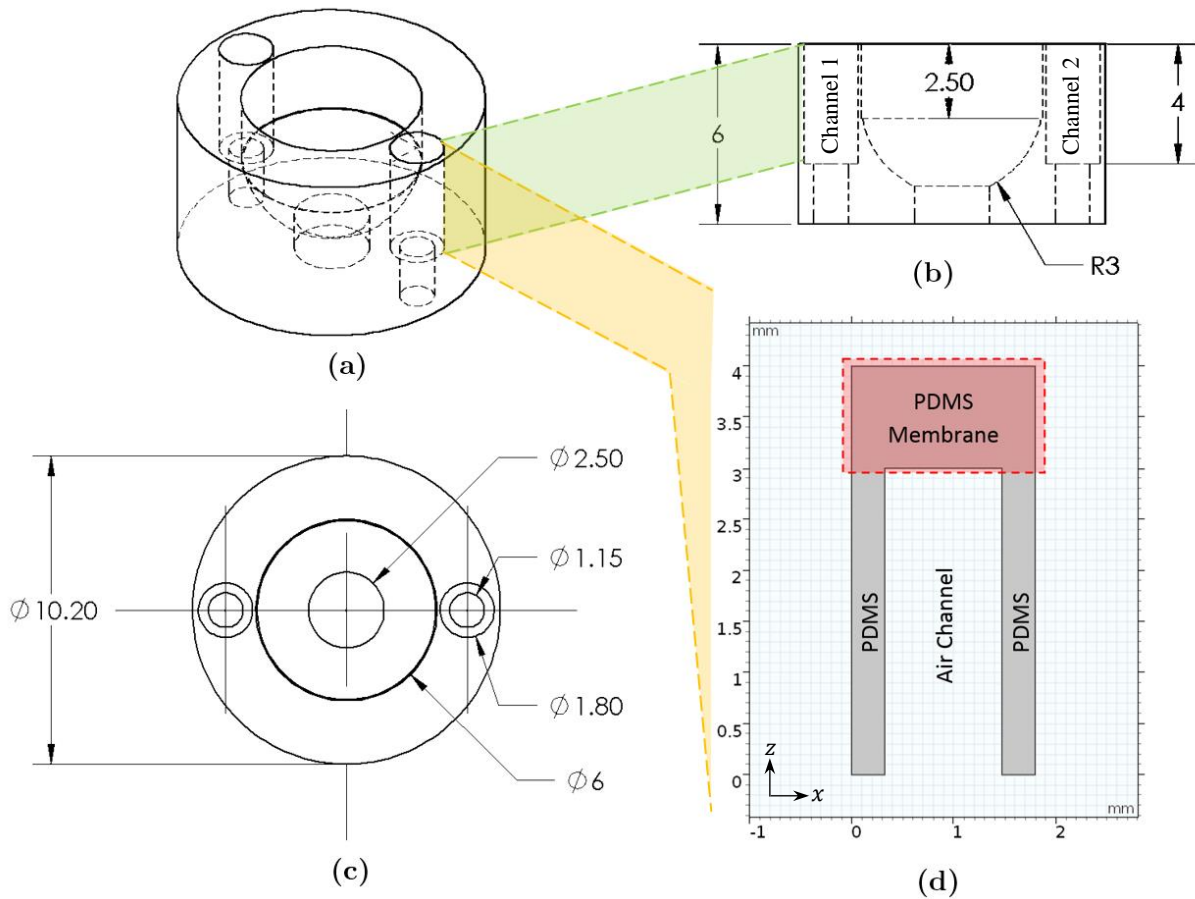


Figure 2.2 Modeling of the (a-c) two-channel and, (d) one-channel membrane actuator (All units are in mm).

Just like the balloon actuator, molds for the membrane actuator were 3D printed directly from computer-aided design (CAD) files (Figure 2.2). The small-scale and large-scale membrane actuators are shown in Figure 2.2 (b, c). Figure 2.2 (d) shows the two-channel membrane actuator.

For the small-scale two- and one-channel actuators, the length of the PDMS and mold cylinder are 4 mm and 5 mm, respectively. The inner diameter and length of the hole inside the PDMS cylinder are 1.15 mm and 3 mm, respectively. The outer diameter of the mold is 2.2 mm for the one-channel actuator. The size of the mold for the two-channel actuator is presented in Figure 2.2 (a-c). Different thicknesses for the PDMS membrane are used including 0.25, 0.45 and 0.75 mm.

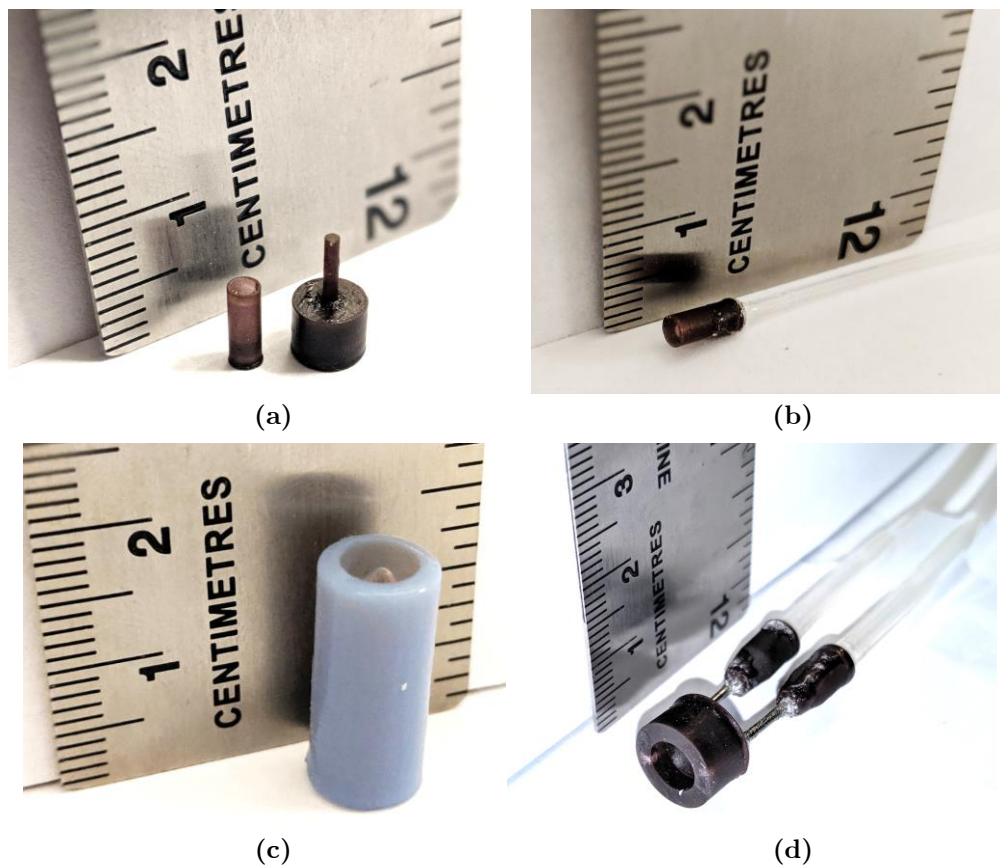


Figure 2.3 (a) 3D printed mold for one-channel small-scale membrane actuator, (b) The assembly of small-scale membrane actuator with PDMS and tubing, (c) The assembly of large-scale membrane actuator with PDMS, (d) The assembly of two-channel membrane actuator with all frames, connectors, and air tubing.

## Chapter 3: Experimental Setup and Methodology

### 3.1 Experimental Setup and Electronic System

An electronic control system was designed to operate and control the PDMS actuator. The control system is designed to be reconfigurable. The presented electronic system consists of the following components: an air pump, a solenoid valve, a proportional valve, a pressure sensor, a microcontroller, switches and MOSFETs, rotary potentiometers, power regulators, and a manual pressure regulator. The detailed explanations of each components are available in Appendix C. The air pressure in the control system is regulated by Pulse Width Modulation (PWM), which involves the controlled timing of the opening and closing of the valves. The board can be controlled manually by adjusting switches and potentiometers or automated via software running on the included Arduino microcontroller.

Two categories of experiments were performed:

- 1) Manual Basic Testing/Control
- 2) Advanced Testing/Control.

For basic testing of the actuator (the type of motion and inflation, leakage, etc.), it would be enough to operate the board manually by using the switches and the potentiometers to vary the pressure and open and close the valves. For advanced testing of the actuator, the Arduino IDE application could be used to write some codes that will automate the operation of the control board. Other environments such as Simulink to create the control or data acquisition software to run on the microcontroller can be used.

### 3.1.1 Manual Basic Control

#### 3.1.1.1 Selection of Components for Manual Basic Control Circuit

The following items were used to design the control circuit: an air compressor, a water filter (Husky HAD704), control valves (SMC VQ110U-5M and SMC PVQ13-5M-04-M5-A), a pressure sensor (ASDX-AVX-100PG-AA5), power MOSFETs (Four Opto-Isolated Power FET Switches (IRF540 type)), and an Arduino Mega 2560 microcontroller. More information for each component and the proportional valve characterization (SMC PVQ13-5M-04-M5-A) are presented on Appendix C.

**Table 3.1 Key features of Arduino ATmega 2560<sup>1</sup>.**

Features	Desired Feature	ATmega2560	Compatibility
Operating Voltage	5 V	5 V	Satisfied
Digital I/O Pins	At least 4 PWM outputs	54 (of which 15 provide PWM output)	Satisfied
Analog Input Pins	At least 9	16	Satisfied
DC Current per I/O Pin	Up to 85 mA	20 mA	Not Satisfied <sup>2</sup>
DC Current for 3.3 V Pin	No specific limitation	50 mA	Satisfied

---

<sup>1</sup> More information at: <https://store.arduino.cc/usa/mega-2560-r3>

<sup>2</sup> We will use an advanced control circuit and a voltage-to-current convertor to satisfy this feature.

### 3.1.1.2 Assembling the Manual Basic Board

Any necessary wires were soldered to all the electronic components following the data sheets and the wiring diagram available in Figure 3.1. Zip ties, screws, washers, nuts, and spacers were used. Using appropriate tubing, the air ports between components was connected.

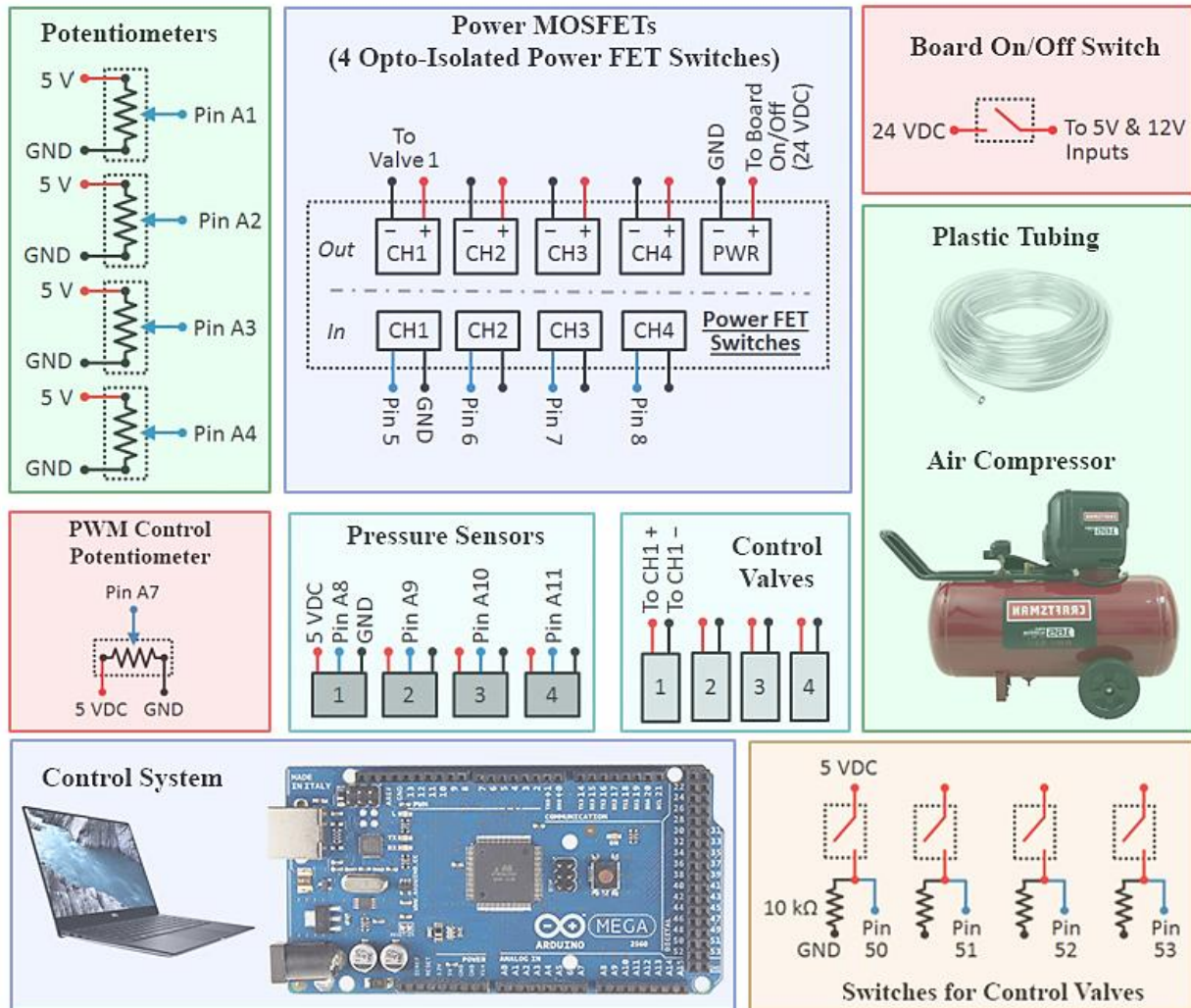


Figure 3.1 Wiring diagram of the manual basic board.

### **3.1.1.3 Guideline for Manual Basic Testing/Control**

Once the circuit has been built, we can start using it to control the pneumatic actuator. By powering the board by plugging in the 24  $V_{DC}$  power adapter and pressing the "Board On/Off" button, the power regulator turns on and displays output of 5  $V$ . If slowly turn one of the four potentiometer dials that control the valves, the solenoid valves should start actuating. Turning the dial of the potentiometer results in the variation of duty cycle (the ratio of the valve's on time to its off time).

During the actuation of the valve, if we adjust the potentiometer on the breadboard (the one connected to Arduino pin A7), the frequency at which the valve actuates should change. If the pump is on, adjusting the various potentiometer dials leads to different air pressure. The pressure readings for each output (in PSI) should be displayed and continuously updated via the serial monitor window of the Arduino IDE application.

## **3.1.2 Advanced Control**

### **3.1.2.1 Selection of Components for Advanced Control Board**

The list of items that were used for this section is almost as same as the manual control with the following modifications:

- I. The 2N2222A model that is an NPN bipolar junction transistor (BJT) is used. For low-power amplifying or switching applications, low to medium current, and medium voltage, this type of transistor would be appropriate and can operate at moderately high speeds.
- II. LM741 Operational Amplifier: this op-amp produces an output potential (relative to circuit ground) that is typically hundreds of thousands of times larger than the potential difference between its input terminals.

### 3.1.2.2 Assembling the Advanced Control Circuit

The Arduino board provides a PWM voltage signal, but the valve must be controlled by the current. Therefore, an intermediate circuit should be designed to convert PWM voltage to current so that each PWM voltage signal corresponds to a specific current signal. For this purpose, a two-step electric board should be designed: 1) the PWM voltage signal should be converted to a DC voltage (first step), and then 2) the DC voltage could be converted to its corresponding current signal (second step). The above-mentioned circuit has two major sections as follows:

The first component is an Active Low Pass Filter. The simplest form of a low pass active filter is to connect an amplifier to the basic RC low pass filter circuit as shown in Figure 3.2. It provides a low-frequency path to the input of a non-inverting operational amplifier. The high input impedance of op-amps prevents excessive loading on the output of the filter. On the other hand, the op-amps low output impedance prevents the filters cut-off frequency point from being affected by changes in the impedance of the load.

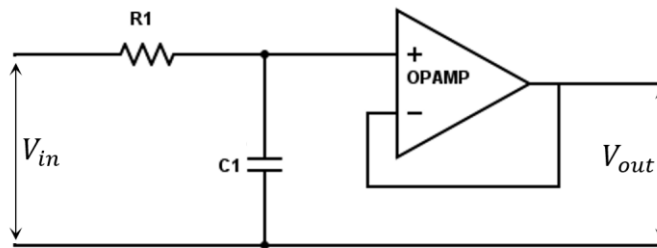
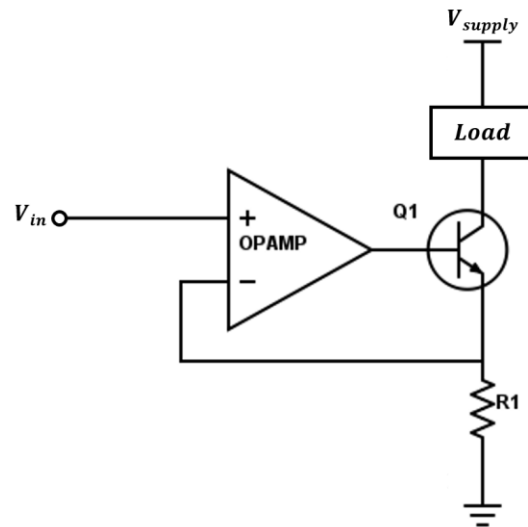


Figure 3.2 Active low pass filter.

The second component is an operational amplifier that maintains a constant current through the load as shown in Figure 3.3.



**Figure 3.3 Precision voltage to current converter.**

Op-amps could improve the function of discrete-component circuits. Also, the very high forward gain and differential input nature of the operational amplifier can be used to create a nearly ideal voltage controlled current source or V-to-I converter. According Figure 3.3, the high open loop gain of the amplifier will force the Gate of transistor  $Q1$  to the required voltage such that  $V_{in}$  appears across  $R_1$ . The input voltage to be converted is applied to the non-inverting input terminal of the op amp. The inverting input terminal is connected in feedback to one end of the resistor  $R_1$  and the source of transistor  $Q1$ . The output of the op-amp drives the Gate of the transistor. The current in  $R_1$  will thus be  $V_{in}/R_1$  and will flow only in the Source of  $Q1$ . It should be noted that the load current only if the transistor's base current is zero, would be  $V_{in}/R_1$ . The wiring diagram and the assembled advanced control board are presented in Figure 3.4. The schematic wiring diagram and the voltage-to-current convertor with more details are available on Appendix A.

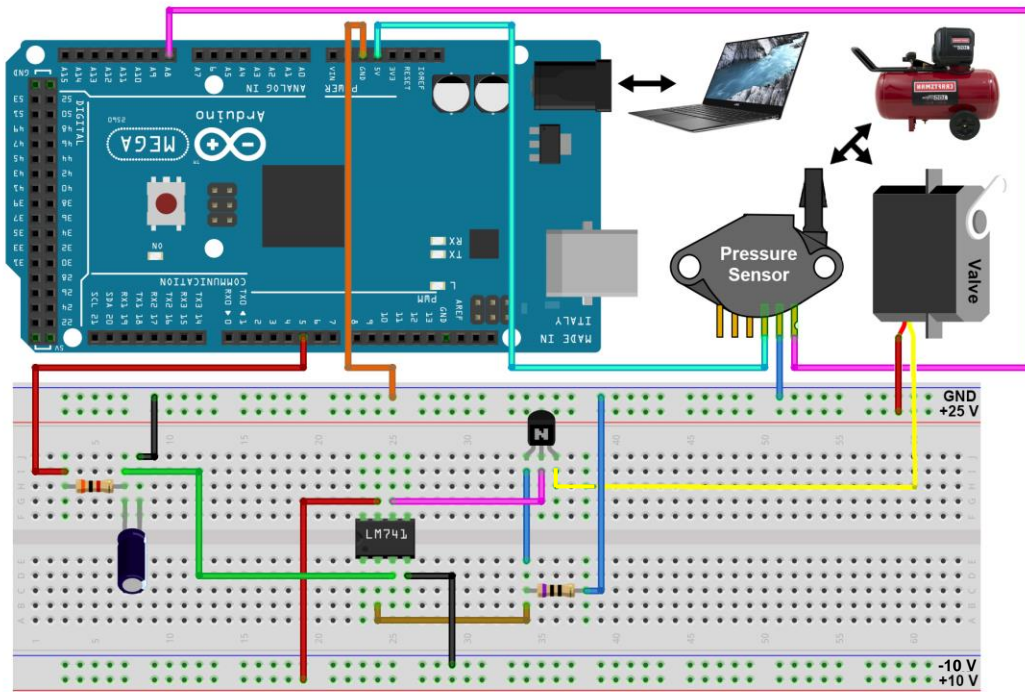


Figure 3.4 Wiring diagram and the assembled voltage to current converter board.

### 3.1.2.3 Guideline for Advanced Testing/Control

The Arduino integrated development environment (IDE) is a cross-platform application that is written in the programming language, Java. It is used to write and upload programs to Arduino compatible boards. A code was developed in the Arduino environment to automatically control the system. These are the most important items that should be considered in the code:

- I. Initialize values for the PWM duty cycle set by potentiometers,
- II. Define Setpoint, Input and Output for the system and PID controller,
- III. Define PID parameters ( $K_p$ ,  $K_i$ , and  $K_d$ ),
- IV. Develop PID controller or use libraries,
- V. Read the value of the sensor. Analog output is from 0 to 1024. Map it to a value from 0 to 255,
- VI. Update PWM output based on the above values from potentiometers,

- VII. Include transfer function for sensor Honeywell ASDX-RRX-100PG-AA5 (A-calibration),
- VIII. Read output voltages from sensors and convert to pressure reading in *psi/kPa*,
- IX. Write the output as calculated by the PID function.

### 3.2 System Calibration

#### 3.2.1 Optical Setup

As shown in Figure 3.5, the light emitted from the laser passes through a quadrilateral prism (QP). A portion of the light is projected directly along the incident direction, and the portion of the light can enter the environment directly or be absorbed by the black body. Another portion of the light is reflected at 90 degrees, which is controlled by a pinhole to reduce the size of the spot and to reduce background noise. Light passing through the pinhole enters the fiber through a collimator, and a flat mirror is placed at one end of the fiber end face. The plane mirror returns the reflected light path back through the QP. The light passing through the QP will be at 90 degrees to the light incident in the direction of the laser. A photodetector is placed in the 90 degree direction, and the amount of reflected light energy is measured by a photodetector.

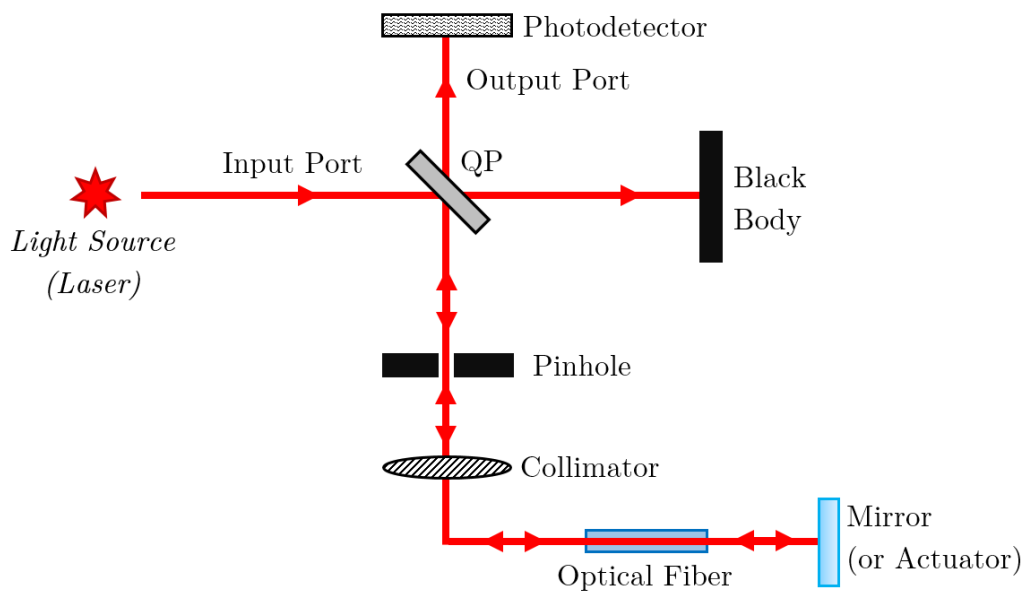


Figure 3.5 Optical setup for system calibration.

We used one optical fiber to determine the deflection of the actuator as a function of air pressure. Therefore, a two-step experiment is needed: First, the relationship of the displacement and the detector voltage would be obtained. Then, under the same experimental condition, the relationship of the air pressure (which leads to the displacement of the actuator) and the detector voltage would be observed. By combining the results of these two steps, the displacement of the actuator could be determined as a function of the air pressure.

### 3.2.2 Methodology for System Calibration

To use fiber and lens for measuring the displacement, two steps should be followed: obtaining 1) Displacement–Voltage, and 2) Pressure–Voltage graphs. First, the relation between the displacement and the voltage (laser power) should be defined as shown in Figure 3.6.

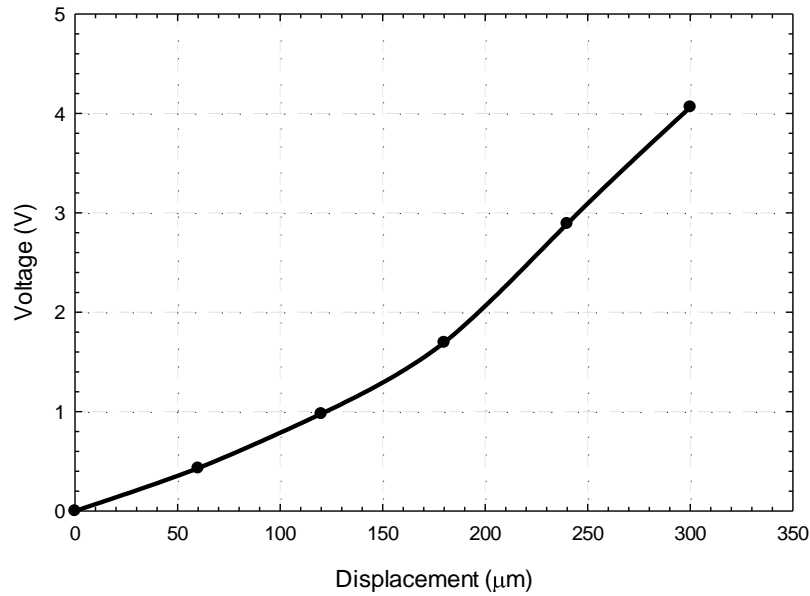


Figure 3.6 Displacement as a function of the laser power.

Using the curve fitting toolbox in Matlab®, the following function could be derived:

$$D = a_m V^3 + b_m V^2 + c_m V + d_m \quad (3.1)$$

where  $D$  is displacement in  $\mu\text{m}$ ,  $V$  is the voltage or laser power ( $V$ ),  $a_m = 4.213$ ,  $b_m = -37.47$ ,  $c_m = 156.5$ ,  $d_m = 0$  and the goodness of fit is  $R^2 = 0.999$ .

In the second step, for actuators with different thicknesses, the Pressure–Voltage graphs, as well as their corresponding curve fitting function, could be obtained as presented in Figure 3.7:

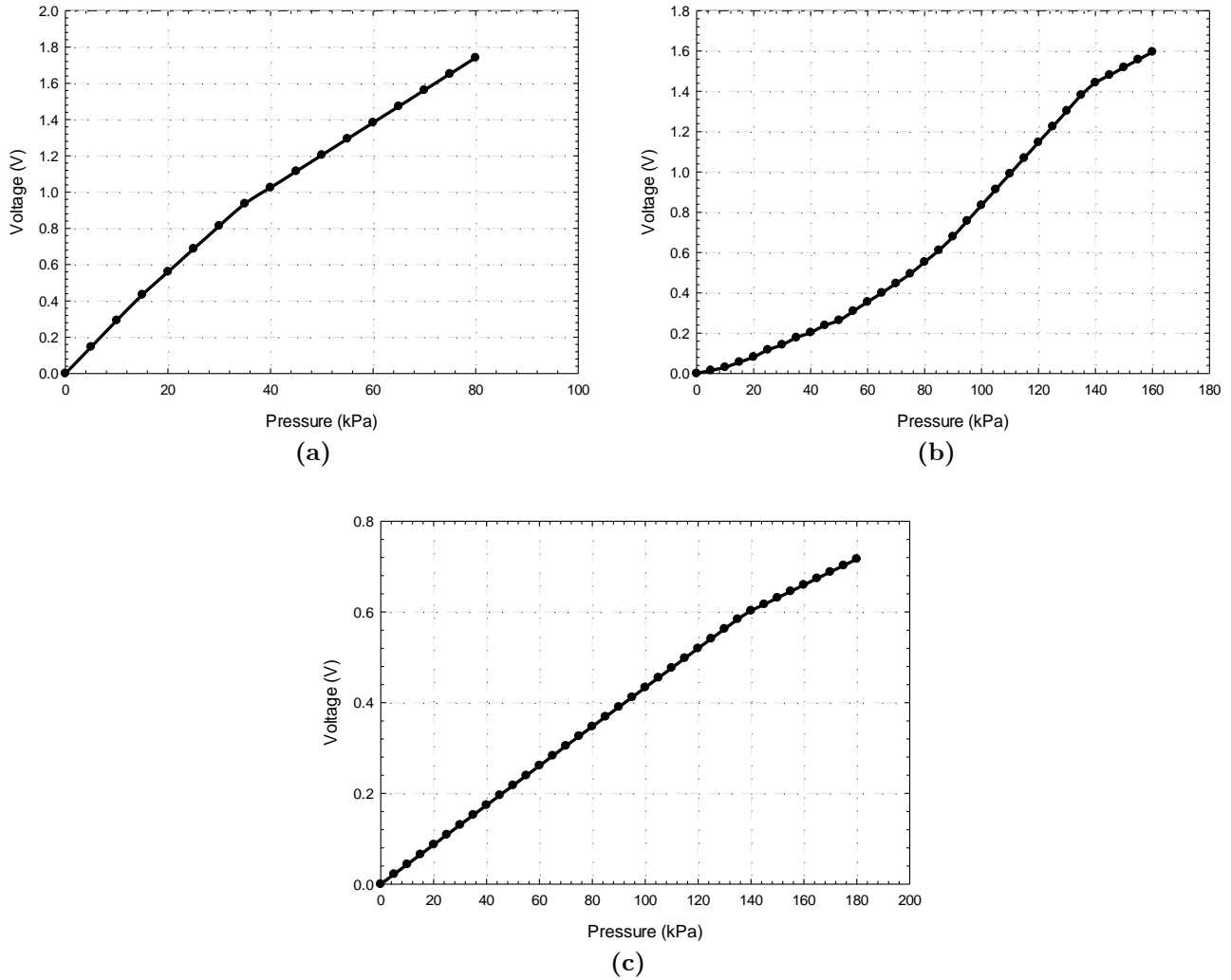


**Figure 3.7** Pressure as a function of the voltage for different PDMS membrane thicknesses:

(a) 0.25 mm, (b) 0.45 mm, and (c) 0.75 mm.

The curve fittings are as follows for each thickness:

0.25 mm	$V = eP^2 + fP + g \quad (3.2)$ <p>where <math>e = -7.377 \times 10^{-5}</math>, <math>f = 0.02122</math>, <math>g = 0</math> and the goodness of fit is <math>R^2 = 0.999</math>.</p>
0.45 mm	$V = eP^2 + fP + g \quad (3.3)$ <p>where <math>e = 4.768 \times 10^{-5}</math>, <math>f = 0.003239</math>, <math>g = 0</math> and the goodness of fit is <math>R^2 = 0.989</math>.</p>
0.75 mm	$V = eP^2 + fP + g \quad (3.4)$ <p>where <math>e = -2.58 \times 10^{-6}</math>, <math>f = 0.003721</math>, <math>g = 0</math> and the goodness of fit is <math>R^2 = 0.999</math>.</p>

According to the Displacement–Voltage (D–V) and Voltage–Pressure (V–D) graphs for each actuator, the displacement as a function of pressure (Displacement–Pressure graph (D–P)) could be derived as follows:

$$D = a(eP^2 + fP)^3 + b(eP^2 + fP)^2 + c(eP^2 + fP) = hP^6 + iP^5 + jP^4 + kP^3 + lP^2 + mP \quad (3.5)$$

The six coefficients of the derived equation are listed in Table 3.2:

**Table 3.2 Coefficients of the displacement–pressure equation.**

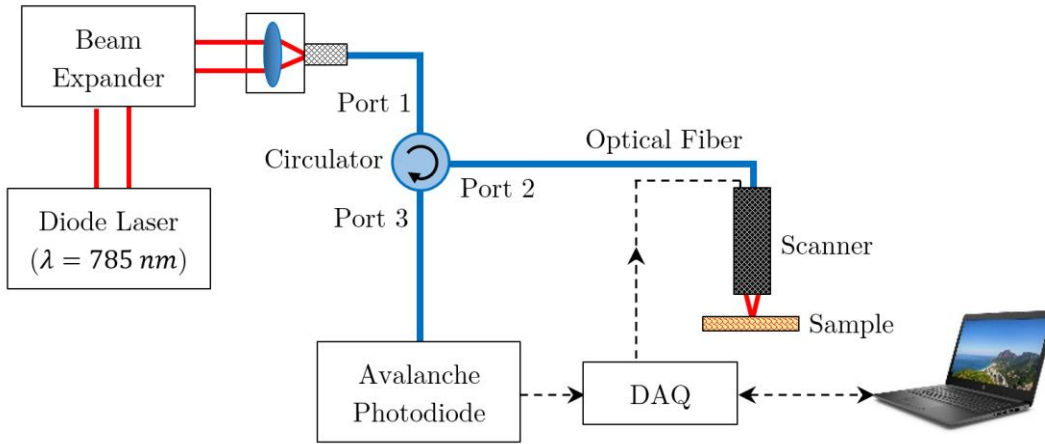
Coefficients	Thickness		
	0.25 mm	0.45 mm	0.75 mm
<i>h</i>	$-1.69134 \times 10^{-12}$	$4.57 \times 10^{-13}$	$-7.2 \times 10^{-17}$
<i>i</i>	$1.45955 \times 10^{-9}$	$9.31 \times 10^{-11}$	$3.13 \times 10^{-13}$
<i>j</i>	$-6.23752 \times 10^{-7}$	$-7.9 \times 10^{-8}$	$-7 \times 10^{-10}$
<i>k</i>	0.000157567	$-1.1 \times 10^{-5}$	$9.36 \times 10^{-7}$
<i>l</i>	-0.028417311	0.007069	-0.00092
<i>m</i>	3.32093	0.506904	0.582337

### 3.2.3 Laser Doppler Vibrometer (LDV)

An LDV can be utilized to make non-contact vibration measurements (velocity, displacement) of a surface. The LDV makes the vibration measurement without mass-loading the object of interest, which is especially important for MEMS instruments. An LDV (Polytec<sup>®</sup> OFV-5000) was used to measure the deflection of the PDMS balloon actuator. The output of the LDV is a continuous analog voltage. This voltage is directly proportional to the target velocity or displacement of the object of interest. We used a wide range of air pressure (0 – 110 *psi*) to check the deflection of the actuator. The principles of operation of LDV is explained on Appendix D.

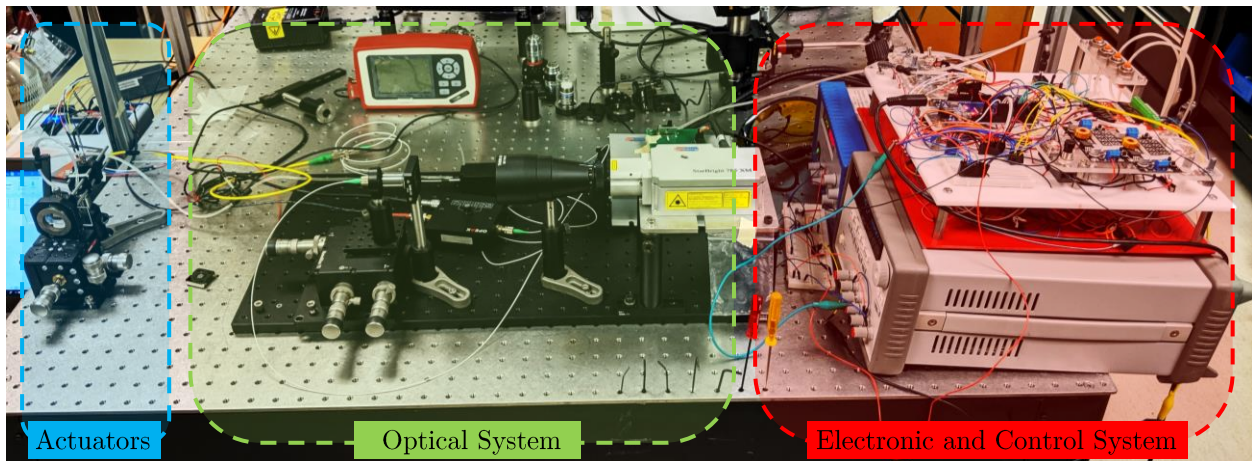
### 3.2.4 Optical Instrumentation and Resolution

Figure 3.8 shows the schematic of the optical system integration. The reflectance confocal microscopy was used in this study. A 785 *nm* diode laser (Starbright 785XM, Torsana Laser Technologies) with linearly polarized and 500 *mW* output power, the optical fiber, and the lenses inside the scanner form the illumination path. Also, a 3-port circulator (OF-LINK, PICIR-785-H7-L-10-FA) was used. The light emitted from the laser goes to port 1 of the circulator, and exits from port 2 to the scanners. The single scattered light (confocal imaging signal) by the tissue is collected by lenses in the scanner, and comes back through the same optical fiber (port 2) to port 3, where the light goes to the avalanche photodiode detector (OPEAK, PD-M-TBPIN-SW) for converting to electrical signals. As described in Chapter 1, the fiber acts as the pinhole in the confocal system and the circulator is like a beam splitter in the traditional confocal system. These electrical signals would be converted to image data and then transferred to the computer for image display and archiving. The MEMS actuator is controlled by the control electronics and the whole system operation is controlled and synchronized by the PC computer.



**Figure 3.8 Schematic diagram of the proposed imaging system.**

The experimental setup, which is the combination of the optical system, electronic and control system, and the actuators are presented in Figure 3.9.

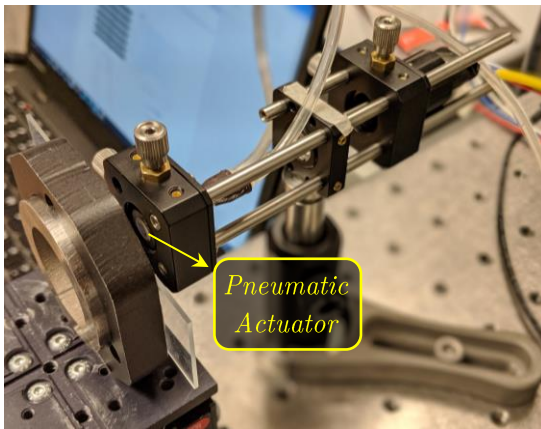


**Figure 3.9 Full assembly of the actuators, control and optical system.**

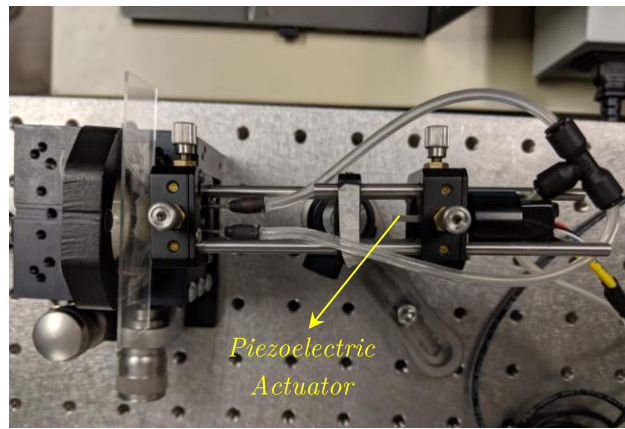
The actuators from Figure 3.9 are enlarged in Figure 3.10, and the full assembly of the probe including the membrane and piezoelectric actuators with the lenses are presented in Figure 3.10 (b, c). In our designed control system, according to the experiments, the air pressure resolution is  $0.83 \text{ kPa}$  and the designed two- and one-channel actuators show the axial resolution of  $1.12 \text{ }\mu\text{m}$ . The axial resolution of the confocal scanner could be derived as follows [128]:

$$R_{axial} = \sqrt{\left[ \frac{0.88 \lambda_{wl}}{n_{ri} - [n_{ri}^2 - NA^2]^{0.5}} \right]^2 + \left[ \frac{\sqrt{2} n_{ri} PH}{NA} \right]^2} \quad (3.6)$$

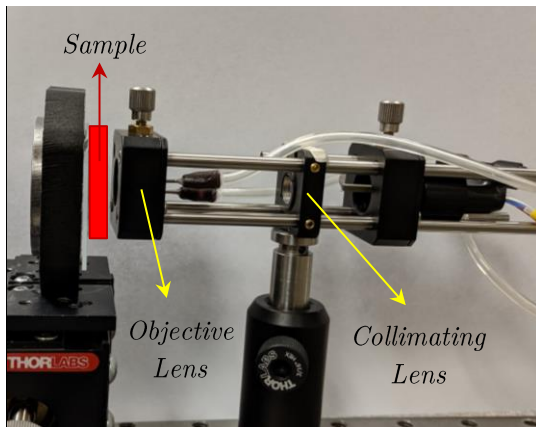
where  $\lambda_{wl}$  is the wavelength of the excitation light,  $n_{ri}$  is the refractive index of the medium,  $PH$  is the pinhole or core diameter of the optical fiber, and  $NA$  is the numerical aperture of the objective lens. In our system the  $NA$  is 0.55,  $n_{ri} = 1$  and  $\lambda_{wl} = 785 \text{ nm}$ . The fiber that was used is a single-mode optical fiber with core diameter of  $PH = 8.2 \mu\text{m}$ . Theoretical axial resolution of the scanner is  $21.5 \mu\text{m}$ .



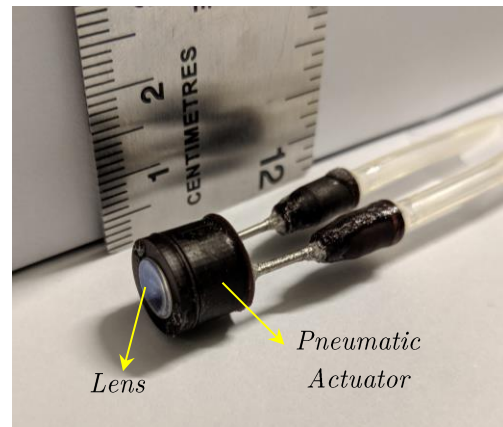
(a)



(b)



(c)



(d)

Figure 3.10 Assembly of the probe, actuators and lenses: (a) Pneumatic actuator, (b) Piezoelectric actuator, (c) Objective and collimating lens, (d) Assembly of the objective lens and pneumatic actuator

### 3.3 Control System

Many of the state-of-the-art MEMS-based scanners have no feedback control mechanisms. The scanner position, in real-time, needs to be characterized before the images are taken. The mechanical properties of the scanners can vary from device to device. Moreover, some uncertainties such as the driving force (pneumatic, magnetic, etc.) fluctuation have effects on the performance of the actuator. On the other hand, to obtain 3D images, the Z-direction position of the lens in the endoscope needs to be maintained to be constant during the scanning in X- and Y-direction. Therefore, these uncertainties have an undesirable effect on the quality of images. We propose to include a feedback control mechanism to accurately control the position of the MEMS actuator. The precise knowledge of the scanner position will be fed to image processing to improve the image quality.

#### 3.3.1 System Identification

System identification is a method of identifying or measuring the mathematical model of dynamic systems using measurements of the system's input and output signals. An approximation of a real system can be obtained by a mathematical model. Some entities including the complexity of a system, the limited prior knowledge of the system, and the incomplete availability of observed data prevent an accurate mathematical description of the system. On the other hand, in case of having full knowledge of the system, an exact description is not almost desirable because the model becomes too complicated and loses its practical application [129, 130].

Figure 3.11 shows the identification procedure for a system to obtain an appropriate mathematical model for the system. Three elements including the prior knowledge, objectives, and data are the main components in the system identification procedure and these entities are dependent. In other words, usually data is collected based on prior system knowledge. Also, modeling objectives leads to appropriate experimental design, and simultaneously observed data may also lead to an adjustment of the prior knowledge or even to the objectives. It should be noted that a criterion

function should be specified to measure the fit between observed data and model output signal. The system identification method has to be chosen. This method numerically solves the parameter estimation problem. Finally, a validation step should be considered to specify whether the proposed model is good enough for its intended use or not. If the model is not appropriate, the procedure must be repeated [129–131].

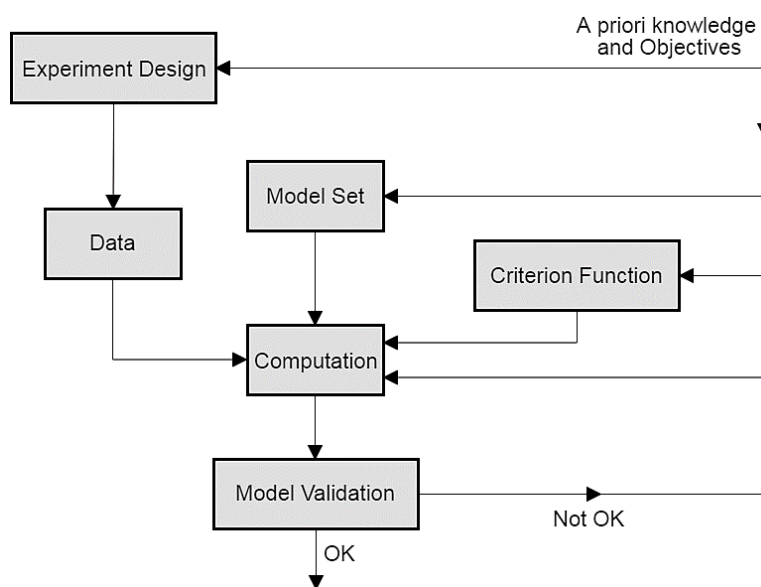


**Figure 3.11** The system identification loop [130, 132].

In this study, the *Direct Step Response Identification* method was used to identify the system. A step can be considered as an indefinite succession of contiguous, equal, short, rectangular pulses. The step input ( $u(t)$ ) could be specified on the form of:

$$f(t) = \begin{cases} 0, & t < 0 \\ k_s, & t \geq 0 \end{cases} \quad (3.7)$$

where  $k_s$  is a constant. In what follows, the issue of the system identification, in the context of PID tuning and control, is addressed. Various methodologies have been presented in the literature to estimate the parameters by performing a simple experiment on the plant. For different air pressures, the analysis of the step response was conducted. These analyses and also the dynamic

response consideration of this system (the *Impulse Response Identification* method Using Step Responses) reveal that the system is a first-order system [130].

It should be noted that controllability and observability are the main issues in the analysis of a system to observe whether it is possible to control or stabilize the system and decide what the best control strategy is to apply to the system. Controllability is the possibility of forcing the system into a particular state by applying a control signal. Observability is the possibility of reconstructing, through output measurements, the state of a system. Both controllability and observability matrixes were derived. The results show that the proposed system is both controllable and observable.

### **3.3.1.1 Linear Parameter Varying (LPV) systems**

In an open-loop control system, the control input is not affected by the actual (measured) outputs. However, in a closed-loop control system, the feedback is being applied to that system. Therefore, the control input is affected by the actual outputs, and the purpose of the controller will be to minimize the error between the actual output and the desired reference input value.

Initiated in [133], LPV modeling techniques have gained much interest. LPV systems are popular and provide a systematic means of computing gain-scheduled controllers. In LPV systems, a linear state-space model with the coefficient matrices functions of external scheduling variables is derived to define the system dynamics. These scheduling variables are assumed to be in some specific given range. Typically, the parameters vary slowly compared to the dynamics of the system and are not uncertain and can often be measured in real-time during system operation or can be measured by doing pre-processing experiments [133, 134]. Figure 3.12 shows a brief explanation of LPV, LTI and LTV systems.

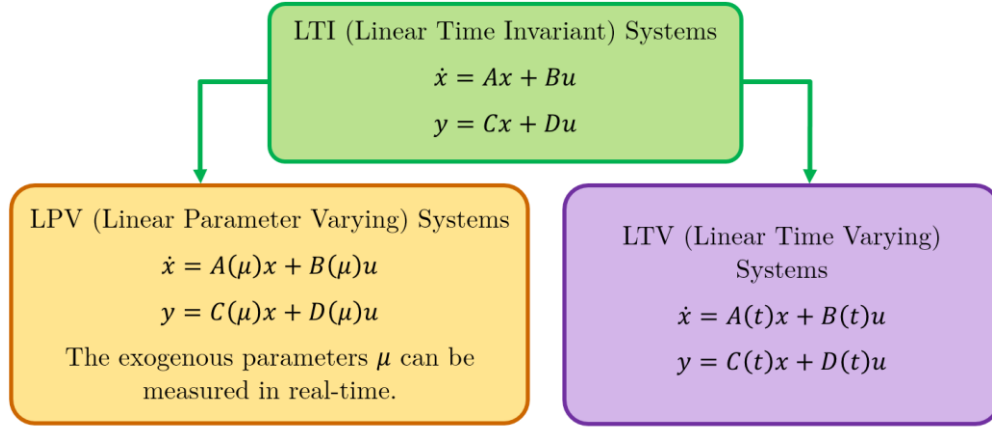


**Figure 3.12 LPV vs. LTI vs. LTV systems.**

### 3.3.1.2 LPV Model Structures

The mathematical model of a nonlinear system is usually formulated as a state space representation by a first-order differential equation in terms of the input  $u(t) \in \mathbb{R}^m$ , output  $y(t) \in \mathbb{R}^p$  and state signals  $x(t) \in \mathbb{R}^n$  and outer disturbances modeled through the signal  $w(t) \in \mathbb{R}^d$  and the initial condition of  $x(t_0) = x_0$ :

$$\begin{aligned} \dot{x} &= f(x, u, w), \\ y &= h(x, u, w), \end{aligned} \tag{3.8}$$

Parameter-dependent systems are linear systems, whose state-space descriptions are known functions of time-varying parameters. The aim of the LPV modeling procedure is finding an LPV description of the nonlinear model based on the form of:

$$\begin{aligned} \dot{x} &= A(\mu)x + B(\mu)u \simeq f(x, u), \quad \mu \in \Omega \\ y &= C(\mu)x + D(\mu)u \simeq h(x, u), \end{aligned} \tag{3.9}$$

where  $\mu$  is the possibly state dependent parameter vector varying within a region  $\Omega$ . The known relation  $\mu = \sigma(y, r_e)$  depends only on the measured signals  $y$  and external signal  $r_e$  whose values are known in the operational time of the system. Therefore, an LPV model is defined as a linear model whose state-space matrices depend on a vector  $\mu$  of time-varying parameters of the form:

$$\begin{aligned}\dot{x} &= A(\mu)x + B(\mu)u \\ y &= C(\mu)x + D(\mu)u\end{aligned}\tag{3.10}$$

Typically, the parameter dependency has an explicit structure including affine, polynomial, etc [129, 130, 134].

### 3.3.1.3 Linearization Through LPV Modeling

For nonlinear systems, the direct linearization schemes can be applied roughly categorized into the following types: global linearization, linearization about equilibrium, and linearization about a parametrized state trajectory [134]. In the following, the off-equilibrium approach is presented: The restriction to equilibrium-point modeling is one of the disadvantages of classical linearization-based scheduling. Utilizing the off-equilibrium linearization method, it is possible to provide linearization at every operating point of the original nonlinear system and the solutions may be pieced together. Considering the nonlinear system as follows:

$$\begin{aligned}\dot{x} &= f(x, u), \\ y &= h(x, u),\end{aligned}\tag{3.11}$$

the velocity linearization at a point  $(x_0, u_0)$ , parameterized by  $\mu$ , would be:

$$\begin{aligned}\dot{x} &= \zeta \\ \dot{\zeta} &= \partial f_{x|(x_0, u_0)} \zeta + \partial f_{u|(x_0, u_0)} \dot{u} \\ \dot{y} &= \partial h_{x|(x_0, u_0)} \zeta + \partial h_{u|(x_0, u_0)} \dot{u}\end{aligned}\tag{3.12}$$

The resulting linearization globally approximates the nonlinear model to an arbitrary degree of accuracy. It should be noted that this approach is not limited to equilibrium points because no restriction to equilibrium operating points is present. Interpolation of linear controller based on this method would be possible [134].

### 3.3.2 Feedback Control

Given a system, what it is desirable to be achieved is obtaining a desired response/output. This objective can be attained by an open- or closed-loop control system. Regarding the open-loop system, the controller specifies the input only on the basis of the reference signal. However, for a closed-loop system, the controller resolves the input signal by using the measurement of the output (the feedback signal). Feedback control is essential to keep the output close to the setpoint despite disturbances, noises, and variations of the process dynamics. The typical feedback control system is represented in Figure 3.13.

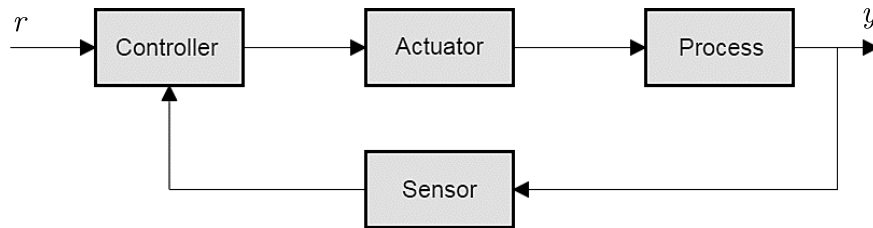


Figure 3.13 Typical components of a feedback control loop.

The performance of the overall control system depends on the proper selection of PID parameters. The actuator and sensor dynamics are often neglected from the purposes of controller design. The general schematic block diagram of a basic feedback control loop is shown in Figure 3.14:

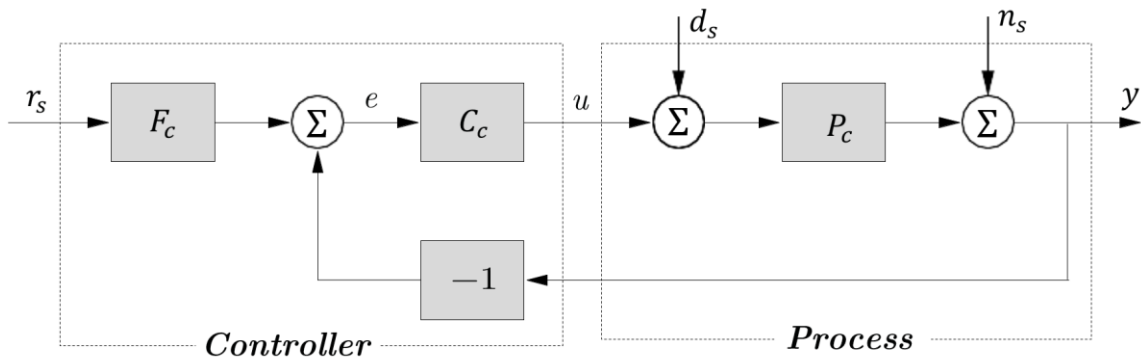


Figure 3.14 Block diagram of a basic feedback loop.

The system loop has two components: 1) the process ( $P_c$ ), and 2) the controller. The controller has two blocks including the feedback block ( $C_c$ ) and the feedforward block ( $F_c$ ). In the presented block diagram,  $r_s(t)$  is the reference signal,  $y(t)$  is the measured/output signal, and  $e(t) = r_s(t) - y(t)$  is the control error. Also,  $u$  is the manipulated (control) variable and the process is influenced by this variable.

The process variable  $x$  is the real physical variable that should be controlled, but control is based on the measured signal  $y(t)$ , where the measurements are corrupted by measurement noise  $n_s$ . Therefore, two disturbances could be considered to act on the process including the load disturbance signal ( $d_s$ ) and the measurement noise signal ( $n_s$ ). The former represents disturbances that deviates the process from its desired behavior. The latter distorts the information about the process variable  $x$ .

As a general basic feedback loop, this process is a system with three inputs ( $u, d_s, n_s$ ) and one output ( $y(t)$ ). The controller is a system with two inputs ( $y(t), r_s(t)$ ) and one output ( $u$ ). The most important signals for control are  $x, y$ , and  $u$ . Considering the Laplace transforms of  $x, y, u, d_s, n_s, r_s$  as  $X_s, Y_s, U_s, D_s, N_s, R_s$ , respectively, for the above-mentioned three signals, the following relations could be obtained according to the block diagram in Figure 3.14:

$$\begin{aligned}
 X_s &= \frac{P_c}{1 + P_c C_c} D_s - \frac{P_c C_c}{1 + P_c C_c} N_s + \frac{P_c C_c F_c}{1 + P_c C_c} R_s \\
 Y_s &= \frac{P_c}{1 + P_c C_c} D_s + \frac{1}{1 + P_c C_c} N_s + \frac{P_c C_c F_c}{1 + P_c C_c} R_s \\
 U_s &= -\frac{P_c C_c}{1 + P_c C_c} D_s - \frac{C_c}{1 + P_c C_c} N_s + \frac{C_c F_c}{1 + P_c C_c} R_s
 \end{aligned} \tag{3.13}$$

According to the presented equations, it should be noted that all three relations are given by the following set of six transfer functions which we call the *Gang of Six* as 1)  $\frac{P_c C_c F_c}{1 + P_c C_c}$ , 2)  $\frac{C_c F_c}{1 + P_c C_c}$ , 3)  $\frac{P_c C_c}{1 + P_c C_c}$ , 4)  $\frac{C_c}{1 + P_c C_c}$ , 5)  $\frac{P_c}{1 + P_c C_c}$ , 6)  $\frac{1}{1 + P_c C_c}$ . The first and second transfer functions describe how the

system responds to set point changes. It should be noted that the remaining four transfer functions describe how the system reacts to load disturbance and the measurement noise. In the special case of  $F_c = 1$  (a system with pure error feedback), the system is completely characterized by four transfer functions (second and third columns), and all control actions are only based on feedback from the error. These transfer functions and their equivalent systems are 1)  $\frac{P_c C_c}{1 + P_c C_c}$ : The complementary sensitivity function, 2)  $\frac{P_c}{1 + P_c C_c}$ : The load disturbance (input) sensitivity function, 3)  $\frac{C_c}{1 + P_c C_c}$ : The noise (output) sensitivity function, and 4)  $\frac{1}{1 + P_c C_c}$ : The sensitivity function.

For simplification and to avoid overcomplicating the system, we avoid using feedforward control and the measurement noise signal ( $n_s$ ) is ignored. Thus, we will use the simple representation as shown in Figure 3.15:

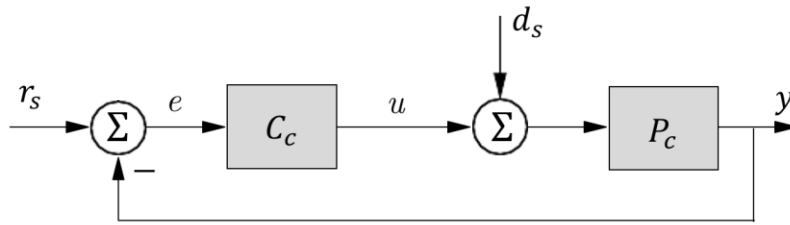


Figure 3.15 Simplified block diagram of a basic feedback loop.

The following relation could be obtained according to the block diagram in Figure 3.15:

$$Y_s = \frac{P_c}{1 + P_c C_c} D_s + \frac{P_c C_c}{1 + P_c C_c} R_s \quad (3.14)$$

### 3.3.2.1 PID Controller

A Proportional-Integral-Derivative (PID) controller is a three-term controller that has a long history in the automatic control field. Not only is it simple, but also in addition to its suitable performance, it could be classified as the standard practical controller in industrial applications [131, 135]. This controller could be used in industrial control applications, functioning to control the temperature, pressure, speed, etc. It uses a closed-loop control feedback mechanism to control process variables, and keep the actual output from a process as close to the setpoint output as possible. Regarding the growth of the research in the PID control field, some methods (basic algorithms) and strategies have been developed for increasing the performance and the ease of use of PID controller. Regarding the working principle of the PID controller, it continuously calculates an error value  $e(t)$  as the difference between a desired setpoint and a measured process variable, and applies a correction based on  $K_p$  for the proportional term,  $K_i$  for the integral term and  $K_d$  for the derivative term in the controller [136]. For the PID controller, many experiments and methods (manual tuning by trial and error method, the PID tuner of the Matlab®, Genetic Algorithms) were conducted to obtain the optimized PID parameters.

### 3.3.2.2 Genetic Algorithm

The use of Machine Learning (ML) is increasing rapidly in many applications. These highly flexible, adaptable methods are in several settings and show better performance, higher robustness and adaptability in comparison with traditional approaches. However, control systems are generally based on the same structure, building blocks and physics-based models of the dynamic system regardless of application. Given certain assumptions, traditional approaches could be mathematically analyzed with respect to stability, robustness, etc. However, ML methods are not subject to physic-based models results in lacking in terms of stability proofs and mathematical analysis. The types of ML algorithms depend on many factors, and their approach including the type of input and output data, and the type of task or problem that should be solved. A genetic

algorithm (GA) is a search algorithm used to find optimum solutions for a problem [137–139]. This method is for solving constrained and unconstrained optimization problems. This algorithm is based on natural selection that drives biological evolution. There are three main operations in a genetic algorithm including reproduction, crossover, and mutation. The sequences of operations involved in the GA are described in Figure 3.16 and are summarized as follows [140]:

1. Generate an initial, random population of individuals for a fixed size.
2. Evaluate their fitness to minimize integral square error.
3. Select the fittest members of the population.
4. Reproduce using a probabilistic method. (Selection rules select the individuals, called parents that contribute to the population at the next generation.)
5. Implement crossover operation on the reproduced chromosomes. Crossover rules combine two parents to form children for the next generation.
6. Mutation rules apply random changes to individual parents to form children.
7. Stop if the search goal is achieved. Otherwise, continue with Step 2.

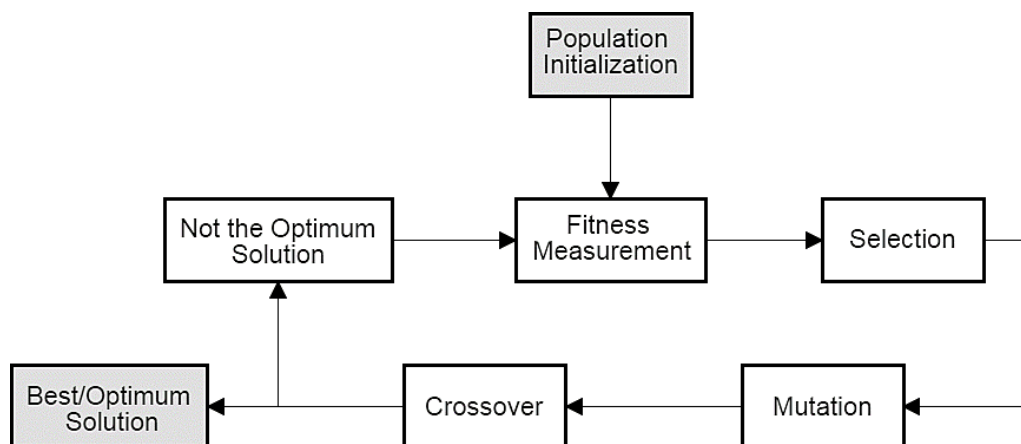


**Figure 3.16** Flow diagram of a genetic algorithm

Fitness is a measure to evaluate the suitability of a chromosome. Therefore, as in natural evolution, a fit chromosome with higher fitness has a higher probability of being selected for reproduction and contributing to one or more offspring in the next generation. The fitness value of each chromosome would be assessed in the reproduction phase. Reproduction helps the search of GA to find the best individuals. Crossover operation is performed to swap certain parts of the two selected chromosomes. Therefore, a good part of the old chromosomes would be captured and a better new one would be generated. A crossover probability of 100% means that each generation would be produced by entirely new offspring. Mutation operators are mostly used to provide more exploration. While crossover tries to converge the solution to a specific point, the mutation does its best to avoid convergence and explore more areas [139, 141].

### **3.3.2.3 Design of PID Controller Using Genetic Algorithm Technique**

This section studies the Genetic Algorithm (GA) method for optimizing PID parameters. PID is the most common type of controller because of its simplicity, and it yields stable results for most applications. To obtain good results, it is crucial to choose the appropriate and accurate parameters ( $K_p$ ,  $K_i$  and  $K_d$ ) but it is also somewhat difficult. GA is an optimization algorithm which is appropriate for finding optimized PID parameters.

Initially, GA generates a random population. The first and the most important step in GA is to encode the PID parameters into appropriate binary strings known as chromosomes, and then construct the population. The higher number of chromosomes leads to a better chance of finding the optimal result. Considering the execution time, some works recommend 20 to 100 chromosomes in one population. Then, each set of PID parameters would be passed to the PID controller. For each PID parameter values, the response of the system and its initial fitness value would be computed. This process will go through GA steps until the best fitness value is found [139, 141–144]. The details of GA parameters used in the simulation are shown in Table 4.4.

The PID tuning procedure through GA starts with the definition of the chromosome representation. According to Figure 3.17, each chromosome is formed by three values that correspond to the three gains of PID controller including  $K_p$ ,  $K_i$ , and  $K_d$ . By adjusting the PID gains, the minimization of the cost function is performed by the GA. This ensures that the actual output is as close as possible to the desired one.

$K_p$	$K_i$	$K_d$
-------	-------	-------

**Figure 3.17 Chromosome definition**

### 3.4 Image Quality

To prove the PID controller was successful in improving the quality of images, some image quality techniques could be used. With the rapid development of information technologies, digital imaging could be count as an important medium for obtaining information and communicating purposes. Image quality is a characteristic of an image and can refer to the combination of visually significant attributes of an image [145]. Generally, during the process of capturing, processing, compression, reproduction, storage and transmission, the images are subject to distortions. Examples of distortion are noise, blurring, and compression artifacts. This leads to some difficulties regarding the evaluation of images. In our proposed research, high quality medical images could help clinical applicants to detect the probability of cancer with more accuracy. Therefore, the study of image quality techniques has key practical significance [145–147].

#### 3.4.1 Image Quality Assessment (IQA) Techniques

Many researchers studied theories, sophisticated algorithms, and digital image processing techniques [145–151]. In order to control and enhance the quality of images, it is very important to quantify image quality degradations. For this purpose, the development of automatic image quality assessment systems is important. Therefore, the Image Quality Assessment (IQA) metrics

could play an important role in image quality adjustment, high quality medical imaging detection, Image quality could be assessed using two ways including objective and subjective evaluation. Objective methods are based on algorithms and computational models to predict perceptual image quality. The development of such algorithms has a lot of potential applications, for example, to monitor image quality in control quality systems. On the other hand, subjective methods are performed by humans and obtained by mean opinion score (MOS). Subjective method deals with the human eyes which extract structural information from the viewing field [147, 148, 151].

## **I. Subjective Methods**

In this method, to observe the quality of images, a number of people are asked to compare original images with distorted images. Then, to define an image quality index, mean opinion score (MOS) should be calculated according to people's comments. Three different factors including the viewing distance from observer to display, luminance, and display properties are considered in the subjective methods [146, 148–151].

## **II. Objective Methods**

Objective method is a quantitative approach. In this method, we evaluate the intensity, reference and distorted type of images to obtain a number which indicate the image quality. This number could be considered as the perceptual quality of image and somehow correlated with the human appreciation. According to the availability of reference image, this approach could be categorized as 1) full-reference (FR), 2) reduced-reference (RR), and 3) no-reference (NR) method. In FR methods, a reference sample should be available to determine the quality of the image. In RR objective reference IQA models, the original reference image is not completely available for IQA system, and some features of the reference image could be utilized by the IQA system. In NR method, there is no need for a reference image to determine the quality of an image, because the reference image without distortion is not available. Therefore, a no-reference image quality matrix

could be used for image quality evaluation. These NR algorithms are as follow [145, 146, 148–151]:

1) Natural Image Quality Evaluator (NIQE):

This algorithm is able to measure the quality of an image with arbitrary distortion. NIQE does not use subjective quality scores, and it is a completely blind image quality evaluator. This strategy only uses measurable deviations from statistical regularities. These are observed in natural images, and there is no training on human-rated distorted images. This algorithm is *opinion-unaware*, meaning that subjective quality scores are not involved with this method.

2) Blind/Referenceless Image Spatial Quality Evaluator (BRISQUE):

A database of images with known distortions should be used to train the BRISQUE IQA algorithm. This method is limited to evaluating the quality of images with the same type of distortion. BRISQUE is *opinion-aware* strategy, and subjective quality scores are used for the purpose of training images leading to a holistic measure of quality. This method uses scene statistics of locally normalized luminance coefficients. Therefore, regarding the presence of distortions, it would be possible to quantify possible losses of *naturalness* of the image. BRISQUE is a simple method which has low computational complexity. Its features could be used for distortion-identification, which would be suitable for real-time applications.

3) Perception based Image Quality Evaluator (PIQE):

This algorithm does not need a trained model. PIQE IQA is *opinion-unaware* and *unsupervised*, and is able to measure the quality of images with arbitrary distortion. For evaluating the image quality score, this model measures the local variance of perceptibly distorted blocks.

In most cases, PIQE performs similar to NIQE algorithm. After training the model, the NIQE and BRISQUE algorithms evaluate the image quality score with a good computational efficiency. Although PIQE algorithm is able to calculate the local measures of image quality in addition to

a global image quality score, its computational efficiency is less than NIQE and BRISQUE algorithms. It should be noted that, considering the agreement with a subjective human image quality score evaluation, all NR IQA metrics usually have better performance compared to FR IQA metrics [145, 146, 148–151].

In this thesis, we will use the no-reference (NR) method (objective model) including PIQE, NIQE, and BRISQUE algorithms to compare the quality of images with- and without PID controller.

## Chapter 4: Results and Discussion

### 4.1 System Identification Experimental Results

Table 4.1 shows the parameters of the first-order system for different air pressures. The general form of the first-order system is as follows:

$$G(s) = \frac{a_s}{b_s s + c_s} \quad (4.1)$$

**Table 4.1 Transfer function parameters of the first-order system for different air pressure.**

Air pressure (kPa)	$a_s$ (C( $\mu$ ))	$b_s$ (B( $\mu$ ))	$c_s$ (-A( $\mu$ ))	$c_s/a_s$	D( $\mu$ )
5	388.75	1	385.76	0.99	0
15	395.03	1	391.96	0.99	0
20	391.63	1	388.65	0.99	0
25	402.40	1	400.80	1.00	0
30	388.19	1	385.21	0.99	0
45	409.30	1	400.90	0.98	0
55	374.30	1	369.10	0.99	0
65	388.10	1	384.10	0.99	0
75	400.38	1	396.98	0.99	0
80	411.50	1	409.10	0.99	0
90	418.80	1	416.50	0.99	0
110	455.20	1	453.70	1.00	0
115	401.60	1	398.05	0.99	0
125	433.80	1	430.20	0.99	0
Average	404.21	1	400.79	0.99	0
Standard Deviation (SD)	20.15	0	20.66	0.004	0
Coefficient of Variation (%CV)	4.99	0	5.16	0.42	0

According to Table 4.1, the parameters  $A(\mu)$ ,  $B(\mu)$ ,  $C(\mu)$  and  $D(\mu)$  are a function of air pressure. The optimization method (System Identification in Matlab<sup>®</sup>) was used to obtain the transfer function of the open-loop system for different air pressures. According to Table 4.1, the parameter

$b_s = 1$  for all pressures and also the parameter  $a_s$  and  $c_s$  are too much close to each other as the ratio  $c_s/a_s$  represents. As an approximation and for simplicity, a new parameter,  $d_u$ , which is the average of parameters  $c_s$  and  $a_s$ , could be defined. The updated transfer function of the system is as follows with the parameters listed in Table 4.2:

$$G^*(s) = \frac{d_u}{s + d_u} \quad (4.2)$$

**Table 4.2 Updated transfer function parameters for different air pressure.**

Air pressure (kPa)	$d_u$
5	387.25
15	393.4933
20	390.14
25	401.60
30	386.70
45	405.10
55	371.70
65	386.10
75	398.68
80	410.30
90	417.65
110	454.45
115	399.83
125	432.00
Average	402.50
Standard Deviation (SD)	20.39
Coefficient of Variation (%CV)	5.06

As a non-linear system, different transfer functions for this system could be defined according to the previous table, but the deviation of parameter  $d_u$  from the average is so small (5%). Therefore, for simplicity, a unique (average) parameter for  $d_u$  could be considered for the proposed system. This creates a 5% error which is almost negligible (which is proved later in this thesis), and the effect of that on the PID controller will be proposed. The final transfer function of the system is:

$$G(s) = \frac{402.5}{s + 402.5} \quad (4.3)$$

#### 4.1.1 Closed Loop Controller Experimental and GA Results

Many experiments were conducted to obtain the optimized parameters of the PID controller. In addition to using manual tuning by trial and error method, the PID tuner of the Matlab® was used to find the PID parameters. For each test, the PID parameters for the general form of a PID controller in the Laplace domain are listed in Table 4.3:

$$C(s) = K_p + \frac{K_i}{s} + K_d s \quad (4.4)$$

**Table 4.3 PID parameters of the general form of a PID controller for different air pressure.**

Air pressure ( <i>kPa</i> )	$K_p$	$K_i$	$k_d$
5	0.178	77.55	0
15	0.178	69.65	0
20	0.177	71.53	0
25	0.177	71.09	0
30	0.177	69.92	0
45	0.176	59.04	0
55	0.176	64.81	0
65	0.177	67.73	0
75	0.177	60.26	0
80	0.177	72.41	0
90	0.177	73.74	0
110	0.177	80.52	0
115	0.175	71.17	0
125	0.176	75.97	0
Average	0.177	70.39	0
Standard Deviation (SD)	0.0007	5.81	0
Coefficient of Variation (%CV)	0.43	8.26	0

According to the experiments, a PI controller would be enough for this system. Also, as a non-linear system, different PID controllers with different PID parameters for each transfer functions could be defined, but the deviation of parameter  $K_p$  and  $K_i$  from the average is so small (%0.43 and %8, respectively). Therefore, for simplicity, a unique (average) parameter for  $K_p$  and  $K_i$  could be considered. This makes an error which is almost negligible as presented in what follows. The final PID controller for the system is as follows:

$$C(s) = 0.177 + \frac{70.39}{s} \quad (4.5)$$

The GA codes are presented in the Appendix E. We considered three main variables in cost function including the overshoot, rise time, and stability of the system. Our target is to prevent overshoot in the system, have a fast response system as obtained by trial and error tuning method, and improved stable system. Three weights were considered for each variable ( $W_1, W_2, W_3$ ), respectively as listed in Table 4.4.

**Table 4.4 Parameters used in the genetic algorithm.**

Air pressure (kPa)	Maximum Iteration	Crossover Percentage	Mutation Percentage	Population	$W_1$	$W_2$	$W_3$
5	1000	0.7	0.2	250	100	5	1
15	1000	0.7	0.2	250	100	5	1
20	1000	0.7	0.2	250	200	5	1
25	1000	0.7	0.2	250	100	5	1
30	1000	0.7	0.2	250	100	5	1
45	1000	0.7	0.2	250	100	5	1
55	1000	0.7	0.2	200	100	5	1
65	1000	0.7	0.2	250	100	5	1
75	1000	0.7	0.2	250	100	5	1
80	1000	0.7	0.2	250	100	5	1
90	1000	0.7	0.2	250	200	5	1
110	1000	0.7	0.2	250	200	5	1
115	1000	0.7	0.2	250	100	5	1
125	1000	0.7	0.2	250	100	5	1

The PID parameters according to the genetic algorithm are listed in Table 4.5:

**Table 4.5 PID parameters obtained by genetic algorithm and other methods.**

Methodology	Genetic Algorithm			Other Methods (Matlab <sup>®</sup> , etc.)		
Air pressure ( <i>kPa</i> )	$K_p$	$K_i$	$k_d$	$K_p$	$K_i$	$k_d$
5	0.13	69.11	0	0.178	77.55	0
15	0.12	69.01	0	0.178	69.65	0
20	0.03	86.24	$6.10 \times 10^{-5}$	0.177	71.53	0
25	0.57	87.65	0	0.177	71.09	0
30	0.33	92.43	$7.01 \times 10^{-5}$	0.177	69.92	0
45	0.01	66.41	0	0.176	59.04	0
55	0.45	65.97	0	0.176	64.81	0
65	0.85	96.72	0	0.177	67.73	0
75	0.02	58.26	0	0.177	60.26	0
80	0.14	69.38	0	0.177	72.41	0
90	0.19	99.8	$3.61 \times 10^{-7}$	0.177	73.74	0
110	0.21	91.2	0	0.177	80.52	0
115	0.13	62.17	$2.20 \times 10^{-6}$	0.175	71.17	0
125	0.40	85.48	0	0.176	75.97	0
Average	0.25	78.55	$9.54 \times 10^{-6}$	0.177	70.39	0
Average error between the results of GA and other methods (Matlab <sup>®</sup> , etc.) is 15%.						

As presented in Table 4.5, the result of experiments demonstrates the authenticity of the results of GA to solve the problem of choosing without getting stuck in local minimums. This adds confidence that the algorithm works well. The  $K_d$  part of the PID parameter becomes either 0 or negligible after running the algorithm for a few generations. According to the both GA and experiments, a PI controller is enough for this system. As same as experimental results, for simplicity, an average parameter for  $K_p$  and  $K_i$  could be considered. According to Table 4.5, the average error between the results of GA and other methods is 15%. The average PID parameters are almost close to the ones obtained by experiments (trial and error method). Consequently, GA is successful in finding PID parameters and the results are in a good fit with the other method.

### 4.1.2 Effect of the Proposed PID Controller on the System

For two different pressures, the effect of the PID controller is shown in Figure 4.1 and Figure 4.2:

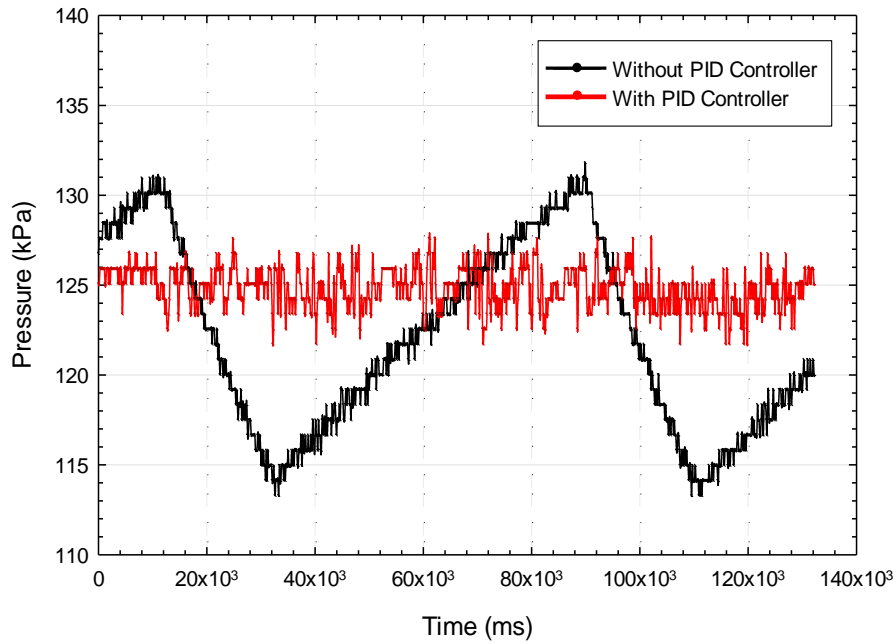


Figure 4.1 Effect of the proposed PID controller at high-pressure setpoint of  $P = 125$  kPa.

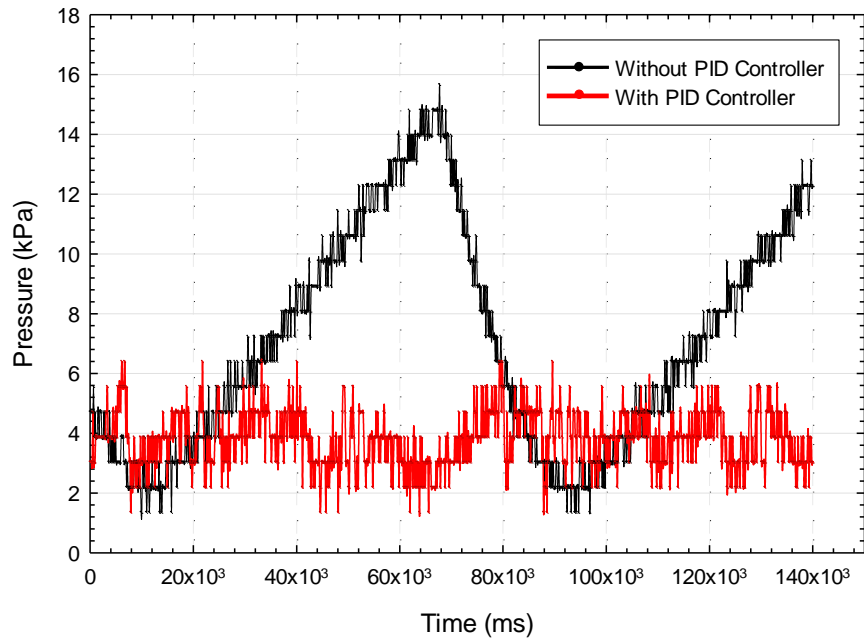
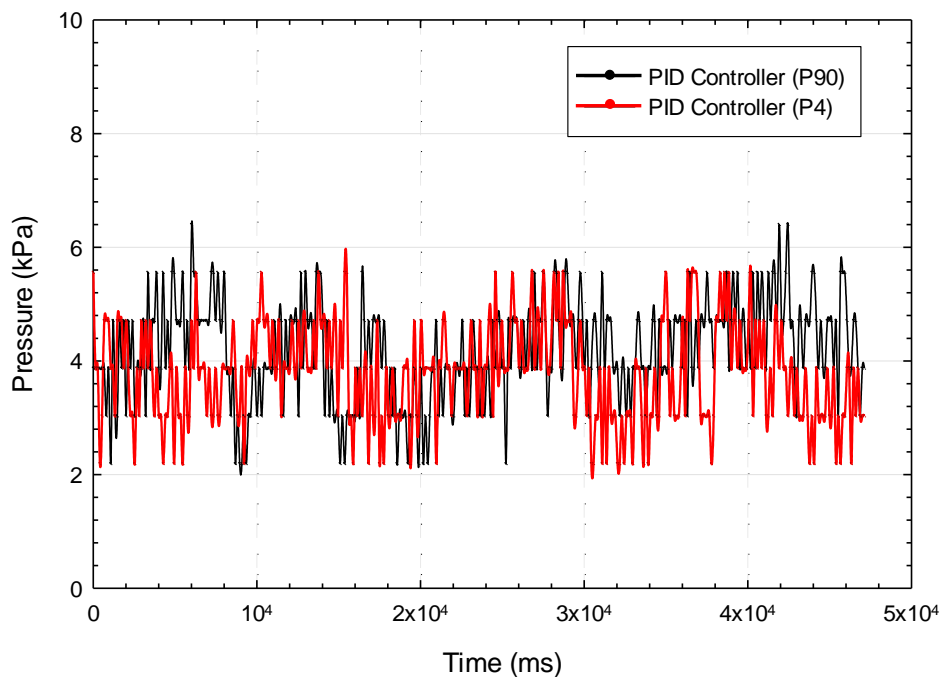
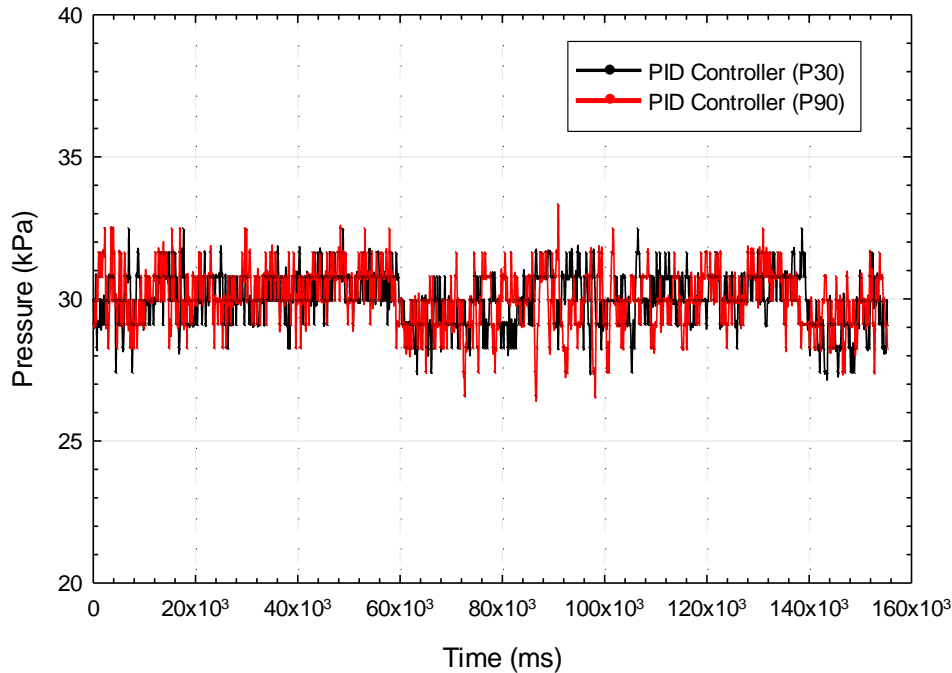


Figure 4.2 Effect of the proposed PID controller at low-pressure setpoint of  $P = 4$  kPa.

As shown in Figure 4.1 and Figure 4.2, the PID controller was successful in eliminating disturbances, and provides a stable position for the actuator. For the first case (Figure 4.1) at a high-pressure set point of  $125\text{ kPa}$ , the average pressure of  $P = 124.85\text{ kPa}$  and the standard deviation of  $1.13\text{ kPa}$  were recorded using the PID controller. Without the PID controller, the average pressure and the standard deviation would be  $P = 122.96\text{ kPa}$  and  $4.99\text{ kPa}$ , respectively. For the second case (Figure 4.2) at low pressure set point of  $4\text{ kPa}$ , the average pressure of  $P = 3.82\text{ kPa}$  and the standard deviation of  $0.98\text{ kPa}$  were recorded using the PID controller. Without the PID controller, the average pressure and the standard deviation would be  $P = 7.54\text{ kPa}$  and  $3.92\text{ kPa}$ , respectively. According to the experiments, the PID controller could improve the performance and position stability of the actuator by 94% for the offset error and 76% for the standard deviation. Some experiments were conducted to prove that using average PID controller parameters is reasonable. The results are shown in Figure 4.3 and Figure 4.4.



**Figure 4.3** Effect of using other random PID controller parameters ( $P = 90\text{ kPa}$ ) for a specific setpoint ( $P = 4\text{ kPa}$ ).



**Figure 4.4 Effect of using other random PID controller parameters ( $P = 90 \text{ kPa}$ ) for a specific setpoint ( $P = 30 \text{ kPa}$ ).**

For the first case (Figure 4.3), using the original set point PID parameters ( $P = 4 \text{ kPa}$ ) for controller leads to the average of  $P = 3.82 \text{ kPa}$  and the standard deviation of  $0.98 \text{ kPa}$ . On the other hand, for the previous set point, using the random alternative PID parameters ( $P = 90 \text{ kPa}$ ) for controller leads to the average of  $P = 4.03 \text{ kPa}$  and the standard deviation of  $1.08 \text{ kPa}$ . Regarding the second case (Figure 4.4), using the original set point PID parameters ( $P = 30 \text{ kPa}$ ) for controller leads to the average of  $P = 29.48 \text{ kPa}$ , and a standard deviation of  $0.93 \text{ kPa}$ . On the other hand, for the previous set point, using the random alternative PID parameters ( $P = 90 \text{ kPa}$ ) for controller leads to the average of  $P = 29.53 \text{ kPa}$  and the standard deviation of  $1.02 \text{ kPa}$ . This makes an error which is negligible. As shown in Figure 4.3 and Figure 4.4, because the proposed PID parameters for all air pressures are close enough to each other, for simplicity, using an average parameter for  $K_p$  and  $K_i$  is reasonable.

As shown in Figure 4.5 and Figure 4.6, for two different pressures, using the Pressure–Displacement correlations, the deflection of the PDMS membrane actuator was tracked to observe the effect of the PID controller on the system:

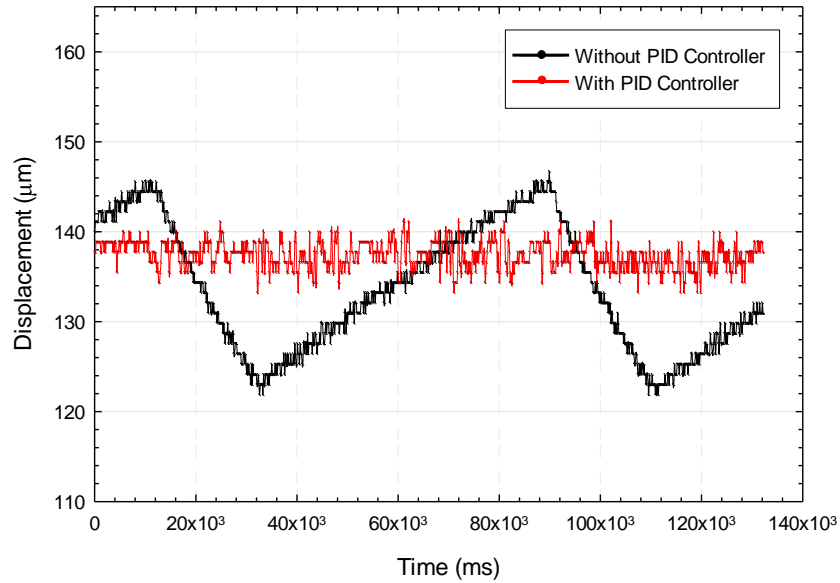


Figure 4.5 Tracking the displacement of the PDMS actuator and effect of the proposed PID controller at setpoint of  $P = 125 \text{ kPa}$ .

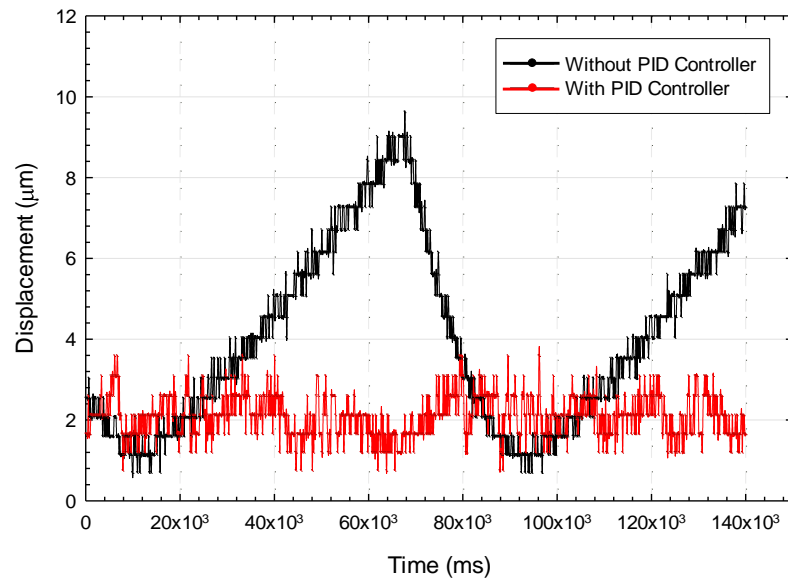


Figure 4.6 Tracking the displacement of the PDMS actuator and effect of the proposed PID controller at setpoint of  $P = 4 \text{ kPa}$ .

According to Figure 4.5 and Figure 4.6, the PID controller was successful in providing a stable position for the actuator. For the first case (Figure 4.5) at high-pressure setpoint of  $125 \text{ kPa}$  (or  $137.63 \mu\text{m}$ ), the average displacement of  $D = 137.42 \mu\text{m}$  and the standard deviation of  $1.51 \mu\text{m}$  were recorded using the PID controller. Without the PID controller, the average displacement and the standard deviation would be  $D = 134.78 \mu\text{m}$  and  $2.71 \mu\text{m}$ , respectively. In this case, with PID controller, the error is  $\%0.15$  and without PID controller, the error would be  $\%2.08$ .

For the second case (Figure 4.6) at a low pressure setpoint of  $4 \text{ kPa}$  (or  $2.14 \mu\text{m}$ ), the average displacement of  $D = 2.05 \mu\text{m}$  and the standard deviation of  $0.55 \mu\text{m}$  were recorded using the PID controller. Without the PID controller, the average displacement and the standard deviation would be  $D = 4.32 \mu\text{m}$  and  $2.42 \mu\text{m}$ , respectively. In this case, with PID controller, the error is  $\%4.21$  and without PID controller, the error would be  $\%101.88$ . The small vibrations in Figure 4.1 to Figure 4.6 are related to the resolution of the pressure sensor. This vibration leads to a very small deflection of the actuator which is negligible. The dynamic response consideration of the presented actuator is available on Appendix F.

## 4.2 Experimental, Analytical and Simulation Results

Using COMSOL<sup>®</sup> Multiphysics, a 2D model of the membrane actuator was investigated as shown in Figure 4.7. The Solid Mechanics Physics with the hyperelasticity properties of PDMS (PR 15:1) and Stationary Study were chosen for this analysis. For boundary conditions, all surfaces were fixed except surfaces A and B (Figure 4.7). The gravity was neglected in this simulation. The mesh sensitivity analysis was performed and the structure meshed with 11512 free quadratic elements.

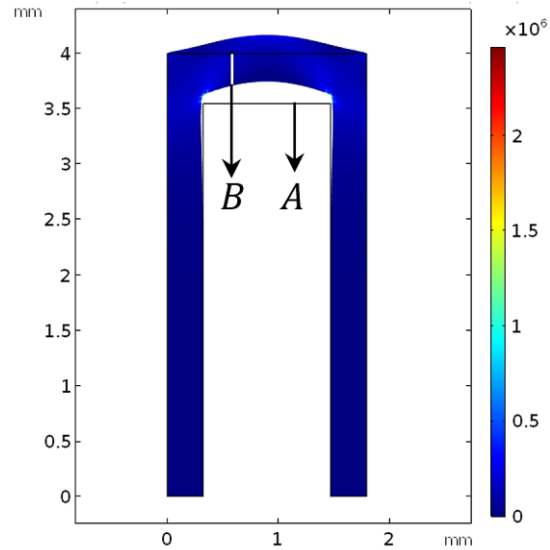


**Figure 4.7 2D model of the membrane actuator.**

The deflection of the small-scale actuator is very small and not visible to the naked eye. Therefore, to present a clearer image, we presented the deflection of the large-scale membrane actuator. Figure 4.8 shows the large-scale membrane actuator before and after actuation.

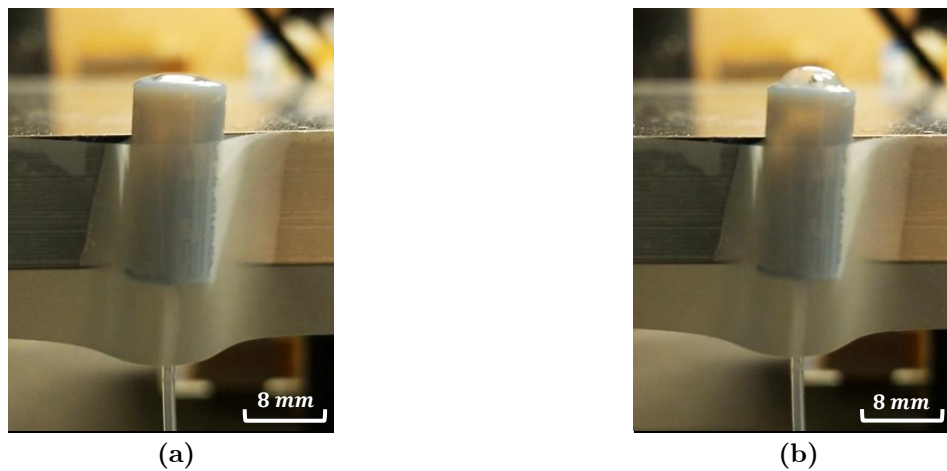


**Figure 4.8 The large-scale membrane actuator (a) before, and (b) after actuation.**

Different PDMS ratios (PR: 10, 15 and 20) were used to observe the effect of PR on the deflection of the PDMS actuator subjected to air pressure. Figure 4.9 shows that the higher the PR, the lower the elasticity modulus. This indicates that higher displacement could be achieved.

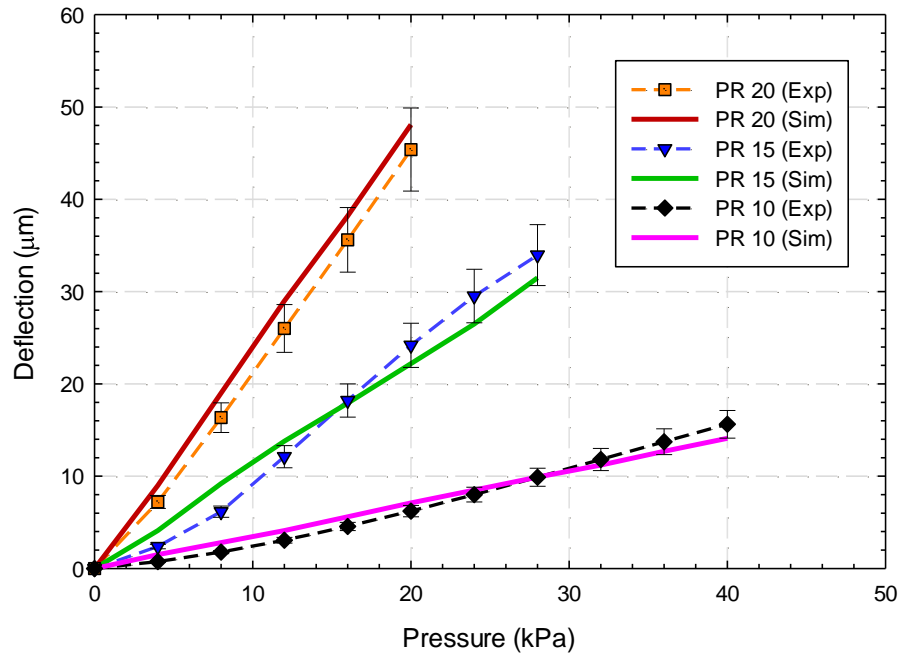


**Figure 4.9** Effect of the PDMS ratio (PR) on the deflection of the membrane actuator.

The results of the simulation and experiment have the same trend and show the RMSE of 0.115. The reason for this error is some assumptions for simplifying our modeling such as neglecting the effect the hyperelasticity of the PDMS. Considering Figure 4.9 and also the research papers, a PR ratio of 15:1 was used for fabrication of the membrane actuator.

For 0.45 mm PDMS membrane thickness, theoretical, experimental and simulation analysis were used to observe the behavior of the PDMS actuator subjected to air pressure. As Figure 4.10 shows, for lower air pressure, the results of the simulation for linear and hyperelastic (non-linear) modeling are in a good agreement. However, by increasing the air pressure, more deviation would be observed for the deflection estimation of the actuator. The theory analysis with involving the correction factor shows a good match with the result of LDV and fiber and lens experiments. However, a gap between the results of these methods is observable. Regarding the fiber and lens experiments, there is a distance between the end face of the optical fiber and the mirror, which is exponentially related to the laser energy reflected into the optical fiber by the plane mirror. The

initial value of the measurement was not zero. Approximate values are used in energy and distance calculations, which also results in incomplete matching between pressure and distance. Moreover, actuator instability can result in poor repeatability at different experimental stages.

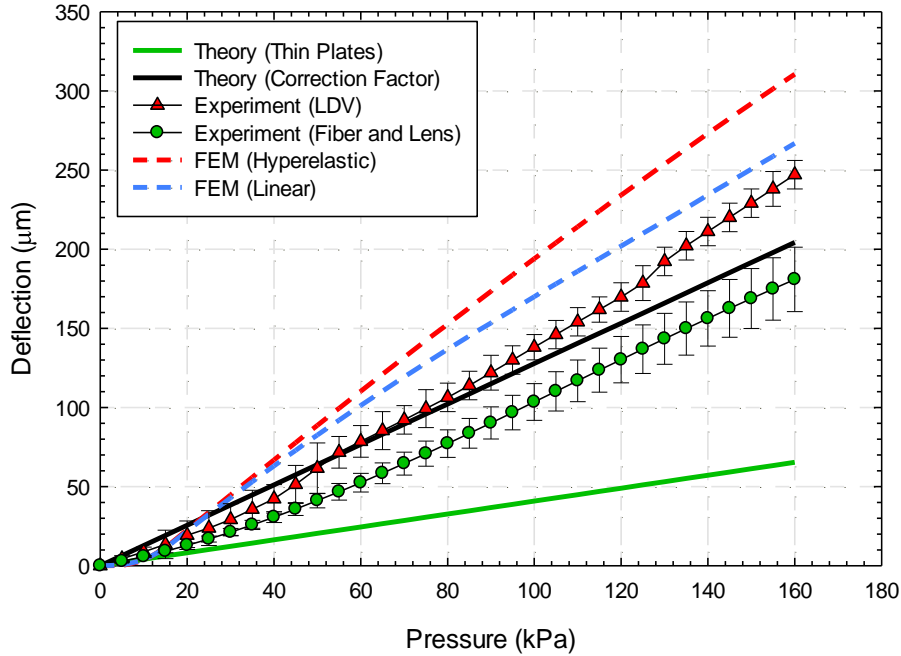


Figure 4.10 Experimental, theoretical, and simulation results for 0.45 *mm* thickness membrane actuator.

We used three thicknesses for the PDMS membrane to observe its dependency on the deflection of the actuator. The chosen thicknesses for the PDMS membrane actuator are 0.25 *mm*, 0.45 *mm*, and 0.75 *mm*. According to Figure 4.10, for the membrane actuator with 0.45 *mm* thickness, the results of the experimental (LDV and fiber and lens) methods are in a good fit with the theoretical method in low pressure range (<80 *kPa*). For higher air pressures, the actuator shows more non-linear behavior and actuator instability can result in poor repeatability at different experimental stages. Moreover, approximate values are observed in the laser energy reflected into the optical fiber and distance calculations, which results in incomplete matching between pressure and distance.

As Figure 4.11 shows, for 0.25 *mm* membrane thickness, the thin plate theory has a very large deviation compared to other methods. This is due to the simplicity of this analysis. As the experimental methods (LDV and Fiber and Lens) show, the membrane actuator shows a non-linear behavior, which the thin plate theory cannot predict. It should be noted that the theoretical method with the correction factor predicts the deflection of the actuator very well compare to the thin plate theory, but still has a fairly liner trend. For the 0.45 *mm* and 0.75 *mm* membrane thicknesses, there is a very large gap between the prediction of the thin plate theory and other methods. The bending properties of a plate depend greatly on its thickness. The approximate theories of thin plate become unreliable in the case of plates of large thickness and by increasing the thickness of the membrane, the thin plate theory cannot predict deflection accurately. Therefore, the thick-plate theory should be applied. This theory considers the problem of plates as a three-dimensional problem of elasticity and up to now, this analysis is fully solved only for a few particular cases. Therefore, including the correction factor on the thin-plate theory could compensate this error to some extent.

The responses of the PDMS actuator with two other different thicknesses are presented in Figure 4.11. For a specific air pressure, the thicker PDMS membrane shows a smaller deflection. The very thin actuator has a non-linear behavior compared to the two other actuators that make the process of controlling the actuator more difficult. According to Figure 4.10 and Figure 4.11, for 100  $\mu\text{m}$  deflection, the 0.45 *mm* PDMS membrane thickness actuator is the ideal case. Also, a more linear behavior compared to 0.25 *mm* thickness could be observed for this case. For taking images, we used 0.45 *mm* thickness.

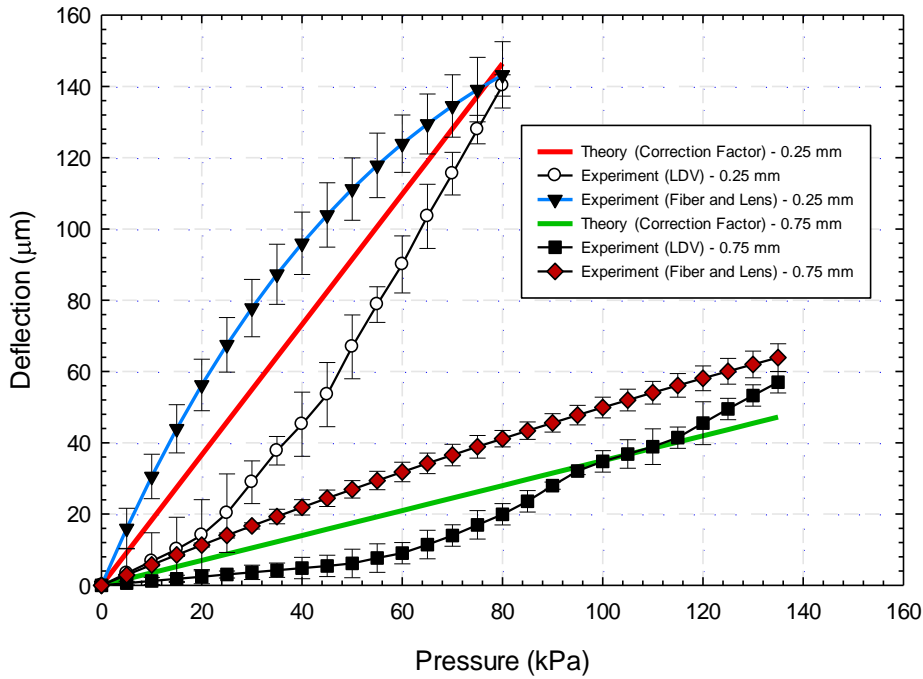
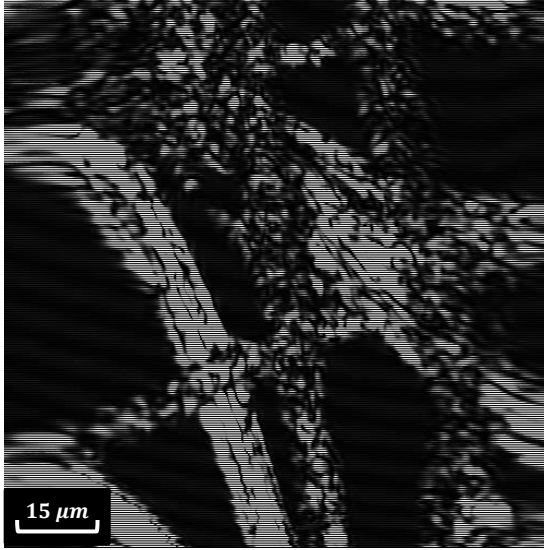


Figure 4.11 Comparison of membrane actuators with various membrane thickness.

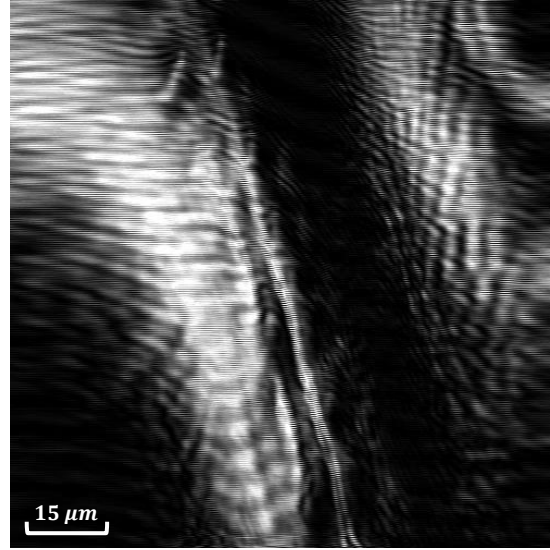
### 4.3 Imaging Results

#### 4.3.1 2D Images

To demonstrate the functionality of the proposed system, paper fiber and onion epidermis were used to obtain some images. The actuator was held stationary, and the samples were positioned in front of the objective lens of the MEMS scanner during experiments. Raster scanning of the laser beam has been performed by using another optical system developed by [152]. The collimating lens is Thorlabs C220TMD-B and the objective lens is Thorlabs C230TMD-B. The X-Y resolution of images is  $1.41 \mu\text{m}$  and the Field of View (FOV) is  $\sim 100 \mu\text{m} \times 100 \mu\text{m}$  [152]. The frame rate is 1.25 fps. After fixing the membrane actuator at a specific Z-depth, a paper fiber and onion epidermis were used for taking images in different air pressures. The results are shown in Figure 4.12.



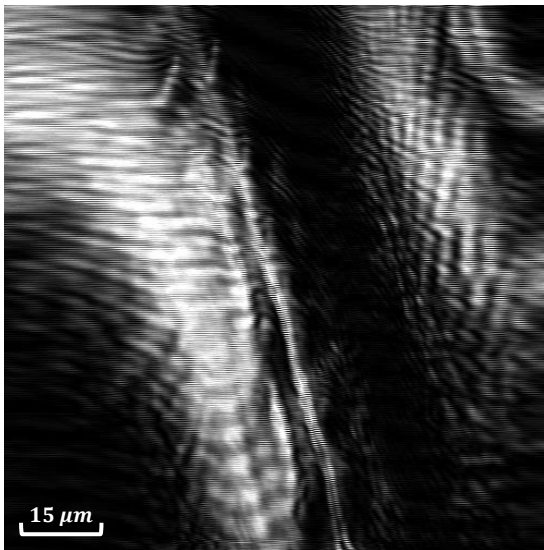
(a)



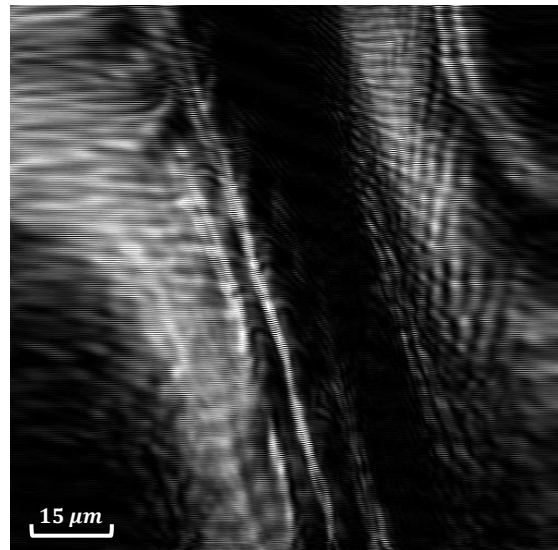
(b)

Figure 4.12 Confocal images of (a) paper fiber, and (b) onion epidermis at a specific fixed Z-depth and different air pressures.

The onions epidermis are used to compare the images that are taken without PID and with PID controller (Figure 4.13).



(a)



(b)

Figure 4.13 Confocal images of onion epidermis with (a), and (b) without PID controller.

As the image quality techniques were explained in Chapter 3, in this research, we used the objective strategy (no-reference (NR) IQA method). A no-reference image quality matrix computes quality scores according to expected image statistics. NR algorithms require knowledge about anticipated distortions according to training examples and corresponding human opinion scores. We used Matlab® PIQE, NIQE, and BRISQUE algorithms to compare the quality of images with- and without PID controller. Figure 4.13 (a) and (b) are the input arguments of these functions. The quality scale of images with these three algorithms is presented in Table 4.6.

**Table 4.6 Scale of onion images epidermis with- and without PID controller evaluated by NR algorithms.**

NR IQA Algorithm	Scale		Which image is better? <i>(The lower value scale means better perceptual quality of image)</i>
	With PID Controller	Without PID Controller	
PIQE	80.5	82.8	With PID Controller
NIQE	9.9	10.1	With PID Controller
BRISQUE	43.4	43.5	With PID Controller

The lower values of scale reflect better perceptual quality of image. Therefore, according to Table 4.6, the PID controller was successful in improving the quality of images.

### 4.3.2 3D Images

As the lens moves, the focal point changes to penetrate at different depth. We changed the air pressure from  $0\text{ kPa}$  to  $85\text{ kPa}$  for 60 seconds and simultaneously scanned the X-Y plane of the sample. The 3D images are presented in Figure 4.14.

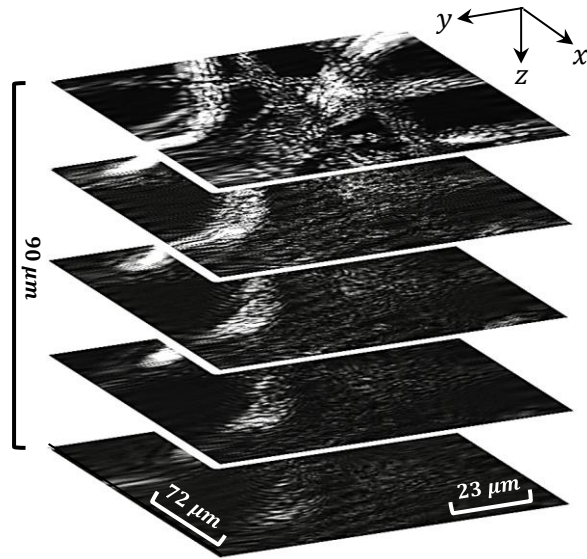


Figure 4.14 3D images of paper fiber with the PID controller.

The imaging capability of the system was demonstrated by imaging some samples. The actuator designed in this study has several advantages that make it attractive for further clinical applications. The scanner is driven by pneumatic forces only, and provides large scanning range that is desired in clinical applications. The Z-scanner combined with X-Y scanner provides 3D images. The proposed system could be used to provide a non-invasive clinical diagnosis. However, more improvement and miniaturization should be considered to form a catheter for commercial endoscopic applications.

## Chapter 5: Conclusion and Future Work

The focus of this study is confocal imaging technology for improving early cancer detection. The proposed transmissive scanning actuator moves the laser beam focal point inside the sample without changing the focal length of the optical system. This not only results in constant spatial resolution regardless of different tissue depth, but also facilitates convenient Z-scanning in the MEMS confocal engine. The designed actuator which has a displacement range of  $200\ \mu\text{m}$ , demonstrates low frequency, high resolution, and good stability. We used one optical fiber to determine the deflection of the actuator as a function of air pressure as well as a Laser Doppler Vibrometer (LDV). In our designed control system, the air pressure resolution is  $0.83\ \text{kPa}$  and the designed two- and one-channel actuators show an axial resolution of  $1.12\ \mu\text{m}$ . The theoretical axial resolution of the confocal scanner is  $21.5\ \mu\text{m}$ . To demonstrate the functionality of the proposed system, paper fiber and onion epidermis were used to obtain some images. The X-Y resolution of the images is  $1.41\ \mu\text{m}$  and the Field of View (FOV) is around  $100\ \mu\text{m} \times 100\ \mu\text{m}$  with the frame rate of 1.25 fps. It was observed that using the PID controller would improve the quality of images. The Z-scanner combined with X-Y scanner to provide 3D images.

Five methods of theoretical, experimental and simulation analysis were used to observe the behavior of the PDMS actuator subjected to air pressure. Using COMSOL® Multiphysics, FEM simulation was conducted. The results of the FEM simulation, theoretical and experimental methods are in a good fit.

The *Impulse Response Identification* method using step responses reveals that the system is a first-order system. A simplified LPV system was used for this system. The proposed reconfigurable electric board platform was built to operate and control the designed soft actuator. The MEMS actuator is controlled by the control electronics, and the whole system operation is controlled and synchronized by the PC. For advanced testing of the actuator, the Arduino IDE application was used that will automate the operation of the control board. For the PID controller, many

experiments and methods (manual tuning by trial and error method, the PID tuner of the Matlab<sup>®</sup>, Genetic Algorithms) were conducted to obtain the optimized PID parameters. According to the results, a PI controller would be enough for this system. Result of experiments demonstrates the authenticity of the results of GA, and adds confidence that the algorithm works well. The average PID parameters are close enough to the ones obtained by experiments. The PID controller was successful to eliminate disturbances and provide a stable position for the actuator. Results show that the PID controller could improve the performance and position stability of the actuator by 94% for the offset error and 76% for the standard deviation. We also used NIQE, BRISQUE, and PIQE image processing algorithms to evaluate the quality of images provided by PID controller. Results show that PID controller was successful to provide better image quality compared to the system without PID controller.

Different PDMS ratios were used to observe the deflection of the PDMS actuator. The higher the PR is, the lower the elasticity modulus (meaning a higher displacement). For a specific air pressure, the thicker PDMS membrane shows a smaller deflection. The very thin actuator has a non-linear behavior compared to the two other actuators that make the process of controlling the actuator more difficult. For 100  $\mu m$  deflection, the 0.45 *mm* PDMS membrane thickness actuator is the ideal case. For taking images, we used 0.45 *mm* thickness. We found that the PDMS Ratio of 15:1 (as a common case) was appropriate for fabrication of membrane actuator.

The available scanning lens in this research was not very small, but we envision that the final scanning lens can have a size of 1.0 *mm* diameter, while the collimating lens can be 1.25 *mm*. On the other hand, using a pneumatic actuation was successful but there were some challenges such as the leakage of air throughout the tubing. In addition, using the smaller lens could improve the overall resolution of images. As the future design, we also 3D printed the actuator with four channels as shown in Figure 5.1. Having these channels allows control of the actuator tilting angle through the X- and Y-axis. Therefore, the actuator could have a better performance, but a more complicated controller should be designed for this actuator.



**Figure 5.1 3D printed design of a future four-channel MEMS actuator.**

It was challenging to fully synchronize the X-Y and Z-scanners in this research. Therefore, other platforms could be designed to improve the performance of the system and improve the compatibility of X-Y and Z-scanner actuators simultaneously. Although this system could be used to provide non-invasive clinical diagnosis, to form a catheter for commercial endoscopic applications more improvement and miniaturization should be considered. In future work, we could acquire confocal images from some patients. Many biopsies are required to detect the highest rate of cancer with more than 90% confidence. Consequently, this leads to patients suffering and significant health care cost. We are hoping to reduce the number of biopsies with the assist of the proposed system, but the exact number will need to be studied further.

## Bibliography

- [1] J. Ferlay *et al.*, “GLOBOCAN 2012: estimated cancer incidence, mortality and prevalence worldwide in 2012,” *Int J Cancer*, vol. 136, pp. E359–E386, 2012.
- [2] M. H. Forouzanfar *et al.*, “Global, regional, and national comparative risk assessment of 79 behavioural, environmental and occupational, and metabolic risks or clusters of risks, 1990–2015: a systematic analysis for the Global Burden of Disease Study 2015,” *Lancet*, vol. 388, no. 10053, pp. 1659–1724, 2016.
- [3] “Gastrointestinal Cancers: An Urgent Need.” [Online]. Available: <https://www.gicancersalliance.org/resources/gastrointestinal-cancers-an-urgent-need/>.
- [4] M. Plummer, C. de Martel, J. Vignat, J. Ferlay, F. Bray, and S. Franceschi, “Global burden of cancers attributable to infections in 2012: a synthetic analysis,” *Lancet Glob. Heal.*, vol. 4, no. 9, pp. e609–e616, 2016.
- [5] B. Stewart and C. P. Wild, “World cancer report 2014,” 2014.
- [6] T. J. Charters, E. C. Strumpf, and M. J. Sewitch, “Effectiveness of an organized colorectal cancer screening program on increasing adherence in asymptomatic average-risk Canadians,” *BMC Health Serv. Res.*, vol. 13, no. 1, p. 449, 2013.
- [7] M. D. Kappelman *et al.*, “Risk of cancer in patients with inflammatory bowel diseases: a nationwide population-based cohort study with 30 years of follow-up evaluation,” *Clin. Gastroenterol. Hepatol.*, vol. 12, no. 2, pp. 265–273, 2014.
- [8] C. E. Rubin, “Histological classification of chronic gastritis: An iconoclastic view,” *Gastroenterology*, vol. 102, no. 1, pp. 360–361, 1992.
- [9] C. Atuma, V. Strugala, A. Allen, and L. Holm, “The adherent gastrointestinal mucus gel layer: thickness and physical state in vivo,” *Am. J. Physiol. Liver Physiol.*, vol. 280, no. 5, pp. G922–G929, 2001.

- [10] “Survival statistics for stomach cancer.” [Online]. Available: <https://www.cancer.ca/en/cancer-information/cancer-type/stomach/prognosis-and-survival/survival-statistics/?region=on>.
- [11] “Stomach (Gastric) Cancer.” [Online]. Available: <http://www.heartburntucson.com/procedures/stomach-cancer-symptoms/>.
- [12] D. A. Skoog, F. J. Holler, and S. R. Crouch, *Principles of instrumental analysis*. Cengage learning, 2017.
- [13] R. Herrmann and C. Onkelinx, “Quantities and units in clinical chemistry: Nebulizer and flame properties in flame emission and absorption spectrometry (Recommendations 1986),” *Pure Appl. Chem.*, vol. 58, no. 12, pp. 1737–1742, 1986.
- [14] T. Schmid, L. Opilik, C. Blum, and R. Zenobi, “Nanoscale chemical imaging using tip-enhanced Raman spectroscopy: a critical review,” *Angew. Chemie Int. Ed.*, vol. 52, no. 23, pp. 5940–5954, 2013.
- [15] P. E. Paull, B. J. Hyatt, W. Wassef, and A. H. Fischer, “Confocal laser endomicroscopy: a primer for pathologists,” *Arch. Pathol. Lab. Med.*, vol. 135, no. 10, pp. 1343–1348, 2011.
- [16] J. T. C. Liu, N. O. Loewke, M. J. Mandella, R. M. Levenson, J. M. Crawford, and C. H. Contag, “Point-of-care pathology with miniature microscopes,” *Anal. Cell. Pathol.*, vol. 34, no. 3, pp. 81–98, 2011.
- [17] J. M. Jabbour, M. A. Saldua, J. N. Bixler, and K. C. Maitland, “Confocal endomicroscopy: instrumentation and medical applications,” *Ann. Biomed. Eng.*, vol. 40, no. 2, pp. 378–397, 2012.
- [18] R. C. Newton *et al.*, “Progress toward optical biopsy: bringing the microscope to the patient,” *Lung*, vol. 189, no. 2, pp. 111–119, 2011.
- [19] S. Coda and A. V. Thillainayagam, “State of the art in advanced endoscopic imaging for the detection and evaluation of dysplasia and early cancer of the gastrointestinal tract,” *Clin. Exp. Gastroenterol.*, vol. 7, p. 133, 2014.

- [20] D. Huang *et al.*, “Optical coherence tomography,” *Science (80-. )*, vol. 254, no. 5035, pp. 1178–1181, 1991.
- [21] A. M. Zysk, F. T. Nguyen, A. L. Oldenburg, D. L. Marks, and S. A. Boppart, “Optical coherence tomography: a review of clinical development from bench to bedside,” *J. Biomed. Opt.*, vol. 12, no. 5, p. 51403, 2007.
- [22] K. Koenig and I. Riemann, “High-resolution multiphoton tomography of human skin with subcellular spatial resolution and picosecond time resolution,” *J. Biomed. Opt.*, vol. 8, no. 3, pp. 432–440, 2003.
- [23] W. Denk, J. H. Strickler, and W. W. Webb, “Two-photon laser scanning fluorescence microscopy,” *Science (80-. )*, vol. 248, no. 4951, pp. 73–76, 1990.
- [24] M. Rajadhyaksha, M. Grossman, D. Esterowitz, R. H. Webb, and R. R. Anderson, “In vivo confocal scanning laser microscopy of human skin: melanin provides strong contrast,” *J. Invest. Dermatol.*, vol. 104, no. 6, pp. 946–952, 1995.
- [25] K. S. Nehal, D. Gareau, and M. Rajadhyaksha, “Skin imaging with reflectance confocal microscopy,” in *Seminars in cutaneous medicine and surgery*, 2008, vol. 27, no. 1, pp. 37–43.
- [26] L. Thiberville, S. Moreno-Swirc, T. Vercauteren, E. Peltier, C. Cavé, and G. Bourg Heckly, “In vivo imaging of the bronchial wall microstructure using fibered confocal fluorescence microscopy,” *Am. J. Respir. Crit. Care Med.*, vol. 175, no. 1, pp. 22–31, 2007.
- [27] E. Laemmel, M. Genet, G. Le Goualher, A. Perchant, J.-F. Le Gargasson, and E. Vicaut, “Fibered confocal fluorescence microscopy (Cell-viZio™) facilitates extended imaging in the field of microcirculation,” *J. Vasc. Res.*, vol. 41, no. 5, pp. 400–411, 2004.
- [28] E. E. Hoover and J. A. Squier, “Advances in multiphoton microscopy technology,” *Nat. Photonics*, vol. 7, no. 2, p. 93, 2013.
- [29] F. Prati *et al.*, “Clinical impact of OCT findings during PCI: the CLI-OPCI II study,” *JACC Cardiovasc. Imaging*, vol. 8, no. 11, pp. 1297–1305, 2015.

- [30] D. J. Kadouch, M. E. Schram, M. M. Leeﬂang, J. Limpens, P. I. Spuls, and M. A. de Rie, “In vivo confocal microscopy of basal cell carcinoma: a systematic review of diagnostic accuracy,” *J. Eur. Acad. Dermatology Venereol.*, vol. 29, no. 10, pp. 1890–1897, 2015.
- [31] W. Drexler and J. G. Fujimoto, *Optical coherence tomography: technology and applications*. Springer Science & Business Media, 2008.
- [32] R. Kiesslich and M. F. Neurath, “Endomicroscopy is born—do we still need the pathologist?,” *Gastrointest. Endosc.*, vol. 66, no. 1, pp. 150–153, 2007.
- [33] M. Liedlgruber and A. Uhl, “Computer-aided decision support systems for endoscopy in the gastrointestinal tract: a review,” *IEEE Rev. Biomed. Eng.*, vol. 4, pp. 73–88, 2011.
- [34] L. E. Meyer, N. Otberg, W. Sterry, and J. Lademann, “In vivo confocal scanning laser microscopy: comparison of the reflectance and fluorescence mode by imaging human skin,” *J. Biomed. Opt.*, vol. 11, no. 4, p. 44012, 2006.
- [35] L. Liu and H. Xie, “3-D confocal laser scanning microscopy based on a full-MEMS scanning system,” *IEEE Photonics Technol. Lett.*, vol. 25, no. 15, pp. 1478–1480, 2013.
- [36] Y. Wang *et al.*, “Portable oral cancer detection using a miniature confocal imaging probe with a large field of view,” *J. Micromechanics Microengineering*, vol. 22, no. 6, p. 65001, 2012.
- [37] A. L. Polglase, W. J. McLaren, S. A. Skinner, R. Kiesslich, M. F. Neurath, and P. M. Delaney, “A fluorescence confocal endomicroscope for in vivo microscopy of the upper-and the lower-GI tract,” *Gastrointest. Endosc.*, vol. 62, no. 5, pp. 686–695, 2005.
- [38] M. Nakao *et al.*, “Optical biopsy of early gastroesophageal cancer by catheter-based reflectance-type laser-scanning confocal microscopy,” *J. Biomed. Opt.*, vol. 13, no. 5, p. 54043, 2008.
- [39] C. MacAulay, P. Lane, and R. Richards-Kortum, “In vivo pathology: microendoscopy as a new endoscopic imaging modality,” *Gastrointest. Endosc. Clin.*, vol. 14, no. 3, pp. 595–620, 2004.

- [40] H. Mansoor, “Microfabricated electromagnetic actuators for confocal measurements and imaging.” University of British Columbia, 2013.
- [41] J. M. Bustillo, R. T. Howe, and R. S. Muller, “Surface micromachining for microelectromechanical systems,” *Proc. IEEE*, vol. 86, no. 8, pp. 1552–1574, 1998.
- [42] J. J. Allen, “Introduction to MEMS (MicroElectroMechanical Systems).,” Sandia National Lab.(SNL-NM), Albuquerque, NM (United States), 2007.
- [43] N. Yazdi, F. Ayazi, and K. Najafi, “Micromachined inertial sensors,” *Proc. IEEE*, vol. 86, no. 8, pp. 1640–1659, 1998.
- [44] W. J. Fleming, “Overview of automotive sensors,” *IEEE Sens. J.*, vol. 1, no. 4, pp. 296–308, 2001.
- [45] R. Bashir, “BioMEMS: state-of-the-art in detection, opportunities and prospects,” *Adv. Drug Deliv. Rev.*, vol. 56, no. 11, pp. 1565–1586, 2004.
- [46] G. M. Rebeiz, *RF MEMS: theory, design, and technology*. John Wiley & Sons, 2004.
- [47] D. S. Eddy and D. R. Sparks, “Application of MEMS technology in automotive sensors and actuators,” *Proc. IEEE*, vol. 86, no. 8, pp. 1747–1755, 1998.
- [48] R. A. Conant *et al.*, “A raster-scanning full-motion video display using polysilicon micromachined mirrors,” *Sensors Actuators A Phys.*, vol. 83, no. 1–3, pp. 291–296, 2000.
- [49] F. Krogmann, W. Moench, and H. Zappe, “A MEMS-based variable micro-lens system,” *J. Opt. A Pure Appl. Opt.*, vol. 8, no. 7, p. S330, 2006.
- [50] M. C. Wu, O. Solgaard, and J. E. Ford, “Optical MEMS for lightwave communication,” *J. Light. Technol.*, vol. 24, no. 12, pp. 4433–4454, 2006.
- [51] T. Mitsui, Y. Takahashi, and Y. Watanabe, “A 2-axis optical scanner driven nonresonantly by electromagnetic force for OCT imaging,” *J. Micromechanics Microengineering*, vol. 16, no. 11, p. 2482, 2006.
- [52] H. Urey, “Moems Display And Imaging Systems III (Proceedings of SPIE),” 2005.

- [53] O. Solgaard, A. A. Godil, R. T. Howe, L. P. Lee, Y.-A. Peter, and H. Zappe, "Optical MEMS: From micromirrors to complex systems," *J. Microelectromechanical Syst.*, vol. 23, no. 3, pp. 517–538, 2014.
- [54] L. Liu, E. Wang, X. Zhang, W. Liang, X. Li, and H. Xie, "MEMS-based 3D confocal scanning microendoscope using MEMS scanners for both lateral and axial scan," *Sensors Actuators A Phys.*, vol. 215, pp. 89–95, 2014.
- [55] S. T. S. Holmström, U. Baran, and H. Urey, "MEMS laser scanners: a review," *J. Microelectromechanical Syst.*, vol. 23, no. 2, pp. 259–275, 2014.
- [56] H. Li *et al.*, "Integrated monolithic 3D MEMS scanner for switchable real time vertical/horizontal cross-sectional imaging," *Opt. Express*, vol. 24, no. 3, pp. 2145–2155, 2016.
- [57] H. Mansoor, H. Zeng, I. T. Tai, J. Zhao, and M. Chiao, "A handheld electromagnetically actuated fiber optic raster scanner for reflectance confocal imaging of biological tissues," *IEEE Trans. Biomed. Eng.*, vol. 60, no. 5, pp. 1431–1438, 2012.
- [58] H. Mansoor, H. Zeng, K. Chen, Y. Yu, J. Zhao, and M. Chiao, "Vertical optical sectioning using a magnetically driven confocal microscanner aimed for in vivo clinical imaging," *Opt. Express*, vol. 19, no. 25, pp. 25161–25172, 2011.
- [59] R. W. Johnstone and A. Parmaswaran, *An introduction to surface-micromachining*. Springer Science & Business Media, 2004.
- [60] W.-H. Lin and Y.-P. Zhao, "Nonlinear behavior for nanoscale electrostatic actuators with Casimir force," *Chaos, Solitons & Fractals*, vol. 23, no. 5, pp. 1777–1785, 2005.
- [61] S. Weinberger, T. T. Nguyen, R. Lecomte, Y. Cheriguen, C. Ament, and M. Hoffmann, "Linearized control of an uniaxial micromirror with electrostatic parallel-plate actuation," *Microsyst. Technol.*, vol. 22, no. 2, pp. 441–447, 2016.
- [62] T. Izawa, T. Sasaki, and K. Hane, "Scanning micro-mirror with an electrostatic spring for compensation of hard-spring nonlinearity," *Micromachines*, vol. 8, no. 8, p. 240, 2017.

- [63] Y. Fan, C. Cui, H. Yu, W. Shen, Z. Wang, and J. Li, "An electrostatic vertical comb-drive micromirror with self-aligned assembly," in *2017 IEEE 12th International Conference on Nano/Micro Engineered and Molecular Systems (NEMS)*, 2017, pp. 268–272.
- [64] L. Yan, I.-M. Chen, C. K. Lim, G. Yang, and K.-M. Lee, *Design, modeling and experiments of 3-DOF electromagnetic spherical actuators*, vol. 4. Springer Science & Business Media, 2011.
- [65] O. Gomis-Bellmunt and L. F. Campanile, *Design rules for actuators in active mechanical systems*. Springer Science & Business Media, 2009.
- [66] S. Ju, H. Jeong, J.-H. Park, J.-U. Bu, and C.-H. Ji, "Electromagnetic 2D scanning micromirror for high definition laser projection displays," *IEEE Photonics Technol. Lett.*, vol. 30, no. 23, pp. 2072–2075, 2018.
- [67] A. R. Cho *et al.*, "Electromagnetic biaxial microscanner with mechanical amplification at resonance," *Opt. Express*, vol. 23, no. 13, pp. 16792–16802, 2015.
- [68] J.-H. Kim, H. Jeong, S.-K. Lee, C.-H. Ji, and J.-H. Park, "Electromagnetically actuated biaxial scanning micromirror fabricated with silicon on glass wafer," *Microsyst. Technol.*, vol. 23, no. 6, pp. 2075–2085, 2017.
- [69] A. Manbachi and R. S. C. Cobbold, "Development and application of piezoelectric materials for ultrasound generation and detection," *Ultrasound*, vol. 19, no. 4, pp. 187–196, 2011.
- [70] G. Gaultschi, "Piezoelectric sensors," in *Piezoelectric Sensorics*, Springer, 2002, pp. 73–91.
- [71] K. Uchino, "Ferroelectric Devices Marcel Dekker, Inc," *New York*, 2000.
- [72] K. Uchino, *Piezoelectric actuators and ultrasonic motors*, vol. 1. Springer Science & Business Media, 1996.
- [73] K. Uchino, "Piezoelectric actuators: expansion from IT/robotics to ecological/energy applications," *J. Japan Soc. Appl. Electromagn.*, vol. 15, no. 4, pp. 399–409, 2007.
- [74] H. Lei *et al.*, "AlN film based piezoelectric large-aperture MEMS scanning micromirror integrated with angle sensors," *J. Micromechanics Microengineering*, vol. 28, no. 11, p. 115012, 2018.

- [75] K. H. Koh, T. Kobayashi, F.-L. Hsiao, and C. Lee, "Characterization of piezoelectric PZT beam actuators for driving 2D scanning micromirrors," *Sensors Actuators A Phys.*, vol. 162, no. 2, pp. 336–347, 2010.
- [76] J.-S. Park, L. L. Chu, A. D. Oliver, and Y. B. Gianchandani, "Bent-beam electrothermal actuators-Part II: Linear and rotary microengines," *J. Microelectromechanical Syst.*, vol. 10, no. 2, pp. 255–262, 2001.
- [77] R. Cragun and L. L. Howell, "Linear thermomechanical microactuators," in *Proc. ASME IMECE*, 1999, pp. 181–188.
- [78] L. L. Chu and Y. B. Gianchandani, "A micromachined 2D positioner with electrothermal actuation and sub-nanometer capacitive sensing," *J. Micromechanics Microengineering*, vol. 13, no. 2, p. 279, 2003.
- [79] C. D. Lott, T. W. McLain, J. N. Harb, and L. L. Howell, "Modeling the thermal behavior of a surface-micromachined linear-displacement thermomechanical microactuator," *Sensors Actuators A Phys.*, vol. 101, no. 1–2, pp. 239–250, 2002.
- [80] N. B. Hubbard, M. L. Culpepper, and L. L. Howell, "Actuators for micropositioners and nanopositioners," *Appl. Mech. Rev.*, vol. 59, no. 6, pp. 324–334, 2006.
- [81] J. Luo *et al.*, "A large-piston scanning electrothermal micromirror with a temperature control frame," in *2016 International Conference on Optical MEMS and Nanophotonics (OMN)*, 2016, pp. 1–2.
- [82] H. Janocha, *Adaptronics and smart structures*. Springer, 1999.
- [83] H. Janocha, *Actuators*. Springer, 2004.
- [84] A. AbuZaiter, O. F. Hikmat, M. Nafea, and M. S. M. Ali, "Design and fabrication of a novel XYθz monolithic micro-positioning stage driven by NiTi shape-memory-alloy actuators," *Smart Mater. Struct.*, vol. 25, no. 10, p. 105004, 2016.
- [85] Y. Hwang, O. H. Paydar, and R. N. Candler, "Pneumatic microfinger with balloon fins for linear motion using 3D printed molds," *Sensors Actuators A Phys.*, vol. 234, pp. 65–71, 2015.

- [86] Y. Lu and C.-J. Kim, "Micro-finger articulation by pneumatic parylene balloons," in *TRANSDUCERS'03. 12th International Conference on Solid-State Sensors, Actuators and Microsystems. Digest of Technical Papers (Cat. No. 03TH8664)*, 2003, vol. 1, pp. 276–279.
- [87] O. C. Jeong and S. Konishi, "All PDMS pneumatic microfinger with bidirectional motion and its application," *J. Microelectromechanical Syst.*, vol. 15, no. 4, pp. 896–903, 2006.
- [88] S. Konishi, F. Kawai, and P. Cusin, "Thin flexible end-effector using pneumatic balloon actuator," *Sensors Actuators A Phys.*, vol. 89, no. 1–2, pp. 28–35, 2001.
- [89] J. P. Hubschman *et al.*, "'The Microhand': a new concept of micro-forceps for ocular robotic surgery," *Eye*, vol. 24, no. 2, p. 364, 2010.
- [90] O. C. Jeong, S. Kusuda, T. Sakakibara, S. Konishi, and M. Nokata, "Pneumatic micro finger as endeffector of robot," in *IEEE International Symposium on Micro-NanoMechatronics and Human Science, 2005*, 2005, pp. 145–148.
- [91] B. Gorissen, M. De Volder, A. De Greef, and D. Reynaerts, "Theoretical and experimental analysis of pneumatic balloon microactuators," *Sensors Actuators A Phys.*, vol. 168, no. 1, pp. 58–65, 2011.
- [92] L. Zheng, S. Yoshida, Y. Morimoto, H. Onoe, and S. Takeuchi, "Pneumatic balloon actuator with tunable bending points," in *2015 28th IEEE International Conference on Micro Electro Mechanical Systems (MEMS)*, 2015, pp. 18–21.
- [93] S. Konishi, "Merging micro and macro robotics toward micro manipulation for biomedical operation," in *Proceedings of the 36th International Symposium on Robotics (ISR 2005)*, 2005.
- [94] B. Gorissen, T. Chishiro, S. Shimomura, D. Reynaerts, M. De Volder, and S. Konishi, "Flexible pneumatic twisting actuators and their application to tilting micromirrors," *Sensors Actuators A Phys.*, vol. 216, pp. 426–431, 2014.
- [95] S. Bütetfisch, V. Seidemann, and S. Büttgenbach, "Novel micro-pneumatic actuator for MEMS," *Sensors Actuators A Phys.*, vol. 97, pp. 638–645, 2002.

- [96] Y. Shapiro, A. Wolf, and K. Gabor, “Bi-bellows: Pneumatic bending actuator,” *Sensors Actuators A Phys.*, vol. 167, no. 2, pp. 484–494, 2011.
- [97] T. Yukisawa, Y. Ishii, S. Nishikawa, R. Niiyama, and Y. Kuniyoshi, “Modeling of extensible pneumatic actuator with bellows (EPAB) for continuum arm,” in *2017 IEEE International Conference on Robotics and Biomimetics (ROBIO)*, 2017, pp. 2303–2308.
- [98] D. Drotman, M. Ishida, S. Jadhav, and M. T. Tolley, “Application-Driven Design of Soft, 3-D Printed, Pneumatic Actuators With Bellows,” *IEEE/ASME Trans. Mechatronics*, vol. 24, no. 1, pp. 78–87, 2018.
- [99] M. Sudani, M. Deng, and S. Wakimoto, “Modelling and Operator-Based Nonlinear Control for a Miniature Pneumatic Bending Rubber Actuator Considering Bellows,” in *Actuators*, 2018, vol. 7, no. 2, p. 26.
- [100] S. Li, D. M. Vogt, D. Rus, and R. J. Wood, “Fluid-driven origami-inspired artificial muscles,” *Proc. Natl. Acad. Sci.*, vol. 114, no. 50, pp. 13132–13137, 2017.
- [101] J. D. Greer, T. K. Morimoto, A. M. Okamura, and E. W. Hawkes, “Series pneumatic artificial muscles (sPAMs) and application to a soft continuum robot,” in *2017 IEEE International Conference on Robotics and Automation (ICRA)*, 2017, pp. 5503–5510.
- [102] J. Sárosi, I. Biro, J. Nemeth, and L. Cveticanin, “Dynamic modeling of a pneumatic muscle actuator with two-direction motion,” *Mech. Mach. Theory*, vol. 85, pp. 25–34, 2015.
- [103] G. A. A. Rodríguez, C. Rossi, and K. Zhang, “Multi-physics system modeling of a pneumatic micro actuator,” *Sensors Actuators A Phys.*, vol. 141, no. 2, pp. 489–498, 2008.
- [104] P. Rothmund *et al.*, “A soft, bistable valve for autonomous control of soft actuators,” *Sci Robot*, vol. 3, no. 16, p. 7986, 2018.
- [105] K. J. Gabriel, O. Tabata, K. Shimaoka, S. Sugiyama, and H. Fujita, “Surface-normal electrostatic/pneumatic actuator,” in *[1992] Proceedings IEEE Micro Electro Mechanical Systems*, 1992, pp. 128–132.

- [106] W. Zhang, M. L. Accorsi, and J. W. Leonard, “Analysis of geometrically nonlinear anisotropic membranes: application to pneumatic muscle actuators,” *Finite Elem. Anal. Des.*, vol. 41, no. 9–10, pp. 944–962, 2005.
- [107] C.-H. Chiou, T.-Y. Yeh, and -Lung Lin Jr, “Deformation analysis of a pneumatically-activated polydimethylsiloxane (PDMS) membrane and potential micro-pump applications,” *Micromachines*, vol. 6, no. 2, pp. 216–229, 2015.
- [108] D. J. Bell, T. J. Lu, N. A. Fleck, and S. M. Spearing, “MEMS actuators and sensors: observations on their performance and selection for purpose,” *J. Micromechanics Microengineering*, vol. 15, no. 7, p. S153, 2005.
- [109] M. Zupan, M. F. Ashby, and N. A. Fleck, “Actuator classification and selection—the development of a database,” *Adv. Eng. Mater.*, vol. 4, no. 12, pp. 933–940, 2002.
- [110] J. E. Huber, N. A. Fleck, and M. F. Ashby, “The selection of mechanical actuators based on performance indices,” *Proc. R. Soc. London. Ser. A Math. Phys. Eng. Sci.*, vol. 453, no. 1965, pp. 2185–2205, 1997.
- [111] Y. Hwang and R. N. Candler, “Non-planar PDMS microfluidic channels and actuators: a review,” *Lab Chip*, vol. 17, no. 23, pp. 3948–3959, 2017.
- [112] I. Wong and C.-M. Ho, “Surface molecular property modifications for poly (dimethylsiloxane)(PDMS) based microfluidic devices,” *Microfluid. Nanofluidics*, vol. 7, no. 3, p. 291, 2009.
- [113] D. Fuard, T. Tzvetkova-Chevolleau, S. Decossas, P. Tracqui, and P. Schiavone, “Optimization of poly-di-methyl-siloxane (PDMS) substrates for studying cellular adhesion and motility,” *Microelectron. Eng.*, vol. 85, no. 5–6, pp. 1289–1293, 2008.
- [114] Z. Wang, “Polydimethylsiloxane mechanical properties measured by macroscopic compression and nanoindentation techniques,” 2011.
- [115] “How to do PDMS lithography replication from a SU-8 mold.” .

- [116] M. Bélanger and Y. Marois, “Hemocompatibility, biocompatibility, inflammatory and in vivo studies of primary reference materials low-density polyethylene and polydimethylsiloxane: A review,” *J. Biomed. Mater. Res. An Off. J. Soc. Biomater. Japanese Soc. Biomater. Aust. Soc. Biomater. Korean Soc. Biomater.*, vol. 58, no. 5, pp. 467–477, 2001.
- [117] J. O. Iroh and J. E. Mark, “Polymer data handbook.” Oxford University Press, New York, 1999.
- [118] Z. Wang, A. A. Volinsky, and N. D. Gallant, “Crosslinking effect on polydimethylsiloxane elastic modulus measured by custom-built compression instrument,” *J. Appl. Polym. Sci.*, vol. 131, no. 22, 2014.
- [119] D. E. Hanson *et al.*, “Stress softening experiments in silica-filled polydimethylsiloxane provide insight into a mechanism for the Mullins effect,” *Polymer (Guildf)*., vol. 46, no. 24, pp. 10989–10995, 2005.
- [120] H. Hocheng, C.-M. Chen, Y.-C. Chou, and C.-H. Lin, “Study of novel electrical routing and integrated packaging on bio-compatible flexible substrates,” *Microsyst. Technol.*, vol. 16, no. 3, p. 423, 2010.
- [121] D. Armani, C. Liu, and N. Aluru, “Re-configurable fluid circuits by PDMS elastomer micromachining,” in *Technical Digest. IEEE International MEMS 99 Conference. Twelfth IEEE International Conference on Micro Electro Mechanical Systems (Cat. No. 99CH36291)*, 1999, pp. 222–227.
- [122] X. Liang, Y. Sun, and H. Ren, “A flexible fabrication approach toward the shape engineering of microscale soft pneumatic actuators,” *IEEE Robot. Autom. Lett.*, vol. 2, no. 1, pp. 165–170, 2016.
- [123] R. W. Ogden, “Large deformation isotropic elasticity—on the correlation of theory and experiment for incompressible rubberlike solids,” *Proc. R. Soc. London. A. Math. Phys. Sci.*, vol. 326, no. 1567, pp. 565–584, 1972.

- [124] J.-Y. Sun, S. Xia, M.-W. Moon, K. H. Oh, and K.-S. Kim, "Folding wrinkles of a thin stiff layer on a soft substrate," *Proc. R. Soc. A Math. Phys. Eng. Sci.*, vol. 468, no. 2140, pp. 932–953, 2011.
- [125] T. K. Kim, J. K. Kim, and O. C. Jeong, "Measurement of nonlinear mechanical properties of PDMS elastomer," *Microelectron. Eng.*, vol. 88, no. 8, pp. 1982–1985, 2011.
- [126] S. P. Timoshenko and S. Woinowsky-Krieger, *Theory of plates and shells*. McGraw-hill, 1959.
- [127] A. P. Boresi, R. J. Schmidt, and O. M. Sidebottom, *Advanced mechanics of materials*, vol. 6. Wiley New York et al., 1985.
- [128] G. Martin, "Thickness of an optical sectiono," *Thickness of an optical section, Keck Microscopy Facility., University of Washington*, 2007. [Online]. Available: <http://depts.washington.edu/keck/leica/pinhole.htm>.
- [129] R. Isermann and M. Münchhof, *Identification of dynamic systems: an introduction with applications*. Springer Science & Business Media, 2010.
- [130] K. J. Keesman, *System identification: an introduction*. Springer Science & Business Media, 2011.
- [131] A. Visioli, *Practical PID control*. Springer Science & Business Media, 2006.
- [132] L. Ljung, "SyStem Identification: Theory for the User", Prentice-Hall, New Jersey," 1987.
- [133] J. S. Shamma and M. Athans, "Guaranteed properties of gain scheduled control for linear parameter-varying plants," *Automatica*, vol. 27, no. 3, pp. 559–564, 1991.
- [134] P. Gáspár, Z. Szabó, J. Bokor, and B. Nemeth, "Robust control design for active driver assistance systems," *Springer, DOI*, vol. 10, pp. 973–978, 2016.
- [135] S. Bennett, "The past of PID controllers," *IFAC Proc. Vol.*, vol. 33, no. 4, pp. 1–11, 2000.
- [136] M. A. Johnson and M. H. Moradi, *PID control*. Springer, 2005.
- [137] M. Gen and L. Lin, "Genetic algorithms," *Wiley Encycl. Comput. Sci. Eng.*, pp. 1–15, 2007.
- [138] D. E. Goldberg, "Genetic algorithms in search," *Optim. Mach.*, 1989.

- [139] E. E. Vladu and T. L. Dragomir, "Controller tuning using genetic algorithms," *Int. J. Res. Eng. Technol.*, pp. 1–10, 2004.
- [140] B. Nagaraj, S. Subha, and B. Rampriya, "Tuning algorithms for PID controller using soft computing techniques," *Int. J. Comput. Sci. Netw. Secur.*, vol. 8, no. 4, pp. 278–281, 2008.
- [141] A. Jayachitra and R. Vinodha, "Genetic algorithm based PID controller tuning approach for continuous stirred tank reactor," *Adv. Artif. Intell.*, vol. 2014, p. 9, 2014.
- [142] J. M. Amaral, R. Tanscheit, and M. A. Pacheco, "Tuning PID controllers through genetic algorithms," *complex Syst.*, vol. 2, p. 3, 2018.
- [143] M. Ibrahim and S. Bin, "The PID controller design using genetic algorithm," 2005.
- [144] A. Mirzal, S. Yoshii, and M. Furukawa, "PID parameters optimization by using genetic algorithm," *arXiv Prepr. arXiv1204.0885*, 2012.
- [145] B. Keelan, *Handbook of image quality: characterization and prediction*. CRC Press, 2002.
- [146] "Image Quality Metrics." [Online]. Available:  
<https://www.mathworks.com/help/images/image-quality-metrics.html>.
- [147] Z. Wang and A. C. Bovik, "Modern image quality assessment," *Synth. Lect. Image, Video, Multimed. Process.*, vol. 2, no. 1, pp. 1–156, 2006.
- [148] Y. Fu and S. Wang, "A no reference image quality assessment metric based on visual perception," *Algorithms*, vol. 9, no. 4, p. 87, 2016.
- [149] A. Mittal, R. Soundararajan, and A. C. Bovik, "Making a 'completely blind' image quality analyzer," *IEEE Signal Process. Lett.*, vol. 20, no. 3, pp. 209–212, 2012.
- [150] N. Venkatanath, D. Praneeth, M. C. Bh, S. S. Channappayya, and S. S. Medasani, "Blind image quality evaluation using perception based features," in *2015 Twenty First National Conference on Communications (NCC)*, 2015, pp. 1–6.
- [151] M. G. Choi, J. H. Jung, and J. W. Jeon, "No-reference image quality assessment using blur and noise," *Int. J. Comput. Sci. Eng.*, vol. 3, no. 2, pp. 76–80, 2009.
- [152] R. Fan, "A Piezoelectric Fiber Scanner for Reflectance Confocal Imaging of Biological Tissues," The University of British Columbia, 2019.

- [153] M. D. Symes *et al.*, “Integrated 3D-printed reactionware for chemical synthesis and analysis,” *Nat. Chem.*, vol. 4, no. 5, p. 349, 2012.
- [154] M. S. Mannoer *et al.*, “3D printed bionic ears,” *Nano Lett.*, vol. 13, no. 6, pp. 2634–2639, 2013.
- [155] P. Lutzmann, B. Göhler, C. A. Hill, and F. D. M. van Putten, “Laser vibration sensing at Fraunhofer IOSB: review and applications,” *Opt. Eng.*, vol. 56, no. 3, p. 31215, 2016.
- [156] “LDV Schematic.” [Online]. Available:  
[https://en.wikipedia.org/wiki/Laser\\_Doppler\\_vibrometer](https://en.wikipedia.org/wiki/Laser_Doppler_vibrometer)
- [157] J. P. Holman, *Experimental methods for engineers*. 2001.

## Appendices

### Appendix A (Balloon (Cantilever) Actuator)

The molding processes typically used to define miniature balloon actuators are based on planar microfabrication techniques. Consequently, balloon actuators typically consist of several stacks of diaphragms which require multiple iterations of photolithographic steps [87]. It should be noted that the cost and inconvenience of this fabrication method have a limited introduction of novel designs. 3D printing technology is an innovative computer-controlled process in which material is solidified typically layer by layer to create a 3D object. This technology results in the manufacture of very complex objects. Taking advantage of this technology, rapid prototyping of structures from a mold for PDMS devices to structures that are impractical through existing soft lithography techniques (e.g., non-planar cross-section) [155, 156] would be possible. In this research, molds were 3D printed directly from computer-aided design (CAD) files.

#### A.1 Working Principle of Pneumatic Balloon Actuators

The working principle of pneumatic balloon actuators is as follows:

Generally, a balloon actuator has three components, which include the bottom layer, top layer, and a cavity. A thin air channel is embedded in a rectangular PDMS beam structure with asymmetric upper- and lower-layer thickness. To generate an unbalanced force by applying air pressure, designers should consider an asymmetrical design in actuator's geometry to bend this type of pneumatic actuator. When the air channel (cavity) is pressurized, the balloon cavity inflates. Therefore, the difference in strain between the top and the bottom layer results in an out-of-plane deflection of the entire structure. The out-of-plane motion is determined by the ratio of top-layer thickness to bottom-layer thickness [87]. The actuator bends towards the thicker layer side because of the pressurized air expands the thin layer more. The amount of force resulted in the operating angle or deflection depends on the applied air pressure. If the actuator has been made of a material with nonlinear mechanical behavior (elastomers), under certain loads and

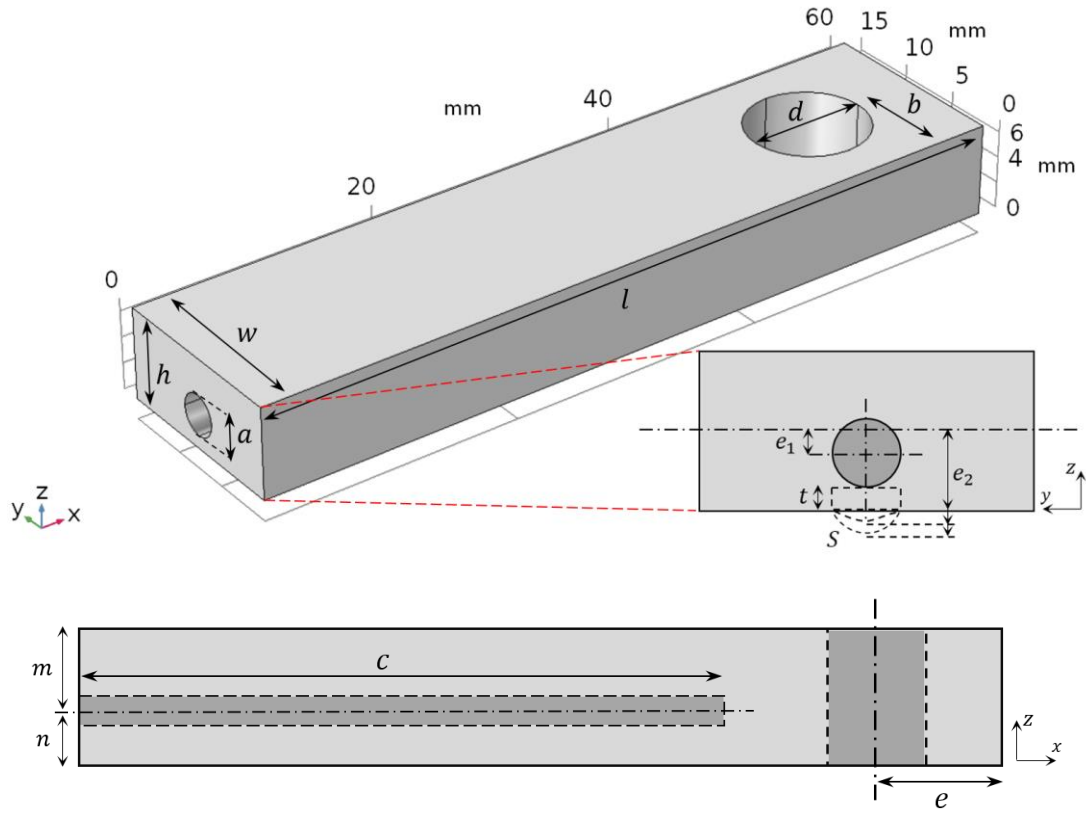
boundary conditions, a nonlinear bending behavior should be observed in response to applied pressures [125]. Large deflection can be achieved using elastomers which was discussed in Chapter 1 [86, 87].

## A.2 Design Concept of the Pneumatic Balloon Actuator

For the first design, a balloon (cantilever) actuator with different geometrical dimensions was fabricated. As shown in Figure A.1, according to the deflection of the actuator with respect to the applied air pressure, the final design is as follows: a thin air channel ( $a = 2.1 \text{ mm}$ ) was embedded in a rectangular PDMS beam structure ( $60 \times 14 \times 5 \text{ mm}$ ) with asymmetric upper- ( $1.9 \text{ mm}$ ) and lower-layer ( $1 \text{ mm}$ ) thickness. A hole was considered in the tip of the beam structure to embed the optical lens there. Figure A.1 (a, b) shows the modeling diagram and concept design of pneumatic balloon actuator and the fabricated balloon actuator after curing the PDMS with geometries listed in Table A.1. The 3D printed mold for fabrication of PDMS balloon actuator is shown in Figure A.1 (c). The geometrical dimensions for the design of the pneumatic balloon actuator are presented in Table A.1.

**Table A.1 Geometrical dimensions of the pneumatic balloon actuator.**

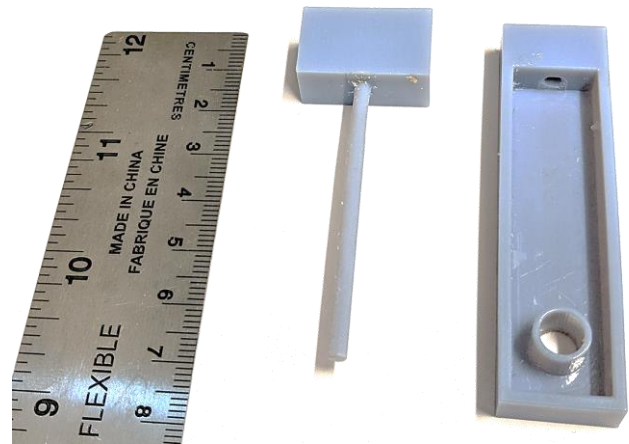
Parameter	Value ( $mm$ )
$a$	2.1
$b$	7
$c$	40
$d$	9.1
$e$	9.55
$h$	5
$l$	60
$m$	2.95
$n$	2.05
$w$	14



(a)



(b)



(c)

Figure A.1 Concept design of pneumatic balloon actuator: (a) Modeling diagram of the balloon actuator, (b) Photograph of fabricated balloon actuator with geometries listed in Table A.1, (c) 3D printed mold for fabrication of PDMS balloon actuator.

### A.3 Theoretical Analysis of Pneumatic Balloon Actuator

According to the presented analytical 2D model, the deformation of the balloon actuator subjected to air pressure could be analytically estimated. For modeling soft materials, some assumptions could be made to simplify their analysis: 1) PDMS is incompressible and have a linear stress-strain behavior at low stress ( $< 150 \text{ kPa}$ ) [122], 2) The cross section area of the cavity is small in comparison with the cross section of the actuator, 3) According to the previous assumption, the neutral axis still could be stayed at half of the height of the actuator and the air channel does not have any significant effect on the moment of inertia of the actuator and, 4) Local inflation (inflated arc) is positioned right above the cavity, 5) The inflated arc has a force center at the middle height of the arc, and 6) The effect of gravity is neglected [91].

According to the beam equation of Euler-Bernoulli theory:  $EI = RM$ , where  $R$  is the local curvature radius of the beam,  $M$  is the local bending moment resulted from air pressure,  $E$  is the elastic modulus, the moment of inertia of the cross section area is  $I = \frac{wh^3}{12}$ ,  $w$  is the width of the 2D PBA, and  $h$  is the height of the beam [127]. The local bending moment,  $= M_{ac} + M_{ia}$ , resulted from two parts: 1)  $M_{ac}$ : the moment generated by the air channel of the original area, and 2)  $M_{ia}$ : the moment generated by the extra area (inflated arc). Considering  $a$  as the diameter of the circular channel,  $P$  the pressure,  $e_1$  the distance from the center of the air channel to the neutral axis of the beam,  $S$  the extra area if inflated arc after injecting air into the cavity,  $e_2$  the distance from the middle height of inflated arc to half of the height of the actuator, one can derive [122]:

$$M = M_{ac} + M_{ia} = \frac{\pi P a^2 e_1}{4} + S P e_2 \quad (\text{A.1})$$

The radius and radian of the inflated arc are  $R_{ia}$  and  $\alpha$ , respectively. Also, strain and stress of the stretched PDMS could be assumed as  $\varepsilon$  and  $\sigma$ , respectively. The height of the inflated arc is  $k$ . The thickness of the upper-layer of the actuator before and after injecting air is assumed as  $t$  and  $t'$ , respectively. Therefore, one can derive:

$$ta = t'R_{ia}\alpha \quad (\text{A.2})$$

$$\sigma = E\varepsilon \quad (\text{A.3})$$

$$R_{ia}\alpha = a(\varepsilon + 1) \quad (\text{A.4})$$

$$k = 0.5 a \left(1 - \cos\left(\frac{\alpha}{2}\right)\right) \quad (\text{A.5})$$

$$R_{ia} = 0.5 a \sin^{-1}\left(\frac{\alpha}{2}\right) \quad (\text{A.6})$$

$$t' = 2t \sin\left(\frac{\alpha}{2}\right) \alpha^{-1} \quad (\text{A.7})$$

According to Figure A.2, taking a moment about point  $Z$ , one argues:

$$\sigma t' k - \frac{a^2 P}{8} + \frac{PR_{ia}a \left(1 - \cos\left(\frac{\alpha}{2}\right)\right)}{2 \tan\left(\frac{\alpha}{2}\right)} = 0 \quad (\text{A.8})$$

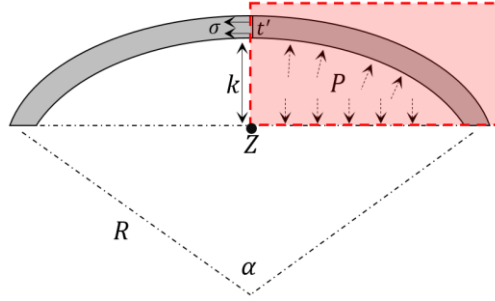


**Figure A.2 Modeling of the inflated arc after injecting the air pressure inside the channel.**

Recasting the previous equations, the relationship between  $P$  and  $\alpha$  could be determined as:

$$P = \frac{4Et \sin\left(\frac{\alpha}{2}\right) \alpha - 2 \sin\left(\frac{\alpha}{2}\right)}{a\alpha} \frac{1 - \cos\left(\frac{\alpha}{2}\right)}{1 - \cos\left(\frac{\alpha}{2}\right)} \quad (\text{A.9})$$

Also,  $S$  and  $e_2$  could be obtained as follows:

$$S = \frac{\alpha R_{ia}^2}{2} - \frac{(R_{ia} - k)a}{2} = \frac{a^2(\alpha - \sin(\alpha))}{8 \sin^2\left(\frac{\alpha}{2}\right)} \quad (\text{A.10})$$

$$e_2 = \frac{k}{2} + \frac{h}{2} \quad (\text{A.11})$$

Based on the equations mentioned above, the maximum deflection of the actuator could be obtained as follows:

$$D_{max} = \frac{Ml^2}{2EI} = \frac{3atl^2[\pi e_1(1 - \cos(\alpha)) + (\alpha - \sin(\alpha))e_2] \left(\alpha - 2 \sin\left(\frac{\alpha}{2}\right)\right)}{\alpha wh^3 \left(\sin\left(\frac{\alpha}{2}\right) - \frac{1}{2}\sin(\alpha)\right)} \quad (\text{A.12})$$

#### A.4 FEM Modeling

To assess the accuracy of the proposed theoretical solution, FEM simulation was used. Using COMSOL® Multiphysics, a 3D model of the balloon actuator was investigated as shown in Figure A.3. The deflection of the tip of the balloon actuator was recorded. The Solid Mechanics Physics was chosen for this analysis. For boundary conditions, all surfaces are free except plane A as indicated in Figure A.3. The gravity was neglected in this simulation. The structure meshed with 83541 free tetrahedral elements. The Stationary Study was used. We considered PDMS with linear material properties and used PR 15:1 for the proposed simulation.

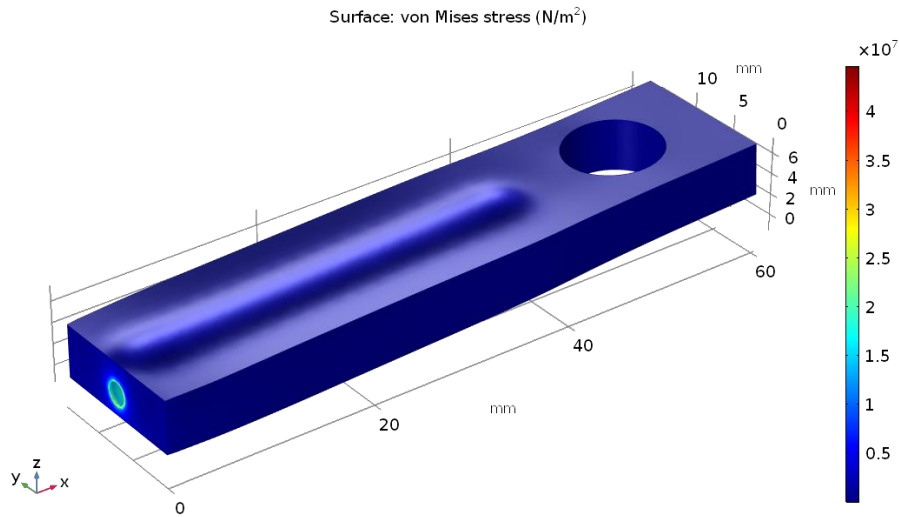
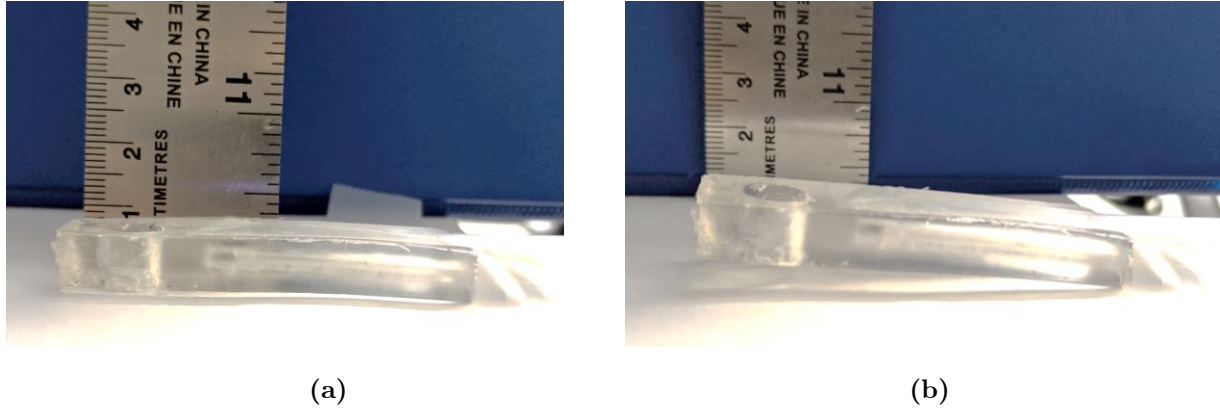


Figure A.3 3D modeling of the balloon actuator.

## A.5 Experimental, Analytical and Simulation Results

Figure A.4 shows the balloon actuator before and after actuation.



**Figure A.4** The balloon actuator (a) before, and (b) after actuation.

According to Figure A.5, the results of the theoretical and experimental method are in a good fit. The results of the simulation and the experiments show a better agreement compared to the theoretical method. This is because of some simplified assumptions that are made in the theoretical analysis such as the local inflation (inflated arc) which is positioned right above the cavity or modeling of the inflated arc after injecting the air pressure inside the channel (Figure A.5). Also, as Figure A.5 shows, a non-linear trend after 140 *kPa* air pressure could be observed; however, the theoretical method considers PDMS as an incompressible material which have a linear stress-strain behavior at low stress. The more applied air pressure results in more deflection of the PDMS balloon actuator.

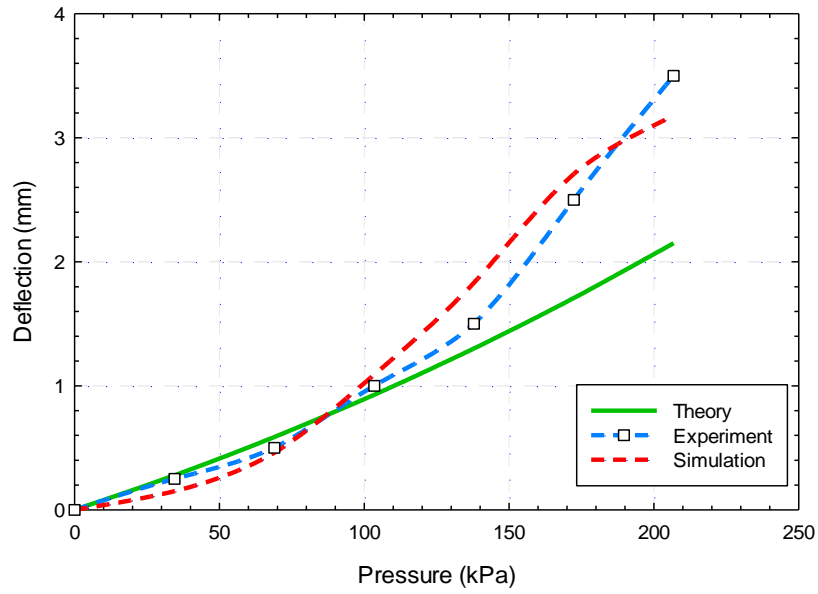


Figure A.5 Experimental, analytical and simulation results for the balloon actuator.

## Appendix B (PDMS Preparation Procedure)

In order to prepare PDMS, seven main steps should be followed:

- I. The preparation of the mold
- II. The scaling and mixing of the PDMS and the curing agent
- III. The degassing to remove bubbles (first time)
- IV. The PDMS pouring on the mold and the degassing to remove bubbles (second time)
- V. The PDMS baking
- VI. The PDMS peeling off the mold
- VII. The PDMS bonding (if applicable)

These steps are explained in detail as follow [115]:

### I. Preparation of the mold

A mold was 3D printed with Miicraft<sup>®</sup> 50. These configurations were used: layer thickness:  $25\ \mu\text{m}$ , curing time:  $6\ \text{s}$ , gap adjustment:  $0.1\ \text{mm}$ , and base curing:  $50\ \text{s}$ . Sometimes,  $50\ \mu\text{m}$  layer thickness was used depends on the structure of the mold. In this case, the curing time of  $7\ \text{s}$  was used. After 3D printing the sample, the mold soaked in 2-Propanol (anhydrous 99.5%). It soaked off after  $20\ \text{min}$  and rinsed with hot water and dried with clean compressed air to remove all dust and particles. The mold was exposed to UV-light for three times (each time for  $10\ \text{min}$ ). For Stratasys<sup>®</sup> (object-24) 3D printer, no specific configurations were used but sodium hydroxide solution (2%) was used as the surface preparation solution. In this case, the mold was immersed into a 2% sodium hydroxide solution for approximately 1-2 hours. After that, the mold was rinsed under running tap water. The other procedures (drying and UV) are as same as Miicraft<sup>®</sup> 50 3D printer.

## **II. The scaling and mixing of the PDMS and the curing agent**

The PDMS is a type of elastomer. To make it harder, more curing agent can be added. The most used PDMS is the Sylgard™ 184 Silicone elastomer and was used in this study. The typical weight ratio between the base and the curing agent is 15:1. This ratio can be changed to prepare a softer or harder PDMS for specific applications. In this study, different ratios of PDMS were used and compared with each other. To prepare the PDMS, the base should be weighed ( $m_b$ ), the curing agent should be added ( $m_{ca}$ ), and should be mixed strongly. It should be noted that first the PDMS and then the curing agent should be poured into a paper cup. Doing the opposite may lead to a bad cross linkage of the polymer. To mix the both components, an automatic PDMS mixer was used (2 *min* mixing with 2000 *rpm*).

## **III. The PDMS degassing to remove bubbles (1<sup>st</sup> time)**

The mixture of components is filled with lots of bubbles due to the mixing procedure and these bubbles have to be removed. If the degassing procedure does not perform well, bubbles will be trapped inside the PDMS sample. There are different ways to degas the PDMS mixture: 1) using a centrifuge, or 2) using a vacuum pump. For the first time, the first option was used (2:30 *min* and 2200 *rpm*). After pouring the mixture into the mold, the second option was used (30 *min*).

## **IV. The PDMS pouring on the mold and the degassing to remove bubbles (2<sup>nd</sup> time)**

Once the mold is clean and the PDMS is degassed, the PDMS could be poured into the mold. Some bubbles would appear during the pouring process and it could be removed with a needle or putting back the mold and PDMS into a vacuum pump.

## V. The PDMS baking

After mixing the base and the curing agent, the cross-linkage has begun but alone it will take around 24 hours to get a solid enough device. Therefore, to expedite this process, the mold and the PDMS have to be baked. The time and temperature of the baking depend on the PDMS ration, the laboratory oven, the user, etc. There are two parameters which can be controlled: 1) Temperature, and 2) time. The PDMS can be baked under a high temperature but a short time or a low temperature but a long time. These two procedures do not have any effect on the chemical properties of the PDMS, but it will influence the mechanical properties. The set temperature should be selected based on the glass temperature of the mold container. We baked the PDMS at 80°C in an oven for 2-4 hours.

## VI. The PDMS peeling off the mold

When the mold and the PDMS reach to the room temperature, then it would be ready to peel off the PDMS. It should be removed easily, otherwise, if the PDMS sticks to the wafer, the mold was not clean enough, or the PDMS did not bake enough.

## VII. The PDMS bonding (if applicable)

The PDMS can bond to another piece of PDMS. Each piece of PDMS must be cleaned thoroughly by isopropanol or an ultrasonic bath. For the oxygen PDMS binding procedure, the surface of each piece of PDMS should be activated, i.e., the  $Si - CH_3$  bonds should transform to  $Si - OH$  bonds and permanent  $Si - O - Si$  bonds will appear. For a good oxygen plasma binding, the recommended pressure inside the chamber is 500 *mTorr*, and 2 *min* is a good time to create strong bonds with the PDMS.

## Appendix C (Electronic System and Components)

### C.1 Electronic System

The electronic control platform could be used to operate and control the soft actuator. The control system is designed to be reconfigurable. The presented electronic system consists of the following components:

- I. Air pump: it provides pressurized air to the actuator.
- II. Valve: it can direct the flow of air in the system.
  - A. Solenoid valve: this is either open or closed, on or off. It operates on different voltages. It is normally open or normally closed but always either on or off.
  - B. Proportional valve: a proportional solenoid valve opens gradually (in steps), depending on the voltage/current applied to the solenoid.
- III. Pressure sensor: it can provide feedback for controlling the system.
- IV. A microcontroller: it is an interface with the hardware via a USB cable (serial port) connection. Various components of the platform can be controlled by the microcontroller or sensor readings can be read.
- V. Switches and MOSFETs: it can control the opening and closing of the valves.
- VI. Rotary potentiometers: it controls the air pressure in the system. A linear potentiometer with a 1/4" mounting diameter and a 10K resistance was used.
- VII. Power Regulator: we need 24 V, 12 V, and 5 V - these chips can be used to take a single input voltage (e.g. 24 V) and convert to our requirements. Alternative is to use three different power supplies.
- VIII. Manual Pressure Regulator: for controlling the air pressure in large increments, a manual pressure regulator was used.
- IX. Base structure: the base structure of the control board is a sheet of acrylic with a water-jet "pegboard" design.

## C.2 Selection of Components for Manual Basic Control Circuit

This section presents a list of items that were used to prepare the control circuit.

- I. Air Pump: an air compressor is used to inject the air into the system.
- II. Water Filter: a filter dryer (Husky HAD704) was connected to the air tubing after the air compressor. Since during the test, condensed water was entered to the actuator and valve, which may affect the performance of the system, a filter dryer was used.
- III. Pressure Sensor: the working principle of this pressure sensor is simple. The air pressure causes the diaphragm to deflect, and deflection is measured by piezo-resistor. The ASDX Series of the pressure sensor has a proportional analog interface for reading pressure over the specified full-scale pressure span and temperature range. Using an on-board Application Specific Integrated Circuit (ASIC), this sensor is fully calibrated, and temperature compensated (range of 0°C to 85°C) for sensor offset, sensitivity, temperature effects and non-linearity. This sensor should work very well with a single power supply of either 3.3  $V_{Dc}$  or 5.0  $V_{Dc}$ . This sensor is capable of measuring gauge pressure referenced to atmospheric pressure.

**Table C.2 Key features of the pressure sensor<sup>1</sup>.**

Features	Desired Feature	ASDX-AVX-100PG-AA5
Shape, size, port configuration and orientation	No specific limitation	The axial port on top, vented cover on the bottom
Supply voltage	0 – 24 $V_{Dc}$	5 $V_{Dc}$
Output	Analog	Analog
Working pressure	0 – 70 <i>psi</i>	0 – 100 <i>psi</i>
Temperature	[0°C, 40°C]	[-20°C, 105°C]

---

<sup>1</sup> More information at: [http://www.farnell.com/datasheets/1850579.pdf?\\_ga=1.244440389.115337667.1482958853](http://www.farnell.com/datasheets/1850579.pdf?_ga=1.244440389.115337667.1482958853)

#### IV. Control Valve

A. Solenoid valve: in the first series of experiments, three-port solenoid valve (VQ110U-5M) was used.

**Table C.3 Key features of the solenoid valve<sup>2</sup>.**

Features	Desired Feature	SMC VQ110U-5M
Shape, size, and body material	3-Port	3-Port M plug connector
Action	Normally Closed	Normally Closed
Operating voltage of the coil	$0 - 24 V_{Dc}$	$24 V_{Dc}$
Temperature	[0°C, 40°C]	[-10°C, 50°C]
Port size	M5	M5
Type of fluid	Air	Air, Inert gas
Valve operating pressure	$0 - 60 \text{ psi}$	$0 - 87 \text{ psi}$
Power consumption (Current)	$\leq 100 \text{ mA}$	$0.7 \text{ W}$ (29 mA)

---

<sup>2</sup> More information at: <https://www.smc-pneumatics.com/pdfs/vq100.pdf>

B. Proportional valve: after establishing the authenticity of the experimental setup with the solenoid valve, a proportional valve was used. A proportional solenoid valve opens gradually (in steps), depending on the voltage. These valves provide infinite positioning of spools results in infinitely adjustable flow volumes. To achieve the infinite positioning of spools, force-controlled or stroke-controlled solenoids are used.

**Table C.4 Key features of the proportional valve<sup>3</sup>.**

Features	Desired Feature	SMC PVQ13-5M-04-M5-A
Shape, size, and body material	2-Port or 3-Port M plug connector	2-Port M plug connector
Action	Normally Closed	Normally Closed
Operating voltage of the coil	$0 - 24 V_{Dc}$	$24 V_{Dc}$
Temperature	[0°C, 40°C]	[0°C, 50°C]
Port size	M5	M5
Type of fluid	Air	Air, Inert gas
Valve operating pressure	$0 - 60 \text{ psi}$	$0 - 66 \text{ psi}$
Power consumption (Current)	$\leq 100 \text{ mA}$	$2 \text{ W (85 mA)}$
Orifice Size (Diameter)	$\leq 0.5 \text{ mm}$	$0.4 \text{ mm}$

---

<sup>3</sup> More information at: <https://www.smcpneumatics.com/pdfs/PVQ.pdf>

- V. Manifold: a manifold is a wide or a bigger pipe, or channel, into which smaller pipes or channels lead. In the proposed system, one or two channels were used, but as the future work, maybe four channels will be needed.

**Table C.5 Key features of the manifold.**

Features	Desired Feature	SMC-VV3Q12U-0401N
Shape, size, and body material	Compatible with SMC VQ110U-5M	Compatible with SMC VQ110U-5M
Base Model	Large flow type	Type U (large flow type) mounting base
Number of stations	$\geq 4$	4
Port size	NPT 1/8	NPT 1/8
Type of fluid	Air	Air, Inert gas

- VI. Power MOSFETs: 4 Opto-Isolated Power FET Switches (IRF540 type)

It can control high power DC devices such as motors, LEDs, and valves. The load is connected from the positive terminal supply to the switch. When the switch is on, it connects the negative load terminal to the ground. This four-channel MOSFET switch is designed to provide four electronic switches which may be used to control different DC loads.

- VII. Arduino MEGA: The Arduino Mega 2560 is a microcontroller board based on the ATmega2560. It has 54 digital input/output pins (of which 15 can be used as PWM outputs), 16 analog inputs, 4 UARTs (hardware serial ports), a 16 MHz crystal oscillator, a USB connection, a power jack, an ICSP header, and a reset button. It simply connects to a computer with a USB cable.

The schematic wiring diagram of the advanced control board and the voltage to current converter board is presented in Figure C.1.

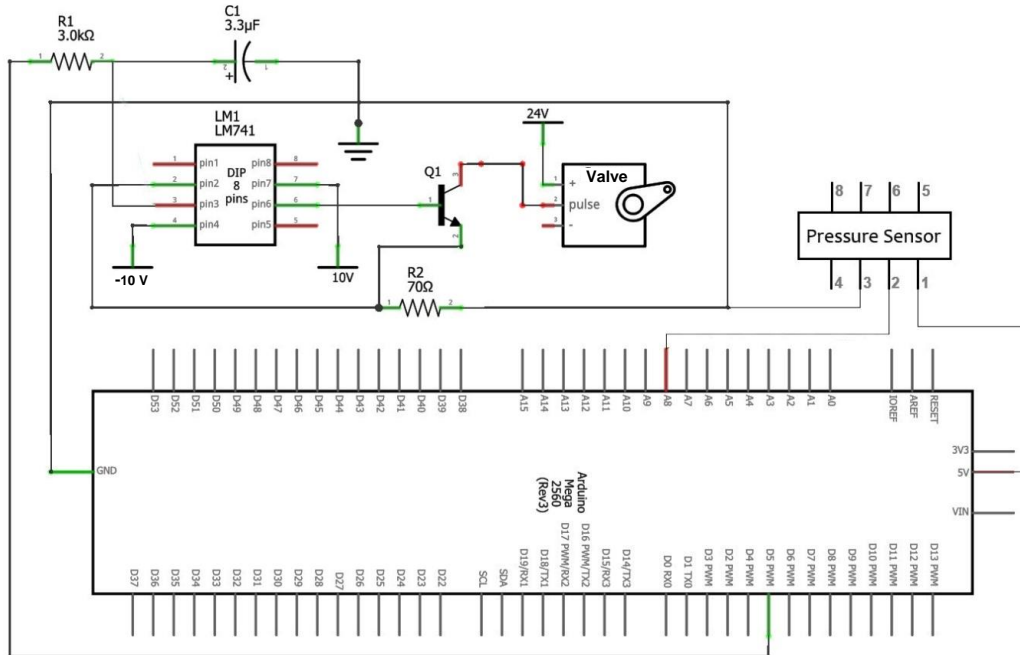


Figure C.1 Schematic wiring diagram of the advanced control board and the voltage to current converter board.

### C.3 Valve characterization

According to the experiments, we found that the proportional valve, which is used in our research, can provide different pressure drop ( $\Delta P$ ) for each driving force (input voltage signal). As shown in Figure C.2, the higher applied voltage leads to a larger pressure drop. Moreover, we observed that for a specific input voltage signal, the higher the operating air pressure, the larger the pressure drop would be achieved.

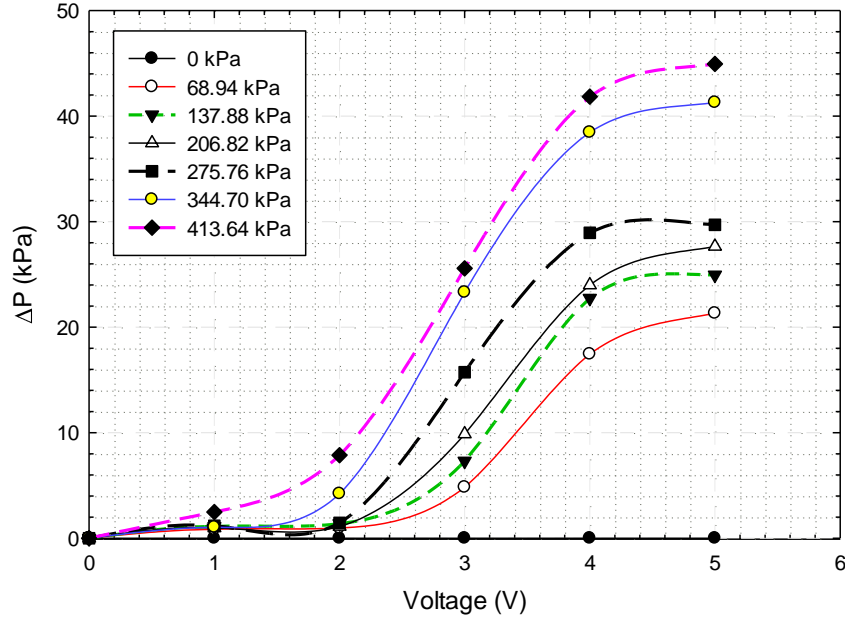


Figure C.2 Proportional valve characterization.

According to Figure C.2, a correlation between the pressure drop ( $\Delta P$ ), the input voltage signal ( $V$ ) and the applied operating pressure ( $P$ ) could be derived by using a curve fitting method. The presented curve fitting has a goodness of fit of  $R^2 = 0.995$ .

$$\begin{aligned}
 \Delta P = & C_{00} + C_{10}P + C_{01}V + C_{20}P^2 + C_{11}PV + C_{02}V^2 + C_{30}P^3 + C_{21}P^2V + \\
 & + C_{12}PV^2 + C_{03}V^3 + C_{40}P^4 + C_{31}P^3V + C_{22}P^2V^2 + C_{13}PV^3 + C_{04}V^4 + \\
 & + C_{50}P^5 + C_{41}P^4V + C_{32}P^3V^2 + C_{23}P^2V^3 + C_{14}PV^4 + C_{05}V^5
 \end{aligned} \tag{C.1}$$

where  $P$  is normalized by *mean* 30 and *standard deviation (std)* 20.24 and  $V$  is normalized by *mean* 2.5 and *standard deviation (std)* 1.729. The coefficients of the presented equation are listed in Table C.6. The idea is that the  $P$  variable is replaced by  $(P - \text{mean}(P))/\text{std}(P)$  and the  $V$  variable is replaced similarly. This is done before any polynomial terms are computed. The transformation will not change the fit theoretically, but it will make the results better conditioned on a computer with finite precision.

**Table C.6 Coefficients of the proportional valve characterization.**

Coefficient	Value	Coefficient	Value	Coefficient	Value
$C_{00}$	0.6663	$C_{21}$	0.5264	$C_{04}$	-0.5632
$C_{10}$	0.4396	$C_{12}$	0.1140	$C_{50}$	-0.1079
$C_{01}$	2.56	$C_{03}$	-0.9217	$C_{41}$	-0.3038
$C_{20}$	0.7807	$C_{40}$	-0.2947	$C_{32}$	0.1270
$C_{11}$	0.932	$C_{31}$	0.2185	$C_{23}$	0.02839
$C_{02}$	1.815	$C_{22}$	-0.1481	$C_{14}$	-0.1193
$C_{30}$	0.4074	$C_{13}$	-0.3164	$C_{05}$	0.1514

The valve is current-controlled, and the correlation between the input Arduino PWM voltage signal and the resultant applied current on the proportional valve should be obtained. The results of the experiments are presented in Figure C.3. A linear relationship between the input PWM voltage and the valve current could be observed.

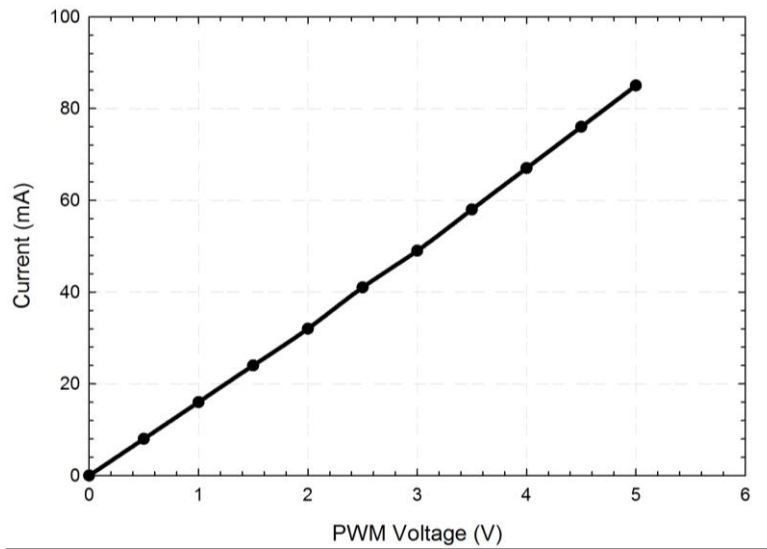


**Figure C.3 Relationship between the input PWM voltage and the valve current.**

## Appendix D (Principles of Operation of LDV)

An LDV is a two beams laser interferometer which measures the frequency or phase difference between a reference beam and a test beam which is directed to the object. The scattered light from the object is collected and interfered with the reference beam on a photodetector (photodiode). Most commercial vibrometers work in a heterodyne regime by adding a known frequency shift ( $30 - 40 \text{ MHz}$ ) to one of the beams which is usually generated by an acousto-optic modulator or a Bragg cell [155].

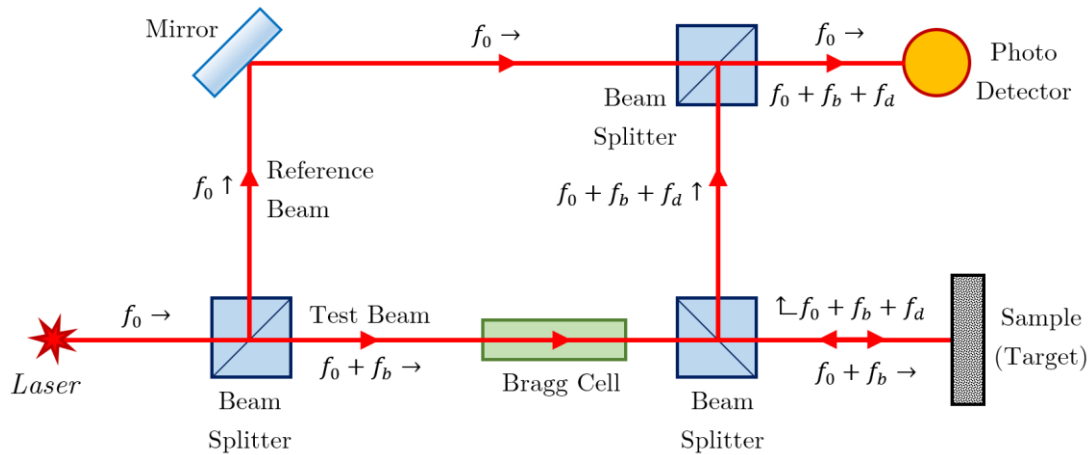


Figure D.1 Basic components of a Laser Doppler Vibrometer [156].

A schematic view of a typical laser vibrometer is shown in Figure D.1. Using a beam splitter, the beam from the laser source ( $f_0$ ) divides into a reference beam ( $f_0$ ) and a measured beam ( $f_t = f_0$ ). The measured beam passes through the Bragg cell, which adds a frequency shift  $f_b$  (carrier frequency). Then, the beam with the shifted frequency of  $f_b + f_0$  directs to the object. The motion of the object adds a Doppler shift (modulation frequency) to the beam  $f_d = 2v(t)\cos(\alpha_{bv})/\lambda$  where  $v(t)$  is the velocity of the object,  $\alpha_{bv}$  is the angle between the laser beam and the velocity vector, and  $\lambda_{wl}$  is the wavelength of the light. Some portion of the light ( $f_0 + f_b + f_d$ ) is collected by the LDV and reflected by the beam splitter to the photodiode. The scattered light ( $f_0 + f_b + f_d$ ) combines with the reference light ( $f_0$ ) at the photodetector. The initial frequency of the laser is

very high ( $> 10^{14}$  Hz), which is higher than the response of the detector. The detector does respond, however, to the beat frequency between the two beams, which is at  $f_b + f_d$ . The output of the photodetector is a standard frequency modulated (FM) signal, with the carrier and modulation frequency. This signal can be demodulated to obtain the velocity of the vibrating object with respect to the time of vibration. The displacement can be obtained based on the velocity data.

## Appendix E (Genetic Algorithm Code)

The sample of the Genetic Algorithm code is as follows:

```
1.  clc;
2.  clear;
3.  close all;
4.
5.  %% Problem Definition
6.
7.  s=tf('s');
8.
9.  G=%here is the transfer function;
10.
11. CostFunction=@(x) MyCost(x,G);    % Cost Function
12.
13. nVar=3;          % Number of Variables
14.
15. VarSize=[1 nVar];    % Size of Variables Matrix
16.
17. VarMin=-1;        % Lower Bound of Variables
18. VarMax= 1;        % Upper Bound of Variables
19.
20. VarRange=[VarMin VarMax]; % Variation Range of Variables
21.
22.
23. %% GA Parameters
24.
25. MaxIt=100;    % Maximum Number of Iterations
26.
27. nPop=50;    % Population Size
28.
29. pCrossover=0.7;    % Crossover Percentage
30. nCrossover=round(pCrossover*nPop/2)*2; % Number of Parents (Offsprings)
31.
32. pMutation=0.2;    % Mutation Percentage
33. nMutation=round(pMutation*nPop); % Number of Mutants
34.
35.
36. %% Initialization
37.
38. % Empty Structure to Hold Individuals Data
39. empty_individual.Position=[];
40. empty_individual.Cost=[];
41. empty_individual.Out=[];
42.
```

```

43. % Create Population Matrix
44. pop= repmat(empty_individual,nPop,1);
45.
46. % Initialize Positions
47. for i=1:nPop
48.     pop(i).Position=unifrnd(VarMin,VarMax,VarSize);
49.     [pop(i).Cost pop(i).Out]=CostFunction(pop(i).Position);
50. end
51.
52. % Sort Population
53. pop=SortPopulation(pop);
54.
55. % Store Best Solution
56. BestSol=pop(1);
57.
58. % Vector to Hold Best Cost Values
59. BestCost=zeros(MaxIt,1);
60.
61. %% GA Main Loop
62.
63. for it=1:MaxIt
64.
65.     % Crossover
66.     popc=repmat(empty_individual,nCrossover/2,2);
67.     for k=1:nCrossover/2
68.
69.         i1=randi([1 nPop]);
70.         i2=randi([1 nPop]);
71.
72.         p1=pop(i1);
73.         p2=pop(i2);
74.
75.         [popc(k,1).Position popc(k,2).Position]=Crossover(p1.Position,p2.Position,VarRange);
76.
77.         [popc(k,1).Cost popc(k,1).Out]=CostFunction(popc(k,1).Position);
78.         [popc(k,2).Cost popc(k,2).Out]=CostFunction(popc(k,2).Position);
79.
80.     end
81.     popc=popc(:);
82.
83.
84.     % Mutation
85.     popm=repmat(empty_individual,nMutation,1);
86.     for k=1:nMutation
87.
88.         i=randi([1 nPop]);
89.
90.         p=pop(i);
91.

```

```

92.     popm(k).Position=Mutate(p.Position,VarRange);
93.
94.     [popm(k).Cost popm(k).Out]=CostFunction(popm(k).Position);
95.
96.     end
97.
98.     % Merge Population
99.     pop=[pop
100.         popc
101.         popm];
102.
103.     % Sort Population
104.     pop=SortPopulation(pop);
105.
106.     % Delete Extra Individuals
107.     pop=pop(1:nPop);
108.
109.     % Update Best Solution
110.     BestSol=pop(1);
111.
112.     % Store Best Cost
113.     BestCost(it)=BestSol.Cost;
114.
115.     % Show Iteration Information
116.     disp(['Iteration ' num2str(it) ': Best Cost = ' num2str(BestCost(it))]);
117.
118.     % Plot Step Response
119.     figure(1);
120.     step(BestSol.Out.T);
121.
122. end
123.
124. %% Plots
125.
126. figure;
127. plot(BestCost);

```

```

1.  function [z out]=MyCost(x,G)
2.
3.     % G: Plant Transfer Function
4.     % K: PID Controller Transfer Function
5.     % T: Closed-Loop Transfer Function [T = G*K/(1+G*K)]
6.
7.     kp=100*x(1);
8.     ki=100*x(2);
9.     kd=10*x(3);
10.     Tf=0.1;

```

```

11.
12.   K=pid(kp,ki,kd,Tf);
13.
14.   T=feedback(K*G,1);
15.
16.   info=stepinfo(T);
17.
18.   MP=info.Overshoot;
19.   Ts=info.SettlingTime;
20.
21.   MaxRealPole=-min(max(real(pole(T))),0);
22.   SI=1/MaxRealPole;
23.
24.   w1=1;
25.   w2=1;
26.   w3=1;
27.
28.   z=w1*MP+w2*Ts+w3*SI;
29.
30.   out.kp=kp;
31.   out.ki=ki;
32.   out.kd=kd;
33.   out.Tf=Tf;
34.   out.G=G;
35.   out.K=K;
36.   out.T=T;
37.   out.ClosedLoopStepInfo=info;
38.   out.ClosedLoopPoles=pole(T);
39.   out.MaxRealPole=MaxRealPole;
40.   out.SI=SI;
41.   out.MP=MP;
42.   out.Ts=Ts;
43.   out.z=z;
44.
45. end

```

```

1. function [pop Costs]=SortPopulation(pop)
2.
3.   Costs=[pop.Cost];
4.
5.   [Costs SortOrder]=sort(Costs);
6.
7.   pop=pop(SortOrder);
8.
9. end

```

```
1. function y=Mutate(x,VarRange)
2.
3.     nVar=numel(x);
4.
5.     j=randi([1 nVar]);
6.
7.     VarMin=min(VarRange);
8.     VarMax=max(VarRange);
9.     sigma=(VarMax-VarMin)/10;
10.
11.    y=x;
12.    y(j)=x(j)+sigma*randn;
13.
14.    y=min(max(y,VarMin),VarMax);
15.
16. end
```

```
1. function [y1 y2]=Crossover(x1,x2,VarRange)
2.
3.     VarMin=min(VarRange);
4.     VarMax=max(VarRange);
5.
6.     delta=0.1;
7.     alpha=unifrnd(-delta,1+delta,size(x1));
8.
9.     y1=alpha.*x1+(1-alpha).*x2;
10.    y2=alpha.*x2+(1-alpha).*x1;
11.
12.    y1=min(max(y1,VarMin),VarMax);
13.    y2=min(max(y2,VarMin),VarMax);
14.
15. end
```

## Appendix F (Dynamic Response Considerations)

The effect of the length of the tube on the pressure drop was investigated. The schematic of the pressure-transmitting system is shown in Figure F.1:

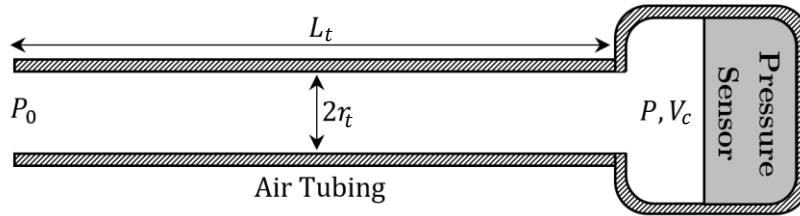


Figure F.1 Schematic of the pressure-transmitting system.

The transient response of pressure-measuring instruments depends on: 1) the response of the transducer element; and 2) the response of the pressure-transmitting fluid, the connecting tubing, etc. Frequently, the second factor determines the overall frequency response of the system. The following analysis could be used to estimate this behavior:

The fluctuating pressure has a frequency of  $\omega$  and  $P_0$  and  $P$  are the amplitude of the pressure signal in the source and applied on the transducer, respectively. The length and radius of the tube are  $L_t$  and  $r_t$ , respectively. A chamber of volume  $V_c$  is considered at the end of the tube where the connection to the pressure-sensitive transducer is made. The fluid friction could be estimated by the conventional formula for laminar friction resistance in the tube and results in the mass vibration of the injected fluid. This friction tends to dampen the motion. The pressure-amplitude ratio can be obtained as follows [157]:

$$\left| \frac{P}{P_0} \right| = \frac{1}{\sqrt{\left[ 1 - \left( \frac{\omega}{\omega_n} \right)^2 \right]^2 + 4h^2 \left( \frac{\omega}{\omega_n} \right)^2}} \quad (\text{F.1})$$

Considering  $V_s$  as the velocity of sound in the fluid,  $\mu_d$  as the dynamic viscosity of the fluid, and  $\rho$  as the fluid density, the natural frequency  $\omega_n$ , the damping ratio  $h_d$ , and the phase angle  $\phi$  for the pressure signal can be derived as follows [157]:

$$\omega_n = \sqrt{\frac{3\pi r_t^2 V_s^2}{4L_t V_c}} \quad (\text{F.2})$$

$$h_d = \frac{2\mu_d}{\rho V_s r_t^3} \sqrt{\frac{3L_t V_c}{\pi}} \quad (\text{F.3})$$

$$\phi = \tan^{-1} \left( \frac{-2h_d \left( \frac{\omega}{\omega_n} \right)}{1 - \left( \frac{\omega}{\omega_n} \right)^2} \right) \quad (\text{F.4})$$

$$V_s = 20.04 \sqrt{T} \text{ m.s}^{-1} \text{ with } T \text{ (Temperature) in } K \quad (\text{F.5})$$

If the transmitting fluid is a gas, the entire system can act as a *Helmholtz* resonator with a resonant frequency of [157]:

$$\omega_n = \sqrt{\frac{\pi r_t^2 V_s^2}{V_c (L_t + 0.5\pi r_t)}} \quad (\text{F.6})$$

According to the performed experiments,  $r_t = 0.794 \times 10^{-3} \text{ m}$ ,  $V_s = 344.092 \frac{\text{m}}{\text{s}}$ ,  $\rho = 1.204 \frac{\text{kg}}{\text{m}^3}$ ,  $\mu_d = 1.825 \times 10^{-5} \frac{\text{kg}}{\text{m.s}}$ , and  $V_c = 3.116 \times 10^{-9} \text{ m}^3$ . Therefore, the damping ratio, natural frequency, and  $\left| \frac{P}{P_0} \right|$  would be:

$$h_d = 9.609 \times 10^{-3} \sqrt{L_t} \quad (\text{F.7})$$

$$\omega_n = \frac{7510.341}{\sqrt{L_t}} \quad (\text{F.8})$$

$$\left| \frac{P}{P_0} \right| = \frac{1}{\sqrt{[1 - 1.773 \times 10^{-8} \omega^2 L_t]^2 + 6.548 \times 10^{-12} \omega^2 L_t^2}} \quad (\text{F.9})$$

For the Z-axis actuator, low frequencies would be enough as  $f = 3 \text{ Hz}$  or  $\omega = 18.85 \text{ Hz}$ . Therefore,

$$\left| \frac{P}{P_0} \right| = \frac{1}{\sqrt{1 - 1.259 \times 10^{-5} L_t + 2.367 \times 10^{-9} L_t^2}} \quad (\text{F.10})$$

In the proposed system, Figure F.2 shows that increasing the length of the tube does not have a considerable effect on the input pressure ( $P_0$ ) and the pressure that is measured in the position of the sensor ( $P$ ). Even for a 100  $m$  length tube, according to Figure F.2,  $1000 \left(1 - \frac{P}{P_0}\right) = 0.62$ ; therefore,  $P = 0.9994P_0$  or  $P \cong P_0$ .

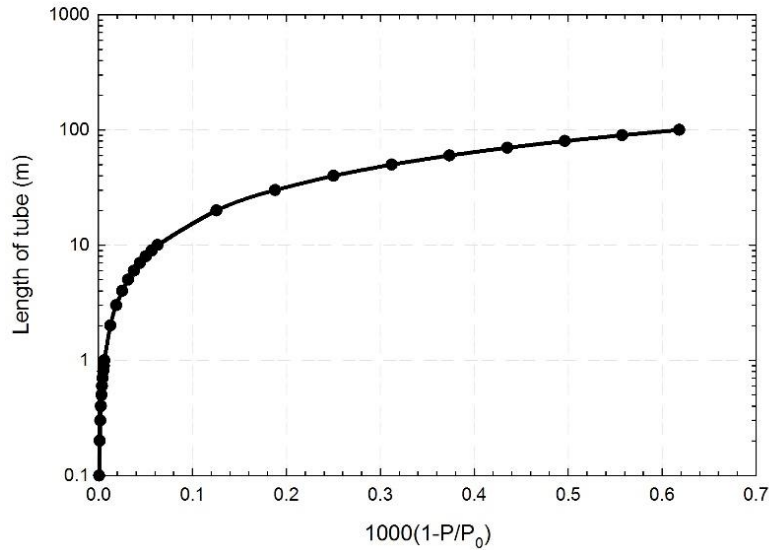


**Figure F.2** The effect of length of the tube on the pressure drop.

In order to experimentally show that the effect of the length of the tube on the measured pressure by the sensor is negligible, an impulse response was applied to the system. Two cases were investigated: a very long tube (3  $m$ ) and a short tube (30  $cm$ ). As the experimental analysis shows (Figure F.3), in both cases, the pressure has the same behavior regardless of the length of the tube.

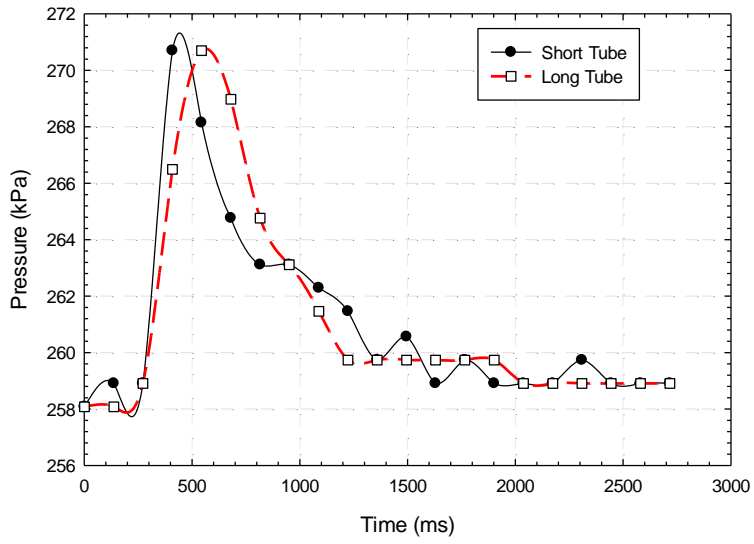


Figure F.3 The effect of the length of the tube by applying an impulse response.

In the performed experiments, a tube with a length of  $L_t = 30\text{ cm}$  was used. Figure F.4 shows the response of the PDMS actuator under the step function with the setpoint of  $125\text{ kPa}$ . According to Figure F.4, the system has a low damping coefficient of 0.005.

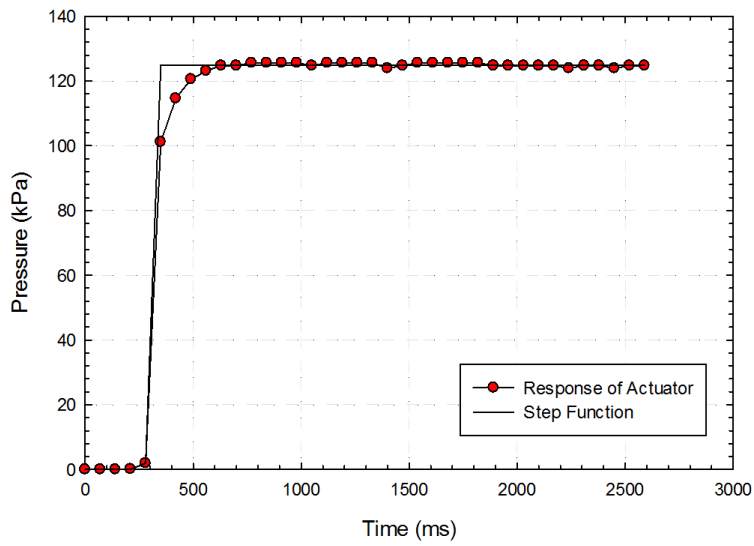


Figure F.4 Response of the PDMS actuator due to the step function.